

AD-A237 577



(2)

DEPARTMENT OF OCEANOGRAPHY  
COLLEGE OF SCIENCES  
OLD DOMINION UNIVERSITY  
NORFOLK, VIRGINIA 23529

DTIC  
ELECTE  
JUL 01 1991  
S D D

Technical Report No. 91-7

MESOSCALE CHARACTERISTICS AND THE ROLE  
OF DEFORMATION ON OCEAN DYNAMICS

By

Albert D. Kirwan Jr., Principal Investigator

Final Report  
For the period 15 December 1988 to 30 September  
1990

Prepared for  
Office of Naval Research  
800 N Quincy Street  
Arlington, Virginia 22217-5000

**DISTRIBUTION STATEMENT A**

Approved for public release  
Distribution Unlimited

Under  
ONR Contract N00014-89-J-1595  
Dr. Thomas Kinder, Scientific Officer

Submitted by the  
Old Dominion University Research Foundation  
P.O. Box 6369  
Norfolk, Virginia 23508-0369

!

1991

91 6 17 056

91-02364



# OCEANOGRAPHY



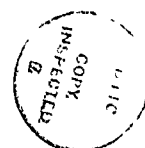
OLD DOMINION UNIVERSITY

Department of Oceanography  
Old Dominion University  
Norfolk, Virginia 23529-0276  
(804) 683-4285  
Fax (804) 683-5303

Chief of Naval Research  
c/o Dr. David Evans  
Office of Naval Research  
Code 1122PO  
800 North Quincy Street  
Arlington, VA 22217-5000

Accession For	
NHS CRASH	<input checked="" type="checkbox"/>
DATA	<input type="checkbox"/>
Unpublished	<input type="checkbox"/>
Justification	
By	
Date	
Availability Codes	
Dist	Availability of
A-1	

June 5, 1991



Dear Sir/Madam:

This letter constitutes the final report for ONR contract N00014-89-J-1595 awarded to Old Dominion University for the period December 15, 1988 through September 30, 1990.

The bulk of the activities conducted under this contract consisted of basic research on ocean flow dynamics as it pertains to the prediction of ocean motions. Results from the research conducted during this period were published in refereed scientific literature. They included:

1. "Evolution of a Warm-Core Ring in the Gulf of Mexico: Lagrangian Observations," *J. Geophys. Res.*, 94(C6), 8163-8178, 1989.
2. "Fractal Drifter Trajectories in the Kuroshio Extension," *Tellus*, 41(A), 416-435, 1989.
3. "Ring Evolution in General Circulation Models from Path Analysis," *J. Geophys. Res.*, 95(C10), 18057-18073, 1990.
4. "Dynamics of Warm-Core Mesoscale Eddies," *Chin. J. Oceanol. Limnol.*, 8(3), 220-231, 1990.

Also presented and published at an international conference was:

"A Synopsis of Mesoscale Eddies in the Gulf of Mexico." Symposium Proceedings of the 1988 Liege Colloquium on Ocean Hydrodynamics, Mesoscale/Synoptic Coherent Structures in Geophysical Turbulence (J. C. J. Nihoul and B. M. Jamart, Editors).

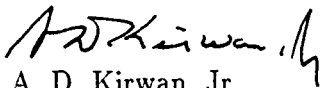
There were several other contract-related activities. A paper entitled, "Super-Inertial Fluctuations of Meso-Scale Eddies" was presented at the American Geophysical Union meeting in San Francisco, 1990. The Principal Investigator served as chairman of the 6.1. external review team for the Naval Research Laboratory in the spring of 1990.

The Principal Investigator also served as a member of the Chief, Naval Oceanographic Command's (CNOC) panel for transision ocean predictive models into operational use.

The contract provided support for William Indest, a Ph.D. Graduate student in oceanography.

I am very grateful for the support provided to the Office of Naval Research for continued support for this research.

Respectfully,

A handwritten signature in dark ink, appearing to read "A. D. Kirwan, Jr." with a stylized flourish at the end.

A. D. Kirwan, Jr.  
Samuel L. and Fay M. Slover  
Chair of Oceanography

## Evolution of a Warm-Core Ring in the Gulf of Mexico: Lagrangian Observations

JAMES K. LEWIS

*Science Applications International Corporation, College Station, Texas*

A. D. KIRWAN, JR.

*Department of Oceanography, Old Dominion University, Norfolk, Virginia*

GEORGE Z. FORRISTALL

*Shed Development Company, Houston, Texas*

During 1985 and 1986, a Gulf of Mexico ring shed by the Loop Current was observed to migrate toward the western Gulf of Mexico. This movement across the gulf was well documented by observations that included drifter data within and outside the ring, sea surface temperature at weekly intervals, expendable bathythermograph surveys at various times, one major hydrographic cruise when the ring was in the northwestern gulf, and currents from moorings over which the ring passed. The drifter data were used to infer the movement of the ring center as well as the eccentricity and orientation of the major axes. The data from the drifters bridge the gaps between detailed surveys to the extent that a daily history of the position and shape of the ring can be constructed. The synthesis of these diverse but complimentary data sources provides a detailed description of how the ring interacted with the bathymetry of the northern Gulf of Mexico as well as with previously and subsequently shed rings.

### 1. INTRODUCTION

A number of studies in the last several years have indicated that Loop Current rings have a major influence in the central and western Gulf of Mexico (GOM). Not only are these anticyclonic features important with respect to the salt and heat budgets of the western GOM [Elliot, 1979], but they also appear to be the dominant factor in momentum balance [Elliot, 1982; Kirwan *et al.*, 1984a]. This last factor is due to the large size of Loop Current rings (radius of  $\sim 150$  km), the intensity of circulation (velocities about the center, or swirl velocities, of 50–75 cm/s), and the frequency of ring separation from the Loop Current (up to three in 1 year [Elliot, 1982]). Lewis and Kirwan [1985, 1987] showed that a number of these anticyclones can exist in the GOM at a given time, resulting in a considerable amount of interaction between the flow fields of individual rings.

Beyond the confines of the American mediterranean, Loop Current rings may also play an important role in the overall energy budget of the North Atlantic gyre. The general picture of this large anticyclonic flow pattern is acceleration and entrainment on approaching the western boundary and energy transfer to other scales at the northern end of the gyre. One of the primary mechanisms for decelerating the Gulf Stream and dissipating energy in the North Atlantic Current is thought to be through the generation of eddies. However, Elliot [1979] suggested that the size, intensity, and frequency of Loop Current rings might represent a significant loss of energy for the western boundary system. It is conceivable then that the energy associated

with Loop Current rings is an important factor in the western boundary energy balance of the North Atlantic.

The motion and processes that are typical during the life history of a Loop Current ring are only now being identified through drifter studies, numerical simulations, and satellite imagery work. After having been pinched off from the Loop Current, these anticyclones move westward across the GOM at a rate of 3 to 8 cm/s [Cochrane, 1972; Elliot, 1982; Kirwan *et al.*, 1984a]. The primary path of the rings is westward through the deepest portion of the GOM [Lewis and Kirwan, 1985]. However, a more northerly route has been identified by Vitkovich and Crisman [1986]. Analysis of drifter data and numerical model studies indicate that the anticyclones remain relatively stable during their westward migration [Kirwan *et al.*, 1984a; Hurlburt and Thompson, 1980] until they reach  $\sim 93^\circ\text{W}$  (approximately 400 km from the western GOM coastline). The orthodox view is that at this longitude the rings begin interacting with the continental slope, where they are often observed to migrate northward. There are at least two explanations for this migration. Nakamoto [1986] has shown that it can be explained as a propagating solitary wave. Smith [1986] has postulated that the northward migration is the result of the nonlinear acceleration of the northward flow between the coast and the ring center. There is also some evidence that rings at this longitude may be strongly affected by circulation structures along the slope. Merrell and Morrison [1981] and Merrell and Vazquez [1983] showed that there can be an eastward transport of 30 Sv off the slope. Lewis and Kirwan [1985] showed an example where a ring impacted the western slope before an earlier ring had dissipated. Recent modeling studies [Thompson, 1986] tend to indicate that the rings go through their final stages of decay in the northwestern corner of the GOM, but

Copyright 1989 by the American Geophysical Union

Paper number 89JC00464.  
0148-0227/89/89JC-0464\$05.00

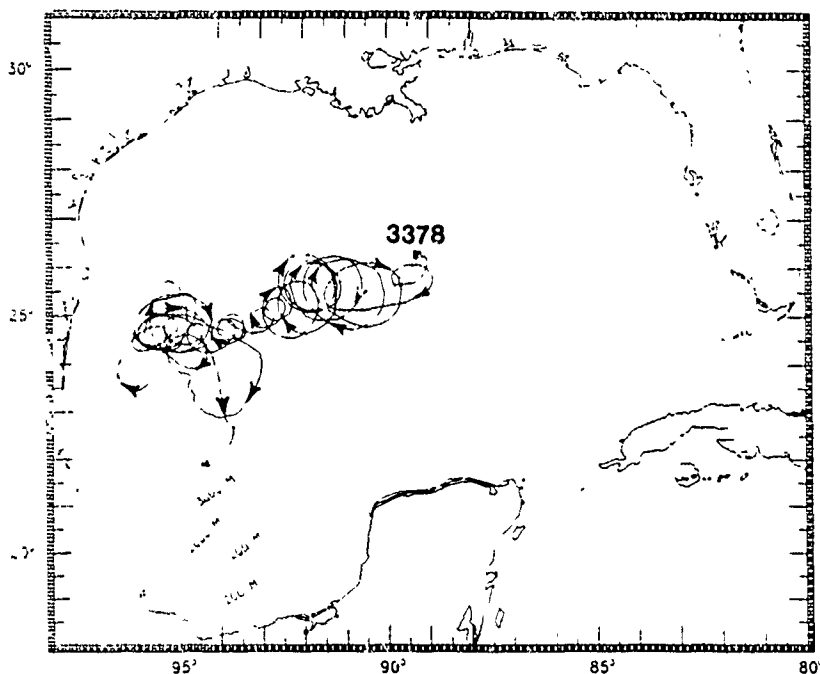


Fig. 1. Trajectory for drifter 3378. Depth contours are in meters. Squares denote the beginning positions of the drifter trajectories, and triangles denote the end positions.

they may be often reenergized by coalescing with younger anticyclones moving northward along the Mexican coastline.

These studies raise several fundamental questions about the dynamics of the Gulf of Mexico. For example, how many rings are there likely to be at any one time in the GOM? What are the dynamical mechanisms that determine the paths of the rings across the GOM? To what extent do the rings interact with each other and with the topography? What is the fate of these rings in the western GOM?

Throughout the spring of 1985, sea surface temperature (SST) and ship of opportunity expendable bathythermograph (XBT) data indicated that a major eddy was on the verge of separating from the Loop Current. As it seemed ideal for addressing some of the above questions, an extensive effort was made to study this ring as it moved into the western Gulf of Mexico. A number of data sets were collected. First, XBT data were collected by ships of opportunity while the ring was in the east central GOM. In addition, the ring was seeded with a drifter which stayed in the ring from July 18, 1985, to approximately May 20, 1986. Several other drifters gave information on the ring during the year. SST data from satellite imagery were analyzed on a weekly basis from July 1985 through August 1986. Other water column surveys were conducted, including an XBT survey during November 11–13, 1985; a hydrographic survey from January 23 to February 6, 1986; a second XBT survey from April 30 to May 6, 1986; and a final XBT survey in the western GOM during August 16–22, 1986. Finally, three sets of current meters were moored in the northwestern GOM during the life of the ring.

The basis of this paper is a presentation and discussion of the Lagrangian data sets along with an analysis and interpretation of the data. The next section describes in more detail the data used in this study. Section 3 provides a chronology of events for the movement of the 1985 ring across the GOM.

Finally, in section 4 some dynamical interpretations of events in the ring's lifetime are discussed.

We concentrate on factors pertaining to the ring's motion along the northern continental slope of the Gulf of Mexico. In addition, we describe and interpret the interaction of the ring with an older ring as well as with a younger ring. We suggest that the more northerly route across the GOM is induced by the proximity of a previously shed ring. We also show that the ring entrains a considerable amount of shelf water. This ring's interactions with a previous ring and a succeeding ring appear to be different. With the older, smaller ring, mass is stripped off and swirled into the center of rotation of this ring. However, when the ring is confronted by a younger ring of similar size, the two apparently coalesce.

## 2. THE DATA

The primary Lagrangian data detailed in this study are the position data of the drifter with Argos identification number 3378 (Figure 1). Since several other drifters gave information on the ring, we have departed from our previous practice of numbering the ring after the buoy, and simply called it Fast Eddy. Fast Eddy was tracked across the GOM for a 10-month period, during which time drifters 5678 and 5683 were also entrained in the ring's flow field. As it approached the Mexican coast, Fast Eddy interacted with a previously shed ring called Ghost Eddy [Lewis and Kirwan, 1987]. Several drifters were associated with Ghost Eddy. Their identification numbers were 3353, 5495, and 5682. Actually, drifter 5495 had been seeded in Fast Eddy, but it was cast out early and became entrained in Ghost Eddy. A seventh drifter, number 3354, was entrained in the Loop Current at the time Fast Eddy was being shed [Lewis and Kirwan, 1987]. An eighth drifter, number 3379, was seeded in a subsequent ring (Hot Eddy) in March of 1986. Fast Eddy and the younger

TABLE 1. Drifters, Their Associated Oceanographic Structures, and Periods During Which Position Data Were Collected

Drifter Identification	Associated Anticyclone	Time in Gulf of Mexico
3378	Fast Eddy	July 18, 1985 to June 26, 1986
5495	Fast Eddy, Ghost Eddy	June 29, 1985, to Jan. 23, 1986
5680	not in a ring	July 18, 1985, to Sept. 5, 1985
5682	Ghost Eddy	Aug. 6, 1985 to Oct. 11, 1985
3354	Loop Current Anticyclone	June 18, 1985, to Sept. 15, 1985
5683	Fast Eddy	Aug. 3, 1985 to Nov. 24, 1985
5678	Fast Eddy, Hot Eddy	Oct. 23, 1985, to April 30, 1986
3353	Ghost Eddy, Fast Eddy	Nov. 3, 1985, to May 22, 1986
3379	Hot Eddy	March 7, 1986, to Jan. 22, 1987

Hot Eddy interacted as the latter drifted into the western GOM. Table 1 summarizes the drifter data sources.

In some cases, the Lagrangian data are presented along with corresponding sea surface temperature data for the entire GOM. The SST maps represent average temperature structure over a 7-day period. Additional flow characteristics can be inferred from these SST contours.

The path information from the drifters was analyzed to provide various kinematic data [Kirwan *et al.*, 1988] which detail the changes of Fast Eddy during its lifetime. These include changes in swirl speed (rotary speed about the translating center of the ring), vorticity, period of rotation, ellipticity (eccentricity and orientation of the axes), deformation (shape change rate), and size.

Water column parameters are used to infer changes in the size and extent of Fast Eddy. Specifically, we look at the volume of water between the 8°C and 15°C isotherms across the ring where the 8°C isotherm reaches upward to the depth of 550 m. This was done by using the water temperature data (accuracy of  $\pm 0.1^\circ\text{C}$ ) to estimate the eccentricity of the ring and then calculating a volume based on that eccentricity. Moreover, the spatial pattern of the depths of the 8°C isotherms helps describe the character of flow around the ring. The 8°C isotherm was chosen because this temperature surface is not affected by surface heating and cooling. Similarly, the 15°C isothermal surface is rarely affected by surface processes except in shallow shelf regions ( $<100$  m). As for the consideration of lateral extents bounded by where the 8°C isothermal surface reaches 550 m, an inspection of XBT data showed that the 8°C surface typically has its greatest slope in rings at 550 m. Thus the 550-m extent of the 8°C surface is a good indicator of the eddy edge. The hydrographic data collected for Fast Eddy are listed in Table 2.

### 3. THE MOVEMENT OF FAST EDDY

Drifter 3378 was seeded in Fast Eddy at  $26.4^\circ\text{N}$ ,  $89.3^\circ\text{W}$  on July 18, 1985. As is shown in Figure 1, Fast Eddy slowly moved westward, reaching approximately the  $91^\circ\text{W}$  meridian by mid-August. Then instead of continuing on the usual path, Fast Eddy held against the slope of the continental

TABLE 2. Cruises During Which XBT Water Temperature Data Were Collected for Fast Eddy

Source	Date
M/V NATCO 6	July 16–19, 1985
R/V Pelican	Oct. 22–27, 1985
AXBT survey	Nov. 11–13, 1985
B O Altan	Jan. 23 to Feb. 5, 1986
B O Altan	April 26 to May 14, 1986
HO-2	Aug. 16–22, 1986

shelf and even moved slightly north of west until it reached  $92^\circ\text{W}$ . The ring became essentially stationary for three revolutions. Then in mid-September 1985, Fast Eddy abruptly moved southward into deeper water. This movement occurred within one revolution of the ring ( $\sim 11$  days). The ring then translated westward, with the drifter moving closer to the ring center (note the smaller loops between  $92^\circ\text{W}$  and  $95^\circ\text{W}$  in Figure 1). The latter part of the trajectory data (mid-November 1985 through May 1986) shows Fast Eddy interacting with the western shelf of the GOM. Several processes occurred during this time, and these will be covered in more detail later in the paper.

#### Separation of Fast Eddy and Initial Movement

The initial characteristics of Fast Eddy have been discussed by Lewis and Kirwan [1987]. Drifter 3378 exhibited current speeds of 60 to 90 cm/s at radii of 60 to 100 km. The Gulf of Mexico flow field for the week beginning August 7, 1985, is depicted in Figure 2. This shows drifter 3378 at a relatively large radius in Fast Eddy along with Ghost Eddy just to the southwest. Drifters 3354 and 5683 were associated with the flow field of the Loop Current, with 3354 defining an anticyclone within the Loop Current [Lewis and Kirwan, 1987]. Drifter 5680 was seen to have some anticyclonic motion to the northeast of Fast Eddy, but temperature profile data indicate that the flow was not directly related to that of Fast Eddy [see Lewis and Kirwan, 1987, Figure 9].

Fast Eddy became stalled along the northern continental slope until mid-September 1985. During this time, the drifter exhibited slightly weaker currents (50–70 cm/s) at radii from 50 to 80 km from the ring center. The ring then made its rather rapid southern movement, and the resulting condi-

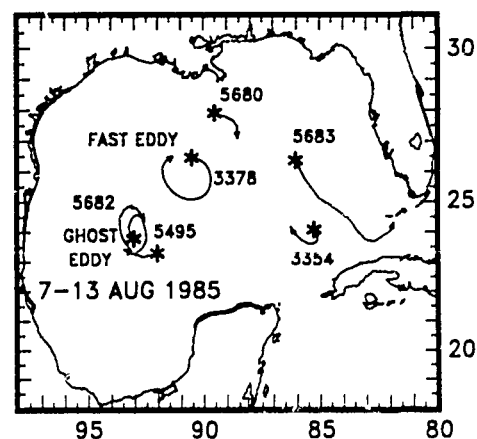


Fig. 2. Drifter trajectories for August 7–13, 1985. Asterisks represent the initial positions of the drifters.

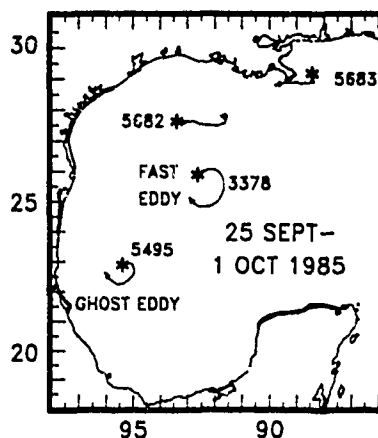


Fig. 3 Drifter trajectories for September 25 through October 1, 1985. Asterisks represent the initial positions of the drifters.

tions are shown in Figure 3. There are two interesting facts to be pointed out in Figure 3. The first is that Ghost Eddy was well southwest of Fast Eddy at that time (September 25 to October 1, 1985). Ghost Eddy had continued its south-westward migration, the preferred path of most GOM rings [Vukovich and Crissman, 1986, Lewis and Kirwan, 1985]. The second interesting factor is the location of drifter 5683. This drifter had been near the Florida Straits (Figure 2), but moved northward and then westward to a position off the Mississippi delta. As will be seen, this drifter eventually became entrained in the flow field of Fast Eddy.

As October 1985 progressed, drifter 3378 moved to tighter orbits ( $\sim 40$ -km radii) in Fast Eddy. Conditions for October 23–29 are shown in Figure 4. Fast Eddy had moved west-southwest into deeper water, and Ghost Eddy had reached the Mexican coast at  $\sim 22.5^\circ\text{N}$ . Drifter 5678 is seen to have some anticyclonic motion to the north of Fast Eddy, and drifter 5683 appears to be following drifter 5678.

#### Interactions in the Western Gulf

After October 1985, Fast Eddy began its interaction with the northwestern corner of the GOM continental slope.

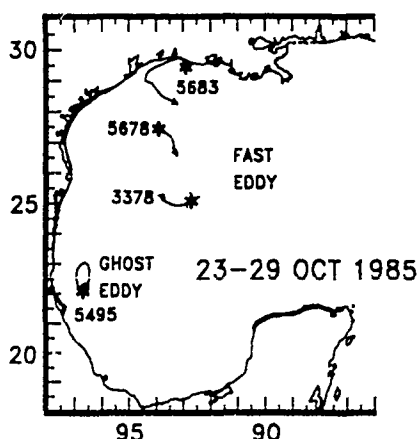


Fig. 4. Drifter trajectories for October 23–29, 1985. Dotted lines indicate the locations of ring waters (based on XBT data) and the edges of Fast Eddy. Asterisks represent the initial positions of the drifters.

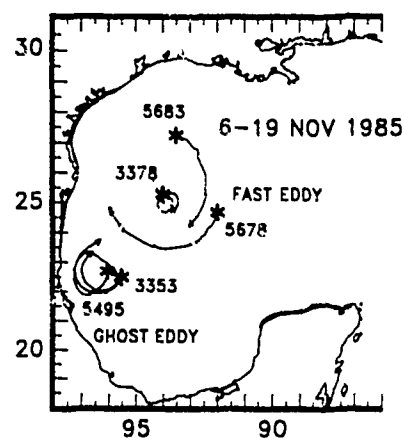


Fig. 5 Drifter trajectories for November 6–19, 1985. Dotted lines indicate the locations of ring waters (based on XBT data) and the edges of Fast Eddy. Asterisks represent the initial positions of the drifters.

Conditions for November 6–19, 1985, are shown in Figure 5. Two drifters were in Ghost Eddy while three drifters were in Fast Eddy. The southern edge of the flow field of Fast Eddy is located at  $23^\circ\text{N}$ , the same latitude of the apparent northern edge of Ghost Eddy. The northern edge of the influence of Fast Eddy is seen to be at  $\sim 27^\circ\text{N}$ . These drift data coincide well with the outline of the ring as determined by depth of the  $8^\circ\text{C}$  isothermal surface from an air-dropped XBT (AXBT) survey of November 11–13, 1985 (Figure 6). These temperature data indicate that the ring was being deformed along its northwestern edge.

An interesting sequence of events followed the mid-November time period. Over the next 2.5 months, Fast Eddy and Ghost Eddy interacted in such a manner that the two rings coalesced. The conditions of November 6–19, 1985 (Figure 5), show Fast Eddy to be quite large. The motion of the drifters imply a radius of at least 200 km. Ghost Eddy is about half as large. In the November 20–26, 1985, SST map (Figure 7), Fast Eddy is still seen to be quite circular, with the movement of drifter 5678 being northward along a tongue of  $26^\circ\text{C}$  water. Also note that one of the drifters in Ghost Eddy had left that ring, moving northeastward along the same curvature as the southwestern section of Fast Eddy. Over the next 3 weeks, this drifter (3353) made a slow cyclonic loop near the Mexican coast at  $\sim 24^\circ\text{N}$ . During the same period, drifter 5678 continued moving north-northeast along the western edge of Fast Eddy and reached  $28^\circ\text{N}$ . Finally, note the characteristic bulge of the Loop Current ( $26^\circ\text{C}$  isotherm) in Figure 7 as it pushes northward into the GOM. This is the beginning of a new ring (to be called Hot Eddy) which will be shed from the Loop Current in January 1986.

By mid-December 1985, both drifters that had been in Ghost Eddy were moving northward along the west side of Fast Eddy along a tongue of  $24^\circ\text{C}$  temperature water. By December 22–28, 1985 (Figure 8), the field of flow became even better organized. A large tongue of  $24^\circ\text{C}$  water extended from the location of Ghost Eddy ( $22.5^\circ\text{N}$ ) to  $27.5^\circ\text{N}$ . The four drifters moved along or within this water mass in an anticyclonic manner.

By mid-January 1986 this large, highly elliptical anticyclone apparently began a process of consolidation. The center of rotation for drifters 3378, 3353, and 5495 moved to

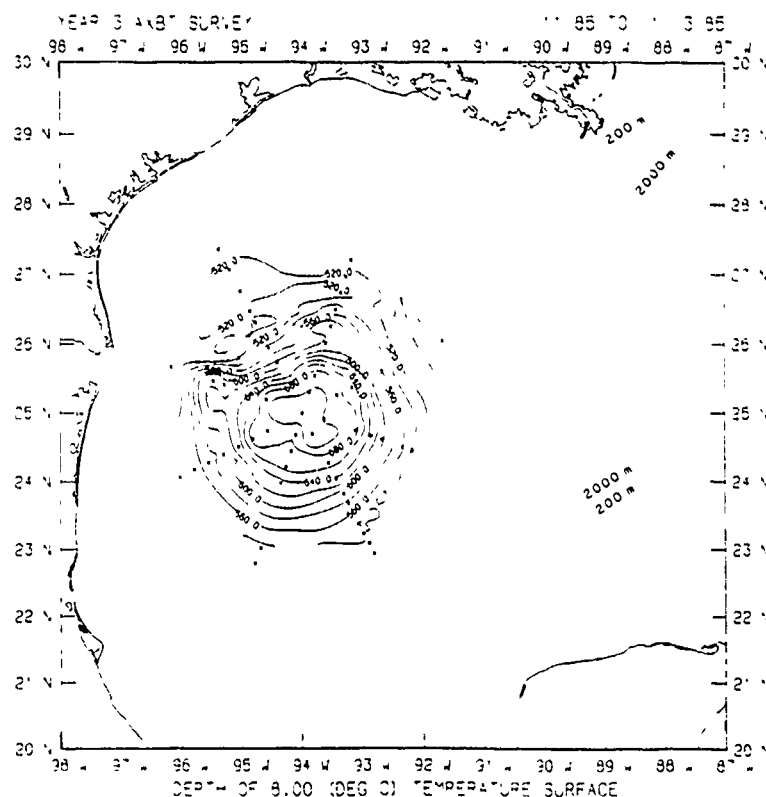


Fig. 6. Depth of the 8°C isotherm from the AXBT survey of November 11–13, 1985

~24.5°N with its southern edge reaching at least to 22.5°N. By January 22–28, 1986 (Figure 9), the flow field had become much less elongated and elliptical. A cyclonic feature to the northwest of the anticyclone is readily apparent in the SST data. A hydrographic cruise was conducted during this period, from January 23 to February 5, 1986. The surface dynamic height field relative to 800 m is shown in Figure 10. The cyclone-anticyclone pair is readily discerned, and the movements of the drifters were tightly coupled to this dynamic topography.

The evidence presented above would suggest that the surface waters of Ghost Eddy had been pulled around to the west and north of Fast Eddy and that a coalescing process between the two rings might be occurring. This evidence includes the movement of the drifters out of Ghost Eddy, a tongue of warm water originating at the northern edge of Ghost Eddy and moving northward up to 27.5°N, and the reconsolidation of the Ghost Eddy drifters into Fast Eddy. Additional evidence will be presented in the following section.

We finally note that the recently shed Hot Eddy is easily discerned by the 24°C and 25°C isotherms in Figure 9. Drifter 5678 was along the northwestern edge of this new ring, rotating in a cyclonic fashion as depicted in Figure 9.

#### Reflection and Dissipation

For the next 3½ months (to mid-May 1986), Fast Eddy continued to persist off the Mexican coast. Maximum swirl speeds were 75 cm/s at a radius of 80 km, but this occurred in mid-February 1986. During March–May, the surface characteristics of Fast Eddy became less energetic and less well organized. Drifter trajectories for February 26 to April 22,

1986, are shown in Figure 11. Fast Eddy had moved eastward, and drifter 5678 had become entrained in the anticyclonic flow regime of Hot Eddy. Fast Eddy became quite elliptical as Hot Eddy approached, with a distinct east-west elongation for the flow field of Fast Eddy by mid-March.

Hot Eddy continued moving southwestward across the deepest regions of the GOM. By the end of April, the flow field of the older Fast Eddy became quite irregular, and the center of Hot Eddy had reached 91°W, 25°N. Drifters 3353 and 5678 appeared to have been influenced by the newer ring's western and northern flow fields, respectively. Drifter 3378 was heading south into the Campeche Bay region.

A set of XBT data was collected in the western GOM during the period of April 26 to May 14, 1986. The depth of the 8°C isothermal surface is shown in Figure 12. The results indicate a smaller but still intense cyclone-anticyclone pair centered at about 95.5°W, 24°N. Drifter 3378 went as far south as 22°N, then moved northward along the western side of the cyclone-anticyclone pair, and finally turned eastward at about 25.5°N.

#### Interaction With Hot Eddy

At the time that drifter 3378 turned eastward, a curious event occurred which involved Hot Eddy. Trajectories for May 14–24, 1986 are shown in Figure 13. As drifter 3378 moved eastward, drifter 3379 began to drift toward the west at ~24°N. At about 94°W, drifter 3379 abruptly turned northward to complete the outline of an elongated ellipse with an east-west orientation. Drifter 3379 then continued its anticyclonic rotation, but drifter 3378 kept moving eastward toward the Loop Current. By June 21, 1986, drifter 3378 had moved northward around the Loop Current and left the



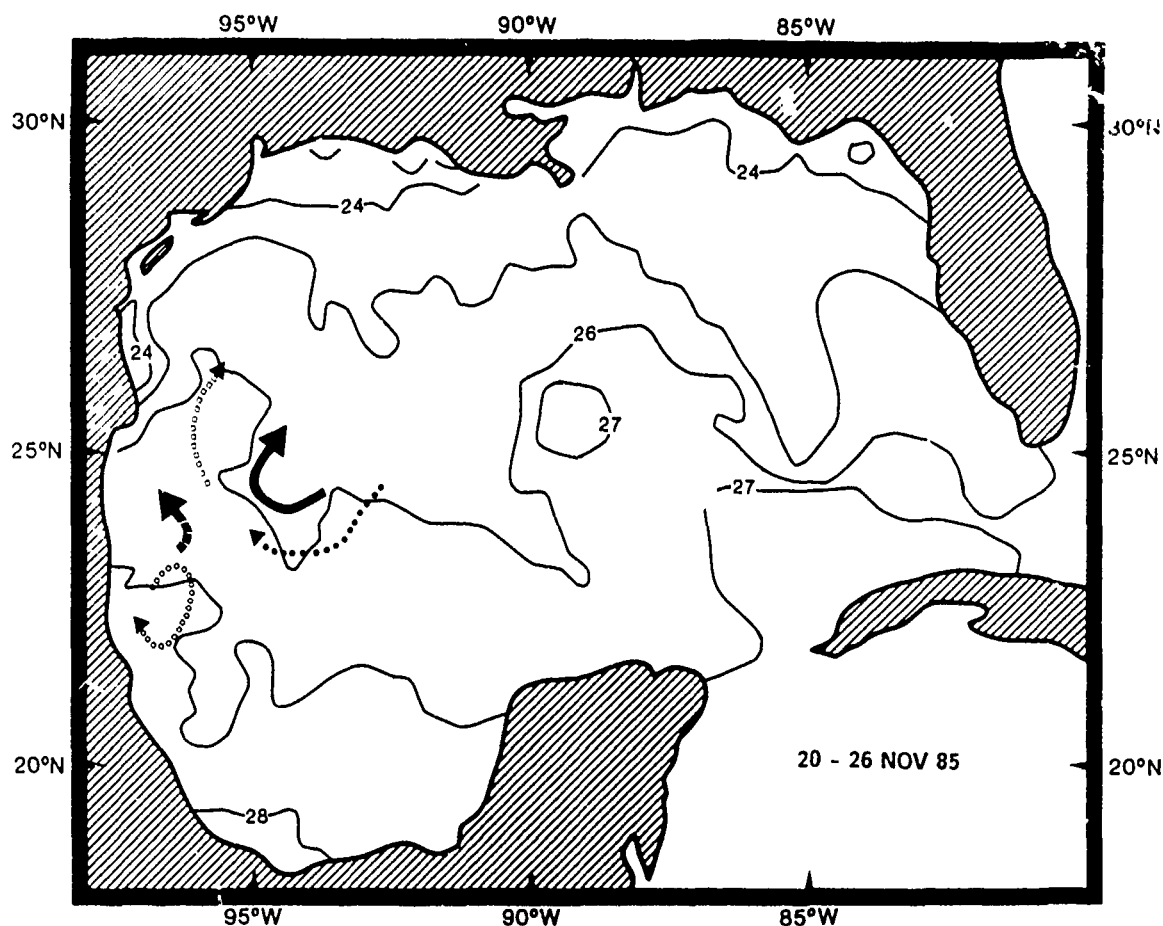


Fig. 7 Sea surface temperature (degrees Celsius) for November 20–26, 1985. The corresponding trajectories of drifters are shown by arrows (3378, black line, 5495, open circles, 5683, solid circles, 5678, open squares, 3353, solid squares).

GOM through the Florida Straits in mid-July 1986. On the other hand, Hot Eddy had reached the Mexican coast at  $\sim 24^\circ\text{N}$  (Figure 14) within a 3-week period. At that time, drifter 3379 began making large, anticyclonic loops in the western gulf and continued this type of motion through August 1986. These loops covered almost  $4^\circ$  in latitude and longitude. An XBT survey was conducted during August 16–22, 1986 (Figure 15), and the  $8^\circ\text{C}$  isothermal surface indicates a large anticyclone centered somewhere south of  $23^\circ\text{N}$ .

#### 4. DYNAMICAL INTERPRETATIONS

There are several aspects of the life of Fast Eddy that we wish to discuss. These will be broken down into four topics: the westward drift across the GOM, the interaction with Ghost Eddy, the gradual dissipation, and the interaction with Hot Eddy.

##### *Westward Motion After Separation From the Loop Current*

Previous drifter-tracked rings as well as Hot Eddy all moved southwestward across the deepest portions of the GOM [Lewis and Kirwan, 1985]. But Fast Eddy is the first drifter-tracked ring that followed a more westerly path paralleling the northern continental slope of the gulf. The

southwesterly path can be explained by simple notions of topographic steering of rings. However, the route along the northern continental slope cannot be so easily explained.

For example, the westward translation of Fast Eddy moves the northern portion of the ring over bottom topography that is substantially shallower than the southern portion. Current data from Fast Eddy as it approached the western gulf showed that the flow field extended to greater than 3000 m [Science Applications International Corporation (SAIC), 1988], which is typical for GOM rings [Hofmann and Worley, 1986]. Considering the spatial extent of this ring when it detached from the Loop Current (Figure 16), the movement of the center of the ring onto the 3000-m isobath would mean that the circulation would flow from depths as shallow as 1200 m in the north to greater than 3000 m in the south. Thus by following the more westerly path, the ring circulation is forced into a drastically different topographic environment relative to the conditions at its formation. This is quite surprising considering the present level of understanding of ring dynamics.

Associated with the movement into shallower water, we find several interesting points. First, a simple notion of the conservation of potential vorticity implies that Fast Eddy should exhibit divergence as it moves into shallower water. However, analysis of the drifter data (Figure 17) indicates just the opposite. During Julian days 235–255, the distance of

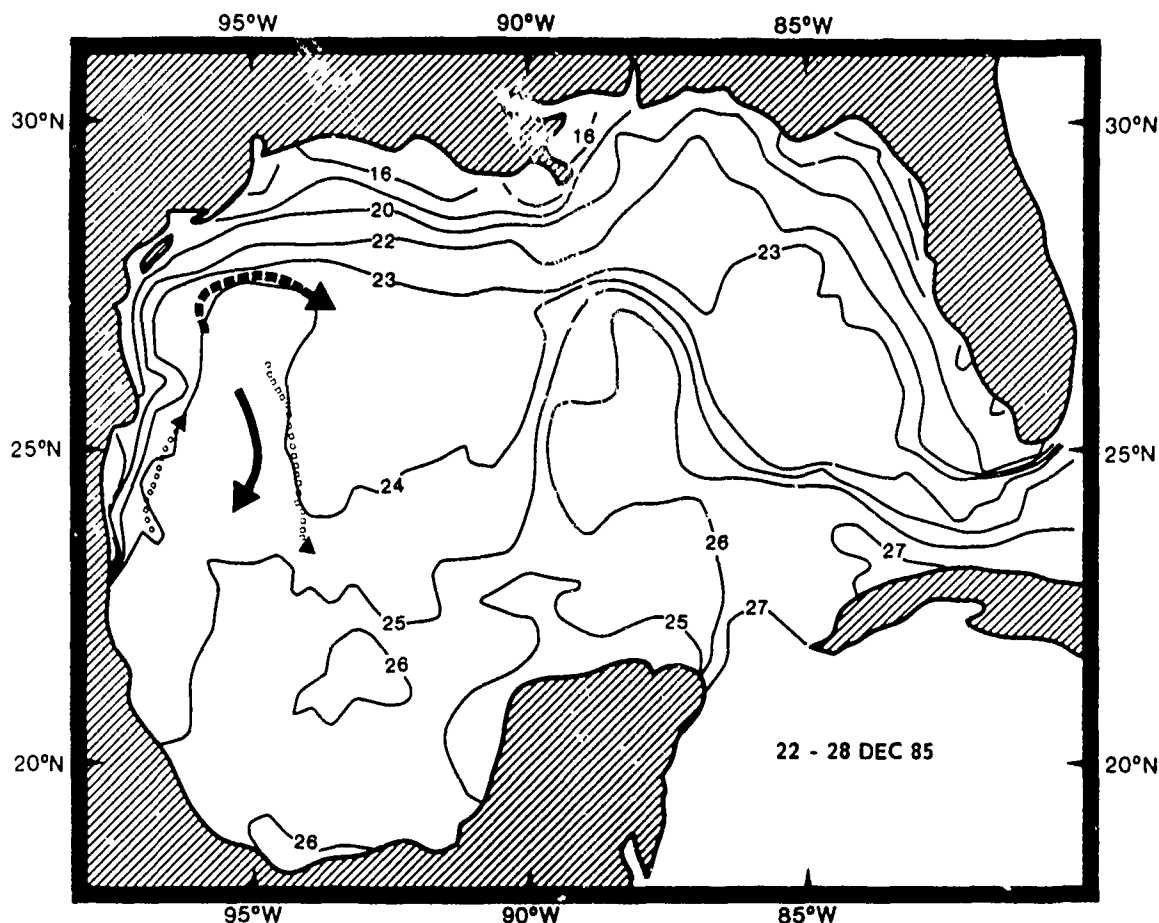


Fig. 8 Sea surface temperature (degrees Celsius) for December 22-28, 1985. The corresponding trajectories of drifters are shown by arrows (3378, black line; 5495, open circles, 5683, solid circles, 5678, open squares, 3353, solid squares)

drifter 3378 to the center of Fast Eddy decreased from approximately 80 to 60 km. Other puzzling aspects of the motion of Fast Eddy are its stalling after moving onto the 3000-m isobath and its subsequent abrupt southward jump back into deeper water.

We will now consider some of these puzzling aspects of Fast Eddy, first addressing its westward motion onto the 3000-m isobath. Based on our present understanding of ring dynamics, there is no internal mechanism that would cause the ring to migrate onto the shallow bathymetry to the north. This means that only external processes could have contributed to the westward movement of the ring. Possible candidates are atmospheric forcing, and the presence of nearby but unobserved flow structures such as cyclones, anticyclones, and shelf-slope circulation. Atmospheric forcing seems the least likely, since it would be of short duration with effects confined mostly to the mixed layer ( $\sim 20$ – $30$  m). By the same reasoning, shelf circulation is not a likely candidate, as its effects are confined to the upper 200 m at most. In addition, the speeds associated with the Texas-Louisiana shelf circulation are about an order of magnitude less than the swirl speed of the ring [Cochrane and Kelly, 1986].

Note in Figure 2 that Ghost Eddy was quite close to Fast Eddy prior to its movement onto the 3000-m isobath. This raises the possibility that these two large rings interacted in a way to force Fast Eddy along its more westward route

However, the interaction of the flow fields of two anticyclones results in the rotation of the pair in an anticyclonic sense [Hooker, 1987; Cresswell, 1982]. Such an interaction would result in Fast Eddy's rotating southeastward and away from the continental slope. Moreover, two interacting vortices with the same rotation tend to coalesce, being drawn together as their flow fields merge [Chang, 1983; Nof and Simon, 1987]. There is no indication of such a coalescence at that time.

There is another external flow field that could have interacted with Fast Eddy to move it into shallower water and that cannot be as easily dismissed as the previous candidates. It is well known from theory and model studies that a translating anticyclone will radiate energy in its wake in the form of vortices of alternating sign [e.g., Smith and O'Brien, 1983]. Thus one could expect a trailing cyclone northeast of Ghost Eddy. (Figure 18 shows such a cyclone associated with Hot Eddy when it was at  $\sim 90.4^\circ$ W). This suggests that the motion of Fast Eddy onto the 3000-m isobath could have been the result of an interaction with a cyclone of Ghost Eddy. A cyclone-anticyclone pair will translate in the direction of the flow of water along their common boundary [Hooker, 1987]. With Ghost Eddy being southwest of Fast Eddy, this would mean a northwestward movement, bringing Fast Eddy onto the continental slope. The implication is that Loop Current rings move along the northern slope of the GOM as a result of a previous ring already being in the

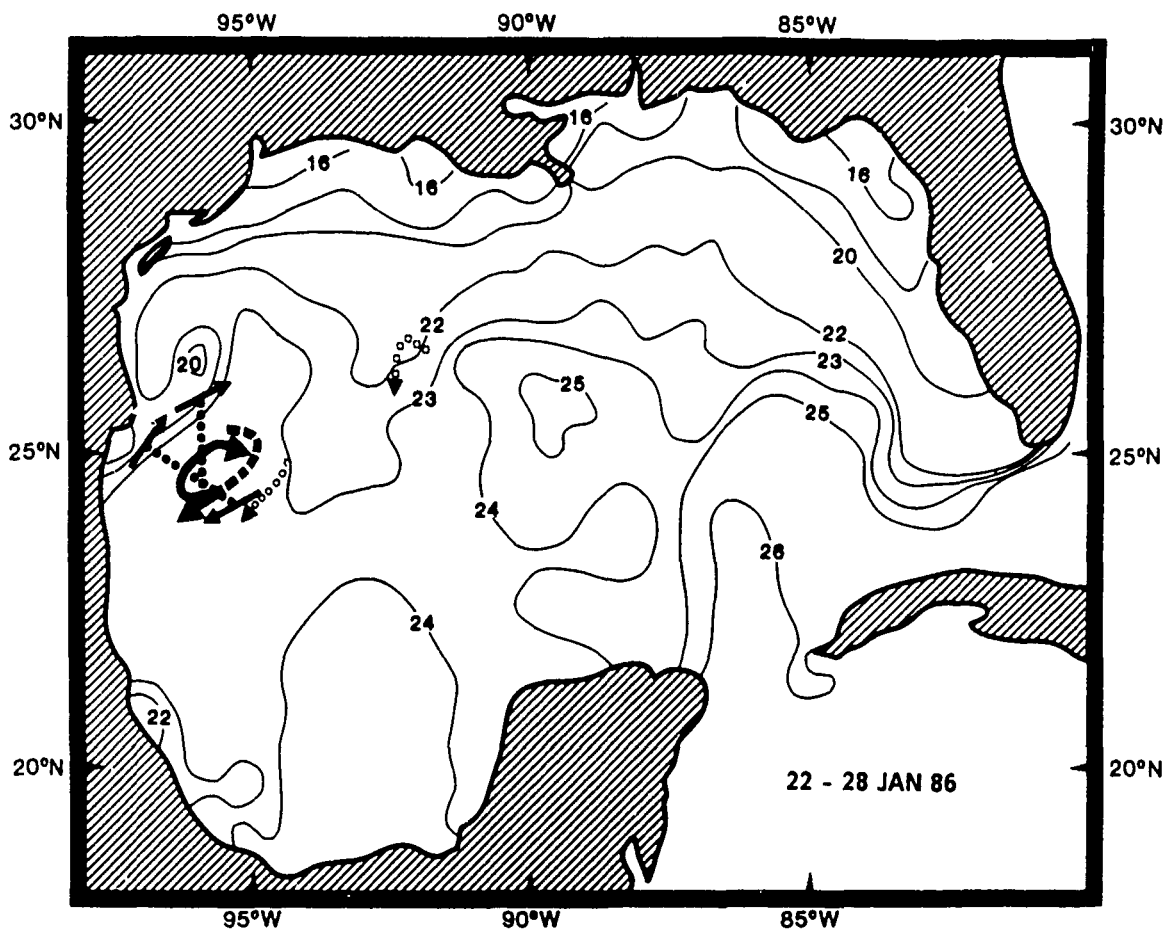


Fig. 9. Sea surface temperature (degrees Celsius) for January 22-28, 1986. Shorter arrows denote the flow at the edges of Fast Eddy, while dotted lines indicate the locations of ring waters (based on XBT data). The corresponding trajectories of drifters are shown by arrows (3378, black line; 5495, open circles; 5683, solid circles; 5678, open squares; 3353, solid squares).

deeper waters of the central gulf. The direct cause is the younger ring's interaction with the wake (cyclone) of the older ring. Direct observations of this effect would be difficult but highly desirable.

Stalling of Fast Eddy on the 3000-m isobath is likely a common event for rings traveling along the northern GOM slope. Westward propagation can be explained by the beta effect on individual water parcels within the ring [Smith and O'Brien, 1983]. But when the ring feels the effect of bathymetry to the north, nonlinear accelerations can become important [Smith, 1986]. The narrower and shallower region along the northern edge of the ring causes an acceleration and an increase in momentum. This effect is readily seen in the kinematic data of drifter 3378 in which the calculated period of rotation was decreased by ~2 days whenever the drifter was on the northern side of the ring during the period of the stall. Geostrophic current calculations for Fast Eddy also show this effect in terms of increased current speeds in the northern part of the ring [SAIC, 1988]. As a result, the eastward flowing water north of the ring center exceeds the westward flow to the south, thus counteracting the beta effect. The stalling of Fast Eddy likely is the result of a balance between the westward tending beta effect and the eastward tending nonlinear acceleration.

Still to be accounted for is the fact that the orbits of drifter 3378 became smaller as Fast Eddy moved on and stalled on

the continental slope. One clue to what may have occurred is found in the XBT data. Table 3 shows the maximum depths of the 8°C isotherms for various surveys. Also shown are the volumes between the 15°C and 8°C isothermal surfaces as determined from the intersection of the 8°C isotherm with the 550-m depth. If one considers the first two cruises, it is seen that the depth of the 8°C isotherm decreased by 5 m but the volume between the 8° and 15°C surfaces increased considerably. The net result is a substantial growth of Fast Eddy from the period between when it was spawned and after it moved southward off the 3000-m isobath. A rough estimate of the growth using the 8° and 15°C data is an increase of ~60%. This implies that Fast Eddy entrained a substantial amount of water. Such a process is consistent with the paths of drifters 5683 and 5678 (Figures 4 and 5). These drifter data indicate that the source of the water was the warm shelf waters of the northern GOM. Similar entrainments for Gulf Stream warm-core rings are shown in some excellent satellite images by Garfield and Evans [1987].

Stern [1987] has shown that entrainment results from the engulfing of outlying waters by an unstable wave form traveling cyclonically around the edge of a warm-core ring. The unstable wave is a Kelvin-Helmholtz type and breaks (crest traveling faster than the rest of the wave) to entrain water outside of the eddy. Stern has shown that the instability can be initiated by an offset of the center of the eddy

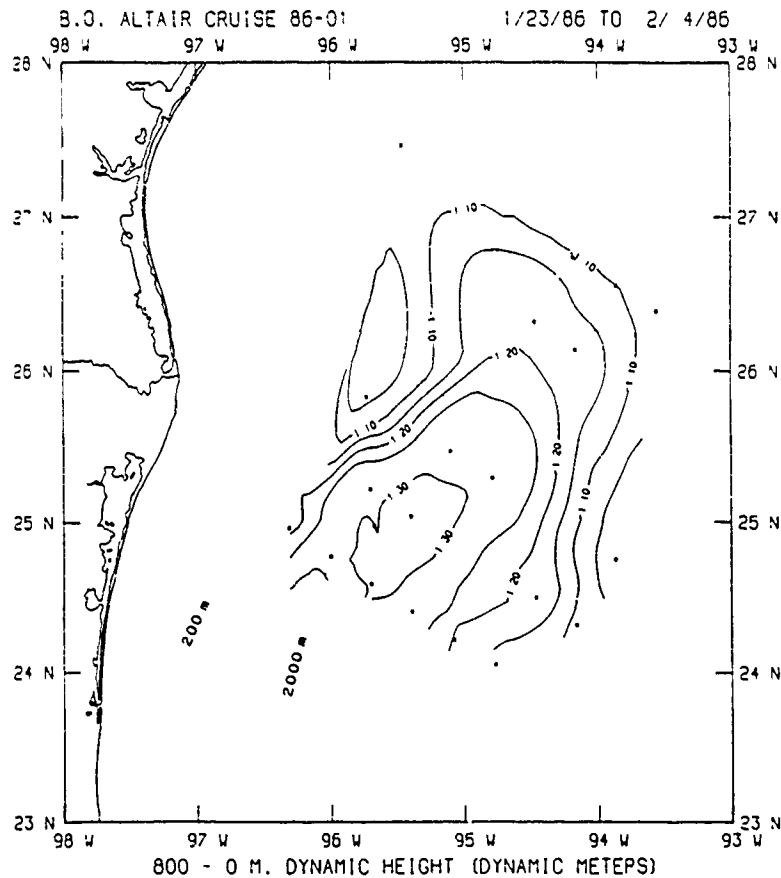


Fig. 10. Surface dynamic topography (centimeters) with respect to 800 m from the survey of January 23 to February 4, 1986.

with respect to its outside edge, a distinct possibility for a ring that has encountered a shelf slope. However, Stern [1987] also indicates that the symmetry of an eddy could be perturbed by an exterior velocity field. This too could be a cause of the entrainment for Fast Eddy considering the cyclonic flow field that has been discerned on the Texas continental shelf by Cochran and Kelly [1986].

The entrainment process explains both the decrease in the radius seen by drifter 3378 and the abrupt offshore jump made by the ring. First, the entrainment of shallow, warm shelf water would produce a convergence in the top layer of

Fast Eddy. The convergence would then produce smaller drifter orbits. Upper layer entrainment would have to be compensated by divergence in the lower layers of Fast Eddy. Some portion of the decrease in ring radius after moving off the 3000-m isobath could be the result of vortex stretching as the ring goes into deeper water. Assuming the ring extends to the bottom at all depths of the GOM, vortex stretching can only account for a third of the decrease in ring radius. The remainder must be attributed to mass entrainment in Fast Eddy. Overall, the net decrease in the ring radius indicates a volume increase of 50%, quite consistent with the 60% estimate obtained using the 8° and 15°C isotherm data.

The entrainment process can also account for the southward movement of Fast Eddy into deeper water. To illustrate this, consider the simplified case of a vortex undergoing solid-body rotation. The conservation of mass and potential vorticity over the volume of the vortex are

$$dH/dt + HD = Q$$

$$d(\zeta + f)/dt + D(\zeta + f) = 0$$

where  $H$  is the average depth (assuming the ring reaches to the bottom),  $t$  is time,  $D$  is the horizontal divergence (negative in the case of entrainment),  $Q$  is some source of mass (the mass entrainment process),  $\zeta$  is the vertical component of vorticity, and  $f$  is the Coriolis parameter. Eliminating  $D$  between the two equations gives

$$d[\ln(\zeta + f)/H] dt = -Q/H$$

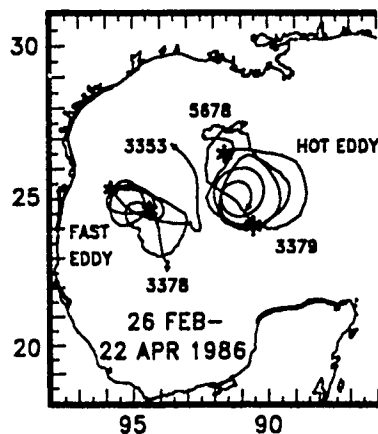


Fig. 11. Drifter trajectories for February 26 to April 22, 1986. Asterisks represent the initial positions of the drifters.

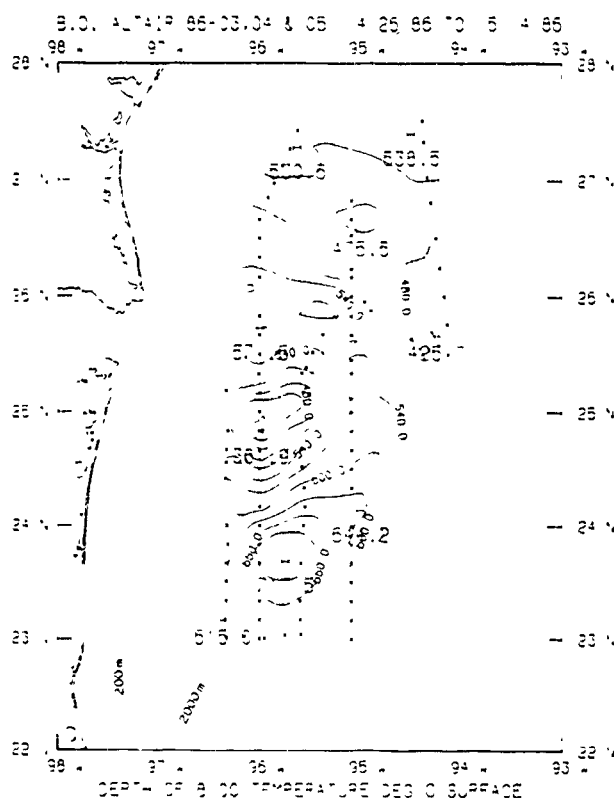


Fig. 12. Depth of the 8°C isotherm from the XBT survey of April 26 to May 14, 1986.

Since  $Q$  is positive for entrainment, the above implies that  $(\zeta - f)H$  must decrease. This can be accomplished by increasing  $H$  and/or decreasing  $\zeta - f$ . For Fast Eddy, the latter varies by at most 5% while the former varies by 30%.

This simplified example qualitatively demonstrates the role of entrainment on the vorticity tendency of the vortex. It suggests that a more detailed study of the effect of entrainment on baroclinic vortices in the presence of sloping topography is required before a complete understanding of this process is available.

We have discussed the significant events during Fast Eddy's westward translation, but we have yet to comment on the general dynamics within the ring as it drifted west.

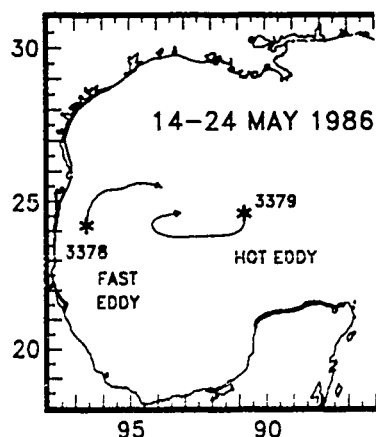


Fig. 13. Drifter trajectories for May 14–24, 1986. Asterisks represent the initial positions of the drifters.

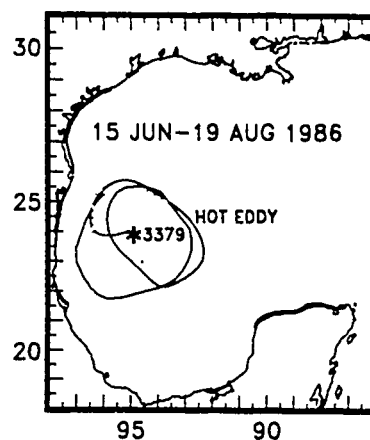


Fig. 14. Drifter trajectories for June 15 to August 19, 1986. Dotted lines indicate the locations of ring waters (based on XBT data) and the edges of Fast Eddy. Asterisks represent the initial positions of the drifters.

This can be done with some of the results of the kinematic analysis and parameters from dynamical models of eddies. We have considered the analytical solutions for an isolated eddy first presented by Ball [1963, 1965] and extensively described by Cushman-Roisin et al. [1985]. They start with the governing equations for a warm core eddy in a reduced-gravity environment on an  $f$  plane. Cushman-Roisin et al. found that the equations of motion reduced to a set of nonlinear, coupled, ordinary differential equations if (1) the velocity of the fluid within the eddy varied linearly with distance from the ring center and (2) the depth variations of the warmer waters of the eddy were a quadratic function of space. The latter assumption is quite reasonable for Fast Eddy. The rms errors of fits of elliptical paraboloids to the isotherm depths measured during July 16–19, 1985 (e.g., Figure 16), were only  $\sim 10$  m.

The dynamical components of the Cushman-Roisin model are the reduced-gravity horizontal pressure gradient, the Coriolis effect, and the local plus nonlinear acceleration terms. Cushman-Roisin et al. showed that the axes of an elliptical warm-core eddy would have a subinertial, anticyclonic rotation. The kinematic analyses were used to determine to what extent the Cushman-Roisin et al. model could be applied to Fast Eddy. Appropriate expressions from Cushman-Roisin et al. were numerically integrated to give the length and orientation of the eddy axes. The reduced-gravity formulation requires a temperature structure described by the depth of the upper layer of water and a vertical temperature difference at the eddy center. On the basis of the XBT data of July 16–19, 1985, we used a depth of 300 m with a temperature difference of 6°C. The results of the numerical integration were compared with the elliptical orientation information provided by the kinematic analysis. The lengths of the axes were taken from the estimates of the distances to the locus of the 20°C isotherm at a depth of 125 m (as opposed to the distance to the drifter itself). Since the deviation of the analytical solution from the observations increases with time, the calculations were restarted every 20 days ( $\sim 2.5$  orbital periods).

The orientations of the observed and model minor axes are shown in Figure 19. The occasional erratic behavior in the observations occurred when the eddy was nearly circular. The observed and model axes rotated anticyclonically at

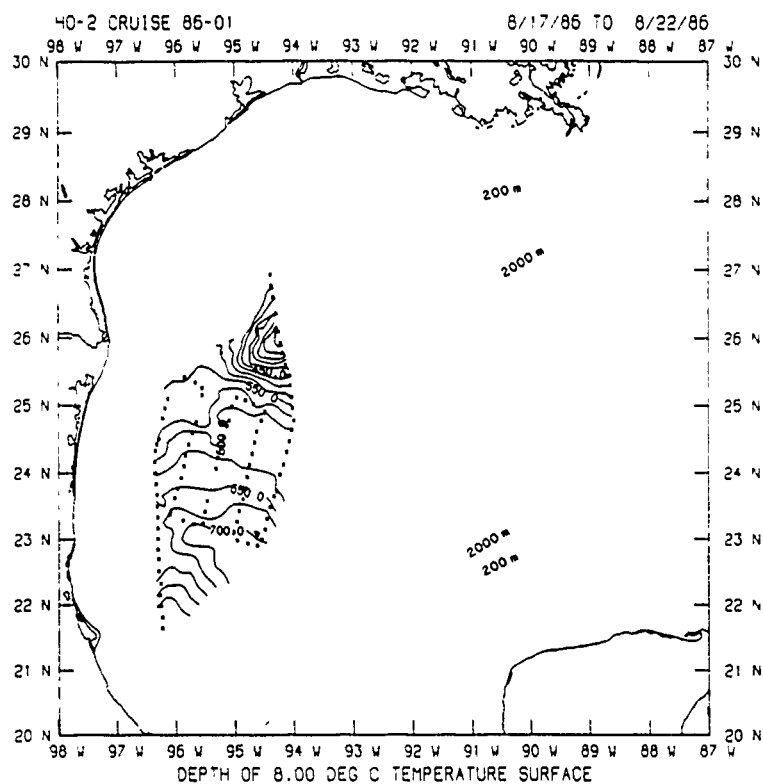


Fig. 15. Depth of the 8°C isothermal surface from the XBT survey of August 17-22, 1986

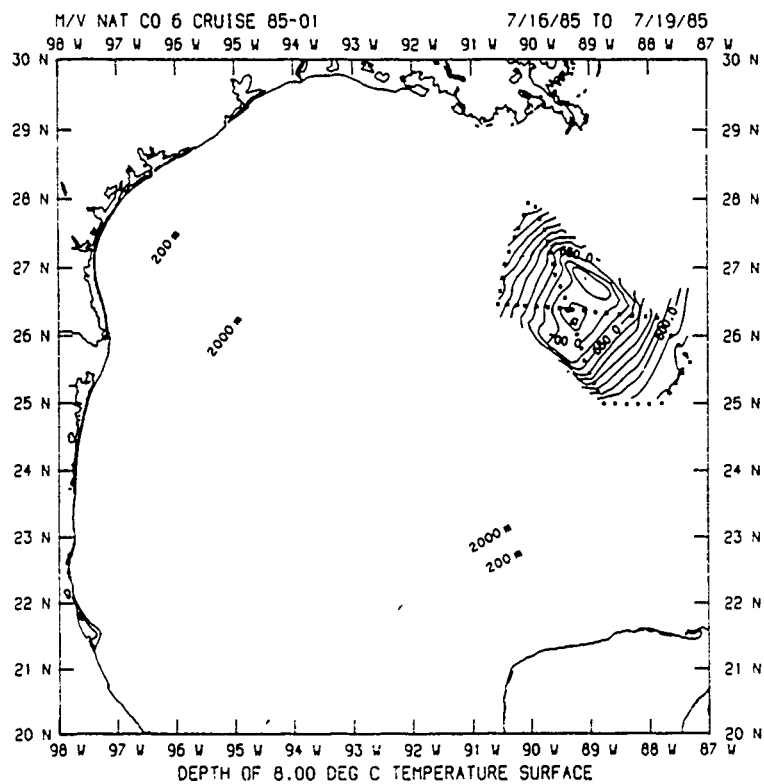


Fig. 16. Depth of the 8°C isothermal surface from the XBT survey of July 16-19, 1985

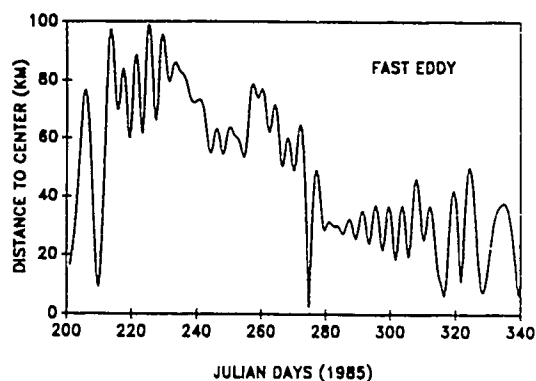


Fig. 17 Distance to the center of rotation of Fast Eddy as seen by drifter 3378 (calculated following Kurwan *et al.* [1988])

almost the same rate, an average of  $3^\circ$  per day. The model results are impressive in that they follow the observed axis orientation on relatively short time scales (1–2 days). The model is for an isolated eddy, and as noted by Cushman-Roisin *et al.*, the model rotation rate depends only on the ratio of the eddy size to the radius of deformation. Interactions with Ghost Eddy and the bathymetry thus seem to have had little effect on the orientation of Fast Eddy.

The observed and modeled major and minor axis lengths are shown in Figure 20. Although the model predictions follow the observations for much of the modeled period, the model is not significantly more accurate than a forecast based on persistence. The model does not follow the observed growth of the major axis from Julian days 270 to 300. If this growth is due to entrainment, then we would not expect it to be described by a model of an isolated eddy. On the other hand, the observed axis lengths do not seem to show any effects from the close proximity of Ghost Eddy during days 210–240. The axis lengths predicted by the model often show in-phase oscillations with periods about the same as the orbital period. The observations show similar oscillations, especially after Julian day 250 (Figure 20). However, these oscillations are out of phase.

TABLE 3. Estimates for Fast Eddy of the Vertical Extent of the  $8^\circ\text{C}$  Isotherm and of the Volume of Water Between the  $8^\circ\text{C}$  and  $15^\circ\text{C}$  Isothermal Surfaces

Date of Survey	Maximum Depth of the $8^\circ\text{C}$ Isotherm, m	Estimated Mass Between $15^\circ$ and $8^\circ\text{C}$ at 550 m, $10^{11}\text{ m}^3$
July 16–19, 1985	760	1.67
Oct. 22–27, 1985	755	2.67
Nov. 11–13, 1985	710	2.82
Jan. 23 to Feb. 5, 1986	810	2.46
April 26 to May 14, 1986	720	1.37
Aug. 16–22, 1986	>700	3.92

These estimates are used as indicators of the changes in the size of the ring between various cruises.

The above comparisons are encouraging. The physics of a reduced-gravity, nonlinear eddy seem appropriate for Fast Eddy during various periods of its westward translation across the gulf. This is somewhat remarkable, since the reduced-gravity model applies to an isolated, shallow, lens-like eddy lying over an infinitely deep inert layer.

Probably one of the most significant consequences of an elliptical, rotating eddy is the presence of an oscillatory deformation field within the eddy. The reader is referred to Cushman-Roisin *et al.* [1985] for an excellent discussion of this phenomenon. The oscillatory deformation field results in each fluid parcel being relatively close to all others at some time during the full period of rotation of the eddy axes. The effects of lateral mixing (the Cushman-Roisin *et al.* model has no such mixing) along with this phenomena would greatly enhance the homogeneity of the fluid within an eddy. This process is greater for more eccentric eddies. From this one may conclude that the greater eccentricity that results from entrainment or ring-ring coalescing also aids in the mixing of the water masses to produce a final uniform water mass rather quickly.

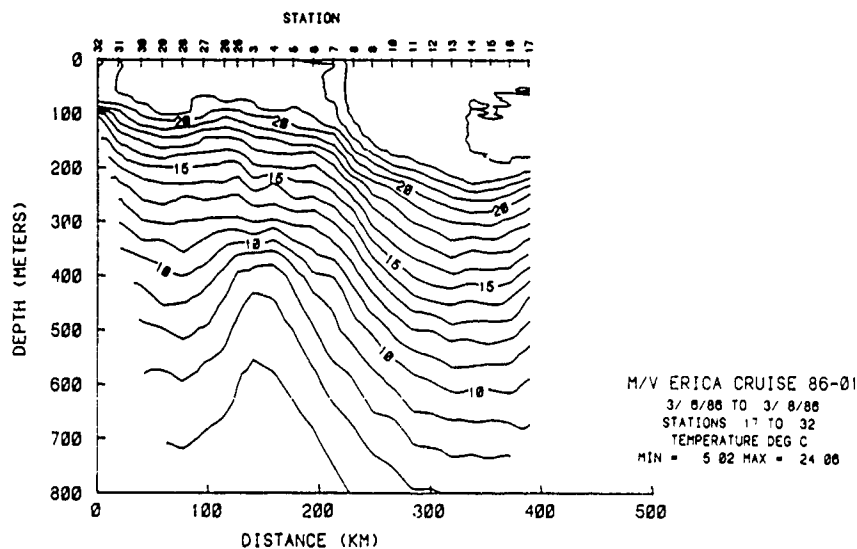


Fig. 18 A north-south XBT transect through Hot Eddy during March 6–8, 1986. The transect was just south of the Mississippi delta, at  $\sim 90^\circ 4'\text{W}$ , from  $24^\circ 8'\text{N}$  (station 17) to  $28.5^\circ\text{N}$  (station 32). The drop in the isotherms from station 25 to 28 indicates a deep cyclone north of the main body of Hot Eddy (stations 8–17) and south of the continental slope (stations 30–32).

### Interaction With Ghost Eddy

After moving into deeper water and crossing the GOM, Fast Eddy began interacting with the western boundary of the gulf. This interaction consisted of deformation caused by the bathymetry and coalescence with Ghost Eddy. On approaching the northwestern corner of the gulf, Fast Eddy underwent considerable deformation (Figure 21). As a result, the ring became more elongated but with a variable orientation of the ellipse (Figure 22). Swirl speeds as detected by drifter 3378 were of the order of 25 cm/s.

Figure 7 shows that Fast Eddy had begun to interact with Ghost Eddy at least as early as November 25, 1985. At the beginning of this interaction, the elliptical orientation of Fast Eddy was northwest to southeast with an eccentricity varying between 2 and 5 (Figure 22). This changed abruptly to a north-south orientation with an eccentricity as great as 7.0. This corresponds to the time that the tongue of warm water penetrated far north over the Texas continental slope and shelf (Figure 8). As the water mass became more consolidated (January 1986), the resulting anticyclone took on a northeast-southwest orientation and became more circular (Figure 22).

The previously presented hydrographic and SST data indicate that Fast Eddy had coalesced completely with Ghost Eddy. The coalescence process has many of the same features as one reported by Lewis and Kirwan [1985]. However, the trajectories of all the drifter data indicate a rather specific coalescence process. It appears that much of the mass of Ghost Eddy was stripped off by Fast Eddy and pulled to the west of the younger ring, with some water being thrown well north of the center of Fast Eddy. Most of the water then returned to an orbit about Fast Eddy. The process is kinematically reminiscent of a binary star system in which the mass of the smaller star is whirled far out into space beyond the larger star before eventually falling into the latter. In the case of the GOM, the larger and more intense Fast Eddy would pull the waters from the older Ghost Eddy. (With momentum being proportional to the radius squared, Fast Eddy had at least 4 times the momentum as Ghost

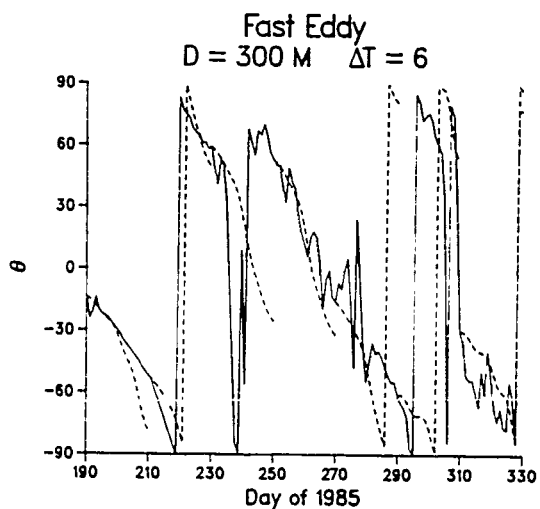


Fig. 19 Orientation of the minor axis of an elliptical fit to the shape of Fast Eddy. The solid line was determined by the trajectory of drifter 3378. The dashed line was determined using the model of Cushman-Roisin et al. [1985] with a 300-m center depth of an anticyclonic eddy with a vertical temperature difference of 6°C.

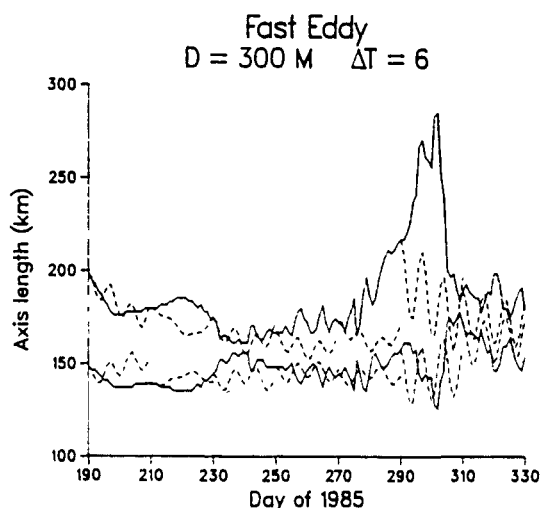


Fig. 20 Variations in the lengths of the major and minor axes of Fast Eddy. The solid line was determined by the trajectory of drifter 3378 and XBT data. The dashed line was determined using the model of Cushman-Roisin et al. [1985] with a 300-m center depth of an anticyclonic eddy with a vertical temperature difference of 6°C.

Eddy; see Figure 5). With the decay of Ghost Eddy, divergence in the upper layers would be ejecting warm water from the ring's central region. The drifter and SST data indicate that Fast Eddy took approximately 1 to 1.5 months to extract and incorporate the waters of Ghost Eddy.

After a tongue of lighter water is jetted northward over denser, colder water, a near-geostrophic balance would be expected to be established at the interface. This would produce a northward flow along the west side of the tongue and a southward flow along the east side of the tongue. Thus by this argument, the water of Ghost Eddy would return to circulate around Fast Eddy.

The 8°C isotherm data of January 23 to February 5, 1986 (Table 3) indicate the extent of the coalescence process. The volume of water between the 8°C and 15°C surfaces decreased slightly, but the maximum depth increased dramatically by 100 m. The implication is that the coalescence process consisted of the influx of warmer water from the south, and these warmer waters converged at the surface of Fast Eddy, resulting in the depression of isotherms.

### Dissipation of Fast Eddy

During February, March, April, and May 1986, Fast Eddy underwent a period of dissipation. Both drifters 3378 and 3353 showed anticyclonic motion until late March 1986. The net movement of the center of rotation was southward and somewhat offshore at about 24°N, consistent with the recent entrainment of water from Ghost Eddy. In about the third week of March 1986, both drifters left the ring and stopped their anticyclonic rotations. When the drifters left Fast Eddy, the distance to the center of rotation was ~80 km. The 8°C isotherm data of April 26 to May 14, 1986, showed a maximum depth of only 720 m (a decrease of 90 m in 3 months) and an estimated volume between the 8° and 15°C isotherms of  $1.37 \times 10^{13} \text{ m}^3$  (compared with  $2.46 \times 10^{13} \text{ m}^3$  for the previous survey). It is obvious that Fast Eddy had decayed substantially. The loss of both drifters is consistent with the weakening of the ring. As the isotherms rise, the surface layers undergo divergence, leading to ejection of



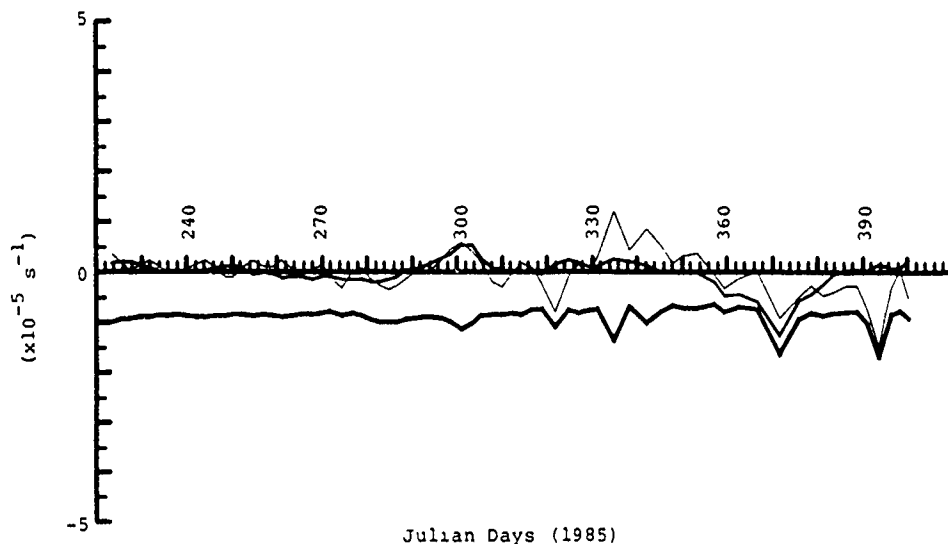


Fig. 21 Normal deformation rate, shear deformation rate, and vorticity for Fast Eddy

water from the eddy. (We note that this process is of a different nature than that of the interaction of Fast Eddy and Ghost Eddy. In the latter case, drifters were pulled out of Ghost Eddy as a result of water being extracted by a type of coalescence process, not a decay of the flow field.)

Still, the XBT data indicate that the ring was far from weak (the  $8^{\circ}\text{C}$  isotherm was still depressed beyond 700 m). But the loss of water from the surface layers of the eddy and the consequent increase in orbit size makes it difficult to use drifters to track a decaying ring such as this. However, interaction with a younger ring apparently acted to consolidate and revitalize this eddy.

#### Interaction With Hot Eddy

The XBT survey of April 27 to May 14, 1986 (Figure 12) shows a distinct closed, anticyclonic vortex in the western

GOM, the remnants of Fast Eddy. As Hot Eddy approached this vortex, drifter 3378 made a large, anticyclonic loop and passed on the west side of the anticyclone shown in the XBT data. At this point, the two anticyclones began an interaction as depicted in Figure 13. The peculiar factor of this interaction was the elongated elliptical path taken by drifter 3379. This "peanut"-shaped path had an east-west orientation, and the track occurred at the same time as drifter 3378 made a sharp eastward turn and began tracking eastward. This apparently is not an unusual phenomena, being seen in the trajectories of two previously drifter-tracked GOM rings [Kirwan *et al.*, 1984a, b; Lewis and Kirwan, 1985]. The subsequent XBT data from August 16–22, 1986 (Figure 15), shows an elongated, east-west feature with an  $8^{\circ}\text{C}$  isotherm maximum depth of  $>700$  m, a clear indication of an anticyclone in the western GOM. Although the depth of the  $8^{\circ}\text{C}$

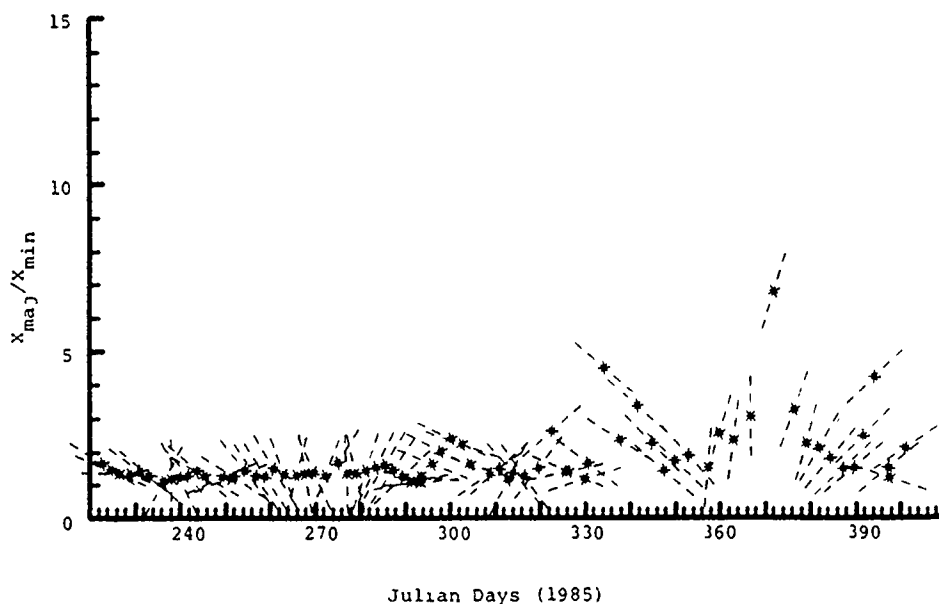


Fig. 22. Time histories for the eccentricity (asterisks) and major axis orientation (dashed line) for Fast Eddy. For the flow field orientation, north is in the positive eccentricity direction and east is in the positive time direction

isotherm had shallowed with respect to the previous survey, the estimated volume of the anticyclone appears to have grown substantially. Thus the interaction of rings 3378 and 3379 was apparently one of coalescence.

We do not have a complete enough data set to determine exactly how the two anticyclones coalesced. It is possible that they coalesced in a similar fashion as Fast Eddy and Ghost Eddy. However, during that previous coalescent process, there was no indication of the peanut phenomenon in any of the drifter paths. It is true that exaggerated elliptical trajectories were made during the coalescing of Fast Eddy and Ghost Eddy. But the elongated ellipse occurring during the interaction of Ghost Eddy and Fast Eddy went beyond and well north of the center of rotation of Fast Eddy. In the case of Fast Eddy and Hot Eddy, the peanut occurred in between the centers of rotation, a very distinct difference.

The other form of coalescence for vortices of the same sign is the gradual joining of streamlines as the rings touch [Chang, 1983]. In such a case, a more central streamline remains closed (around one center of rotation) until all outlying streamlines have merged with those of the other center of rotation. At that time, the streamline can merge with the corresponding streamline of the other vortex. The general shape of a recently merged streamline is that of a dumbbell or peanut. The details of this type of process has recently been examined by Nof [1988]. Nof showed that the actual coalescing process consists of intrusions of tentacles of water from each eddy. These intrusions establish what Nof terms as a "padlock" flow field about each eddy, with a characteristic peanut shape between the centers of rotation. With time, the tentacles become longer, and eventually the eddies are converted entirely into a single vortex of long, spirallike tentacles. At the latitude of Hot Eddy, the merging time would be approximately 30 days.

Although our data are not sufficient to establish the presence of tentacles of intruding water, Nof [1988] shows analytically and experimentally that such intrusions and tentacles are inevitable. Thus there are several strong pieces of evidence suggesting that Fast Eddy and Hot Eddy coalesced by the process described by Nof.

### 5. SUMMARY

Our results have provided a wealth of information pertaining to processes of Loop Current rings. This information plus previous research allows us to provide tentative answers to the questions we posed in the introduction. First, it appears that we may have up to four Loop Current rings shed per year. However, based on our sampling of such rings and their size and interactions, there are likely only a maximum of three such rings in the GOM at any one time. The dynamical mechanisms that determine the paths of GOM rings are (1) topographic steering in terms of the conservation of potential vorticity and (2) interactions with other rings. The interactions between a ring and topography or another ring appear to vary but can be explained by our present knowledge of eddy dynamics. Topographic interactions involve not only the conservation of potential vorticity but also the effects of nonlinear acceleration along the edge of the ring in shallower water. This latter effect accounts for the clockwise movement of GOM anticyclones along the shelf-slope regions of the gulf. Ring-ring interactions apparently range from simple coalescence, to more complex forms of merging, to subtle interactions between one ring and the

trailing vortices of another ring. The ultimate fate of any GOM ring is its coalescence with an older anticyclone in the western gulf. This process continually reenergizes an anticyclonic feature typically found along the coast of Mexico. But in the periods between such reenergizations, we can expect to find an anticyclone that may vary considerably in its characteristics.

There are several points that would provide the basis of some very interesting future work. The first is direct observation of the interaction between the vortices of an older ring and the movement of a younger ring. We are particularly interested in the phenomenon which causes GOM rings to move westward along the northern slope of the gulf. The second is a more detailed study of the entrainment of shelf waters and the effect that such a process has on a ring. It is indeed intriguing that entrainment can apparently set up a system of flow that affects water up to 300 km away along the Texas coast. Finally, the details of the coalescing of two GOM rings is of particular interest. This is not only because there appears to be different forms of coalescing, but also such a process can include a tremendous transfer of mass and heat as well as a temporary and perhaps dramatic convolution of the flow field.

**Acknowledgments.** This work was supported by the Minerals Management Service (MMS), contract 14-12-0001-29158 with Science Applications International Corporation. The authors wish to thank Cortis Cooper, the chief scientist on the discovery cruise of Fast Eddy, Horizon Marine for deploying many of the drifters, Murray Brown, who monitored this work for the MMS, and Maria Giuffrida who carefully prepared many of the figures. We appreciate the data management team at SAIC, Raleigh, North Carolina, who collected many of the data sets and produced a number of the figures. A. D. K. wishes to acknowledge the support of the Office of Naval Research through contract N00014-88-K-0101 with Old Dominion University and the Slover endowment.

### REFERENCES

- Ball, F. K., Some general theorems concerning the finite motion of a shallow rotating liquid lying on a paraboloid, *J. Fluid Mech.* 19, 240-256, 1963.
- Ball, F. K., The effect of rotation on the simpler model of motion of a liquid in an elliptic paraboloid, *J. Fluid Mech.* 22, 529-545, 1965.
- Chang, S. W., A numerical study of the interactions between two tropical cyclones, *Mon. Weather Rev.* 111, 1806-1817, 1983.
- Cochrane, J. D., Separation of an anticyclone and subsequent developments in the Loop Current (1969) in *Contributions to the Physical Oceanography of the Gulf of Mexico*, edited by L. R. A. Caprio and J. L. Reid, pp. 91-106, Gulf Publishing, Houston, Tex., 1972.
- Cochrane, J. D., and F. J. Kelly, Low-frequency circulation on the Texas-Louisiana continental shelf, *J. Geophys. Res.* 91(C9), 10,645-10,659, 1986.
- Cresswell, G. R., The coalescence of two East Australian Current warm-core eddies, *Science*, 215, 161-164, 1982.
- Cushman-Roisin, B., W. H. Heil, and D. Nof, Oscillations and rotations of elliptical warm-core rings, *J. Geophys. Res.* 90(C6), 11,756-11,764, 1985.
- Elliot, B. A., Anticyclonic rings and the energetics of the circulation of the Gulf of Mexico, Ph.D. dissertation, Tex. A&M Univ. College Station, 1979.
- Elliot, B. A., Anticyclonic rings in the Gulf of Mexico, *J. Phys. Oceanogr.* 12, 1292-1309, 1982.
- Garfield, N., and D. L. Evans, Shelf water entrainment by Gulf Stream warm-core rings, *J. Geophys. Res.* 92(C12), 13,003-13,012, 1987.
- Hofmann, E. E., and S. J. Worley, An investigation of the circulation of the Gulf of Mexico, *J. Geophys. Res.* 91(C12), 14,221-14,236, 1986.

- Hooke, S. B., Mesoscale eddy dynamics by the method of point vortices. Ph.D. dissertation, 158 pp., Univ. of Miami, Coral Gables, Fla., 1987.
- Hurlburt, H. E., and J. D. Thompson, A numerical study of Loop Current intrusions and eddy shedding, *J. Phys. Oceanogr.* 10, 1611-1651, 1980.
- Kirwan, A. D., Jr., W. J. Merrell, Jr., J. K. Lewis, and R. E. Whitaker, Lagrangian observations of an anticyclonic ring in the western Gulf of Mexico, *J. Geophys. Res.*, 89(C3), 3417-3424, 1984a.
- Kirwan, A. D., Jr., W. J. Merrell, Jr., J. K. Lewis, R. E. Whitaker, and R. Legeckis, A model for the analysis of drifter data with an application to a warm core ring in the Gulf of Mexico, *J. Geophys. Res.*, 89(C3), 3425-3438, 1984b.
- Kirwan, A. D., Jr., J. K. Lewis, A. W. Indest, P. Reinersman, and I. Quintero, Observed and simulated kinematic properties of Loop Current rings, *J. Geophys. Res.*, 93(C2), 1189-1198, 1988.
- Lewis, J. K., and A. D. Kirwan, Jr., Some observations of ring topography and ring-ring interactions in the Gulf of Mexico, *J. Geophys. Res.*, 90(C5), 9017-9028, 1985.
- Lewis, J. K., and A. D. Kirwan, Jr., Genesis of a Gulf of Mexico ring as determined from kinematic analyses, *J. Geophys. Res.*, 92(C11), 11,727-11,740, 1987.
- Merrell, W. J., and J. M. Morrison, On the circulation of the western Gulf of Mexico with observations from April 1978, *J. Geophys. Res.*, 86(C5), 4181-4185, 1981.
- Merrell, W. J., and A. M. Vazquez, Observations of changing mesoscale circulation patterns in the western Gulf of Mexico, *J. Geophys. Res.*, 88(C12), 7721-7723, 1983.
- Nakamoto, S., An application of soliton wave theory to meso-scale eddies in the Gulf of Mexico, Ph.D. dissertation, 54 pp., Dep. of Oceanogr., Tex. A&M Univ., College Station, 1986.
- Nof, D., The fusion of isolated nonlinear eddies, *J. Phys. Oceanogr.*, 18, 887-905, 1988.
- Nof, D., and L. M. Simon, Laboratory experiments on the merging of nonlinear anticyclonic eddies, *J. Phys. Oceanogr.* 17, 343-357, 1987.
- Science Applications International Corporation (SAIC), Gulf of Mexico physical oceanography program, Final report year 3, vol. II. Technical report, OCS Rep. MMS 88-0046, 241 pp., Gulf of Mex. OCS Reg. Off., Miner. Manage. Serv., U.S. Dep. of the Inter., New Orleans, La., 1988.
- Smith, D. C., IV, A numerical study of Loop Current eddy interaction with topography in the western Gulf of Mexico, *J. Phys. Oceanogr.*, 16, 1260-1272, 1986.
- Smith, D. C., IV, and J. J. O'Brien, The interaction of a two-layer isolated mesoscale eddy with bottom topography, *J. Phys. Oceanogr.*, 13, 1681-1697, 1983.
- Stern, M. E., Horizontal entrainment and detrainment in large-scale eddies, *J. Phys. Oceanogr.*, 17, 1688-1695, 1987.
- Thompson, J. D., Altimeter data and geoid error in mesoscale ocean prediction: Some results from a primitive equation model, *J. Geophys. Res.*, 91(C2), 2401-2417, 1986.
- Vukovich, F. M., and B. W. Crissman, Aspects of warm rings in the Gulf of Mexico, *J. Geophys. Res.*, 91(C2), 2645-2660, 1986.
- G. Z. Forristall, Shell Development Company, P.O. Box 481, Houston, TX 77001.
- A. D. Kirwan, Jr., Department of Oceanography, Old Dominion University, Norfolk, VA 23529.
- J. K. Lewis, Science Applications International Corporation, 1304 Deacon, College Station, TX 77840.

(Received July 13, 1988,  
accepted February 6, 1989.)

## Fractal drifter trajectories in the Kuroshio extension

By A. R. OSBORNE, *Istituto di Cosmogeofisica del C.N.R., Corso Fiume 4, Torino 10133, Italy*,  
A. D. KIRWAN, JR., *Department of Oceanography, Old Dominion University, Norfolk, VA 23508, USA*,  
A. PROVENZALE, *Istituto di Cosmogeofisica del C.N.R., Corso Fiume 4, Torino 10133, Italy*  
and L. BERGAMASCO, *Istituto di Fisica Generale dell'Università, Corso M. D'Azeglio 46,*  
*Torino 10125, Italy*

(Manuscript received 27 June 1988; in final form 2 February 1989)

### ABSTRACT

We study the fractal and scaling properties of the Lagrangian trajectories of three satellite-tracked, freely drifting buoys (drifters) placed in the Kuroshio extension region during 1977. Over a period of about one year, the drifters, whose positions followed approximately the motions of fluid parcels in the near-surface layer, traveled almost the entire width of the Pacific Ocean. During this time, the drifters followed what may be described as highly erratic paths, while on the average being advected eastward in the zonal flow. Here we apply four different data analysis methods, based on the mathematics of fractals, to the drifter paths. We find that for space scales extending from at least 20 to 150 km and time scales from 1.5 days to 1 week, each of the trajectories displays fractal and scaling behavior with a fractal dimension of approximately 1.3. The multifractal nature of the drifter trajectories is also explored. The implication of these results is that the near-surface Lagrangian mesoscale motions in the Kuroshio Extension exhibit fractal properties in a range of scales normally attributed to geophysical fluid dynamical turbulence. These results evidently provide the first experimental evidence that fluid parcel trajectories in large-scale ocean flows can exhibit fractal behavior. A relation between the observed value of the fractal dimension and the properties of the power spectrum of a typical drifter position coordinate is also exploited. We finally discuss some of the possible physical implications of these results for the study of geophysical fluid dynamical flows.

### 1. Introduction

The use of freely drifting, satellite-tracked surface buoys (drifters) and of deep subsurface SOFAR floats is a relatively recent development in the experimental study of large- and meso-scale ocean dynamics. These novel measurement techniques, which are crucially dependent upon remote-sensing technologies, have the capability of providing a large amount of information on the general circulation and on its variability. The trajectories of the drifters and of the floats represent a (quasi) Lagrangian description of the fluid flows since the free buoys may be considered to approximately follow the individual parcels of fluid in their motions throughout the ocean. While scarcely useful in tracking vertical

and convective motions, the drifter measurements are obviously best employed in determining some of the properties of large-scale, essentially two-dimensional, geophysical flows.

To quantitatively interpret the observations now available from several ocean regions, various approaches and time series analysis methods have been considered by different authors. Since large-scale motions may possess an energetic turbulent component, the drifter paths may be highly irregular and statistical approaches must consequently be employed. The techniques most commonly adopted may be grossly subdivided into two main categories, depending upon the scope of the analysis. The first approach is essentially based on considering the "ensemble" behavior of many trajectories, with the aim of

reconstructing the overall characteristics of the circulation. Some examples of these kinds of analyses are provided by Kirwan et al. (1978), McNally et al. (1983) and McNally and White (1985), who studied the circulation in the North Pacific; by Richardson (1983), who studied the mean kinetic energy distribution in the North Atlantic; by Molinari et al. (1981), who analyzed the surface currents in the Caribbean Sea, by Schmitz et al. (1981), Owens (1984), and Shaw and Rossby (1984), whose work was devoted to the study of the Gulf Stream and of the subtropical gyre with SOFAR floats; by Royer and Emery (1984), who studied the circulation in the Bering Sea, by Hofmann (1985), who analyzed the circulation in the Southern Ocean; and by Peterson (1985), who compared drifter data and current-meter measurements at Drake passage in the Southern Ocean. An extensive review of the drifter approach and of the technical problems related to the use of satellite-tracked drifters may be found in Kirwan and Cresswell (1982).

The second approach to the analysis of drifter data is in a sense complementary to the former and it is based on considering the statistical properties of the motions of individual drifters (single particle diffusion) or on two-parcel separation studies. In this context, Davis (1982, 1983) has provided a theoretical basis for analyzing single-parcel and two-particle statistics and for relating Eulerian and Lagrangian statistical properties. These studies represent an extension of classic approaches to Lagrangian diffusion in three dimensional, homogeneous and isotropic turbulence to geophysical fluid dynamical flows. The papers by Davis (1985) on the experimental program CODE and by Fahrbach et al. (1986) on the Atlantic Equatorial Undercurrent are recent examples of parcel separation studies in ocean flows.

In the present analysis, we consider a different approach and focus on the individual geometrical properties of three drifter trajectories in the Kuroshio extension region, a part of the Pacific Ocean known for its intense mesoscale variability. Although the drifter paths are quite irregular and apparently strongly different from each other, we show that there are some fundamental geometrical and statistical properties which are common to all trajectories. In particular we consider the fractal and scaling behavior

of the drifter motions and discuss how the fractal properties of the fluid parcel trajectories may be related to the dynamical motion. The study of the fractal properties of fully developed turbulent flows was stimulated over 15 years ago by the work of Mandelbrot (1972, 1974, 1975), who suggested for the first time that a full understanding of turbulent fluid flows requires consideration of the scaling and fractal properties of the motion. Here we concentrate on an unexplored aspect of the relationship between turbulence and fractals and provide original experimental evidence that fluid parcel trajectories in a large-scale ocean flow may be viewed as fractal curves with a fractal dimension of approximately 1.3. This research is a continuation of a previous study (Osborne et al., 1986), in which we considered the possibility that these Lagrangian observations of the dynamics in the Kuroshio extension could be interpreted in terms of deterministic chaos (for an introduction to deterministic chaos and related topics see, e.g., Eckmann and Ruelle, 1985). That analysis provided no evidence for low-dimensional chaos, but instead indicated that the drifter trajectories in the ocean surface layer displayed many of the characteristics of fractal curves. This paper is thus devoted to the systematic study of these fractal properties.

The approach taken here differs in at least 3 ways from other experimental studies on fractal properties of turbulent flows. First the analysis relies on Lagrangian data; hence we focus on the fractal nature of fluid parcel trajectories. We are not aware of any other experiments which have utilized particle trajectories to estimate fractal properties. A second important difference is that the data analyzed here come from a geophysical fluid dynamical (GFD) system whose dynamics are known to be significantly different from three-dimensional dynamics. Finally we stress that the data studied here come from a natural, large-scale system and not from a controlled laboratory experiment.

The use of Lagrangian data is particularly appropriate in the study of fractal behavior in that Lagrangian trajectories are amenable to at least four types of fractal analyses. Three of these techniques are devoted to the study of the so-called monofractal properties of the drifter trajectories. Of these the "yardstick" length and

the correlation dimension method provide information on spatial scales over which fractal and scaling properties hold. The third method, based on the calculation of the scaling exponent, gives comparable time scale information. Thus, the fractal analysis of Lagrangian data has the potential to give both time and space-scale information. The fourth method which we employ is based on the use of a box counting algorithm and is devoted to the study of the multifractal nature of the drifter data. This method also provides space-scale information.

Because of these attributes the data herein considered can also be used to address several basic issues in the fractal analysis of experimental signals. First, 3 separate trajectories are analyzed. This is important since, with just a single signal, there is concern that some unsuspected bias may distort the results. By contrast we have 6 signals available for fractal analysis; thus by combining signals in different ways we are able to test the internal consistency of the analyses. Second, since we use several different fractal analysis methodologies, we are able to address the important question of whether different methods of calculating the fractal dimension give comparable results when applied to experimental data. Finally, we also exploit a suggestion by Mandelbrot (1977, 1982), together with an extension of a result of Panchev (1971), to estimate the logarithmic slope of the (displacement) power spectrum in the fractal scaling range from the measured values of the fractal dimension of the drifter trajectories.

The remainder of this paper is organized as follows. Section 2 gives a brief description of the experiment and of the data considered herein. Section 3 summarizes the aspects of fractal behavior for curves on a plane that are pertinent to this study. In particular, we review the notions of scaling exponents, yardstick length and the correlation function as methods for determining the fractal dimension of data. We also discuss how the fractal dimensions can be used to infer the slope of the displacement power spectrum in the case of simple (or "mono") fractals and we introduce the concepts of multifractality and multiple scaling. In Section 4, these methodologies are applied to the data described in Section 2. The statistical uncertainties encountered in this analysis are discussed in Section 5, and some of

the possible physical implications of the results found in the present research are discussed in Section 6.

## 2. Description of data

The data analyzed here consists of the trajectories of 3 drifters deployed in the Kuroshio current off the coast of Japan in 1977. These data were included in the synthesis of the North Pacific subtropical circulation compiled by McNally et al. (1983). Part of the data used here were also analyzed by Vastano et al. (1985) and Kirwan and Cresswell (1982). The classical oceanographic interpretation of these data has thus been well established. Further information on the descriptive and statistical oceanographical aspects of the drifter trajectories can be found in the referenced papers.

The drifters were drogued by parachutes to a depth of 100 m. This large drogue depth was chosen to minimize spurious wind and wave-drift effects on the buoy motions, the trajectories are thought to be representative of fluid particle paths in large scale ocean flows. The problem of closely relating the drifter motions to the real fluid particle trajectories is a difficult and debated issue. In a study of drifter motions in the North Pacific Ocean, for example, McNally (1981) reported the puzzling observation that both drogued and undrogued drifters behaved similarly, both being very sensitive to the local winds. This result was however obtained for drifters with a drogue depth of only about 30 m, and is thus relevant to drifters which measure the dynamics in the surface mixed layer and which are strongly influenced by the local atmospheric (and wave) forcing. Drifters with a much larger drogue depth are by contrast thought to behave differently, following more closely the large and mesoscale flows below the surface mixed layer (Kirwan et al., 1978, 1979; Large and Van Loon, 1989; Krauss et al., 1989). Thus, because of the quite large drogue depth of the drifters studied here, we consider the drifter trajectories to be fairly representative, at sufficiently large scales, of the real fluid parcel trajectories.

The trajectories of the three drifters are shown in Fig. 1. The solid line is for drifter NO106, the dashed line for NO307 and the dash-dotted line is

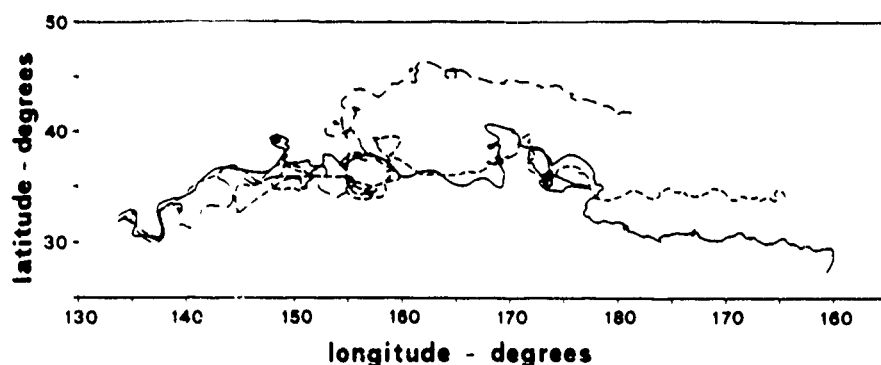


Fig. 1 Lagrangian trajectories of the three satellite tracked drifters in the Kuroshio Extension. The solid line is for buoy NO106, dashed line is for NO307 and dash-dotted line is for NO341.

for drifter NO341. Positions of the drifters were determined several times a day by the Nimbus 6 satellite system. The time series were obtained from the raw Nimbus 6 file by interpolation to equally-spaced time intervals of  $\Delta t = 12$  h. Additional technical details can be found in Kirwan and Cresswell (1982). The paths begin near latitude  $32^\circ$  North and longitude  $133^\circ$  East near the core of the Kuroshio current. In this region, the Kuroshio is a highly organized flow. During the time of deployment the Kuroshio was evidently in its meander mode as suggested by all 3 drifter paths.

East of the Izu Ridge (approximately  $138^\circ$  East), the Kuroshio flow field is much less organized and highly irregular. Large mesoscale variability in this region is well established; see, e.g., Bernstein and White (1979, 1981), Schmitz (1982) and Schmitz et al. (1982) for analyses based on XBT and current meter data. The intense mesoscale variability of this region is related to several possible effects, including the presence of active mesoscale eddies, turbulent dynamics and Rossby waves. This area is thus appropriate to the study of the properties of fluid parcel trajectories in large-scale flows.

The 3 drifters were deployed within 5 km of each other and within an interval of 2 h; they crossed the Izu Ridge within a 7-day period after following paths that deviated by at most 10 km. However, in the Kuroshio extension region their separations in space and time changed dramatically. In the first few days after crossing the ridge the separation between the drifters grew from approximately 10 to more than 500 km. Thereafter the drifters repeatedly approached and sep-

arated in an irregular fashion. It is this extremely irregular and apparently random motion of fluid parcels that is the focus of our study.

### 3. Fractal curves on the plane

In this section we review some of the classical ideas on fractals which are pertinent to this study. The material of this section represents a cursory survey of the techniques which we use in the analysis of the data and is thus limited both in scope and in length. More detailed discussions on fractals and related topics are given in Mandelbrot (1977, 1982). Original developments in the study of the fractal nature of fluid flows may be found for example in Mandelbrot (1972, 1974, 1975), Frisch et al. (1978), Frisch and Morf (1981), and Frisch (1981, 1985) for theoretical aspects and for example in Lovejoy (1982), Lovejoy and Mandelbrot (1985), Sreenivasan and Meneveau (1986), Meneveau and Sreenivasan (1987) and Schertzer and Lovejoy (1987) for experimental results. A recent survey on certain applications of fractals in other fields of physics may be found in Pietronero and Tosatti (1986). For the issues of multifractality, multiple scaling and anisotropy see, e.g., Schertzer and Lovejoy (1983, 1987), Benzi et al. (1984), Frisch and Parisi (1985), Halsey et al. (1986), Lovejoy et al. (1987) and Paladin and Vulpiani (1987).

Heuristically, a fractal is a geometric object whose shape is irregular and/or fragmented at all scales. A technical definition of a fractal is "a set of points whose topological dimension is strictly smaller than its Hausdorff (or fractal) dimen-

sion." The rigorous definition of Hausdorff dimension may be found for example in Mandelbrot (1977, 1982). A striking characteristic of the fractal dimension  $D$  is that it can be non-integer. This is in contrast to the topological dimension which is always integer. A fractal curve on a two dimensional surface (for simplicity a plane) has a fractal dimension which lies somewhere between the topological dimension of the curve (which is  $D_T = 1$ ) and the dimension of the space (here 2). A fractal curve is "non-smooth" at every length scale. No matter how small or large a portion of the curve is examined, one always finds finer or larger scale cusps, structures and "wiggles."

The richness of structures in a fractal curve is related to one of the basic properties of fractals, namely their "scaling" behavior. The scaling properties imply that there is a well-defined relationship describing the structure (e.g., the fluctuations) of the curve at different space and time scales. In the present context, we will be concerned with fractal curves whose scaling properties are statistical and in this case the scaling behavior refers to the probability distribution of the random process which generates the curve. If the curve is parameterized by a single scalar (e.g., time) then each component of the curve is a scaling, random scalar function of this parameter.

A more rigorous definition of scaling is now appropriate. This clarification leads to a basic distinction between monofractals (which are also called "simple" fractals) and multifractals. The issues of multiple scaling and of multifractality are relatively recent and may be associated with multiplicative random processes (see, e.g., Schertzer and Lovejoy, 1987 for a discussion of multifractality and for its applications in geophysics), while monofractals are older and simpler mathematical objects associated with additive random processes (e.g., referred to as "scaling of the increments") and have simple scaling rules. In the following we introduce the relevant ideas of fractal mathematics in the context of monofractals. The extension to multifractal behavior is then considered.

In the case of monofractal curves the scaling properties may be related to the self-affine or self-similar character of the curve or of its parametric representations. To properly define self-affinity consider an arbitrary scalar random function of

time  $X(t)$ . If, for an arbitrary interval  $\Delta t$ ,

$$\lambda^{-H}[X(t + \lambda \Delta t) - X(t)] \stackrel{d}{=} [X(t + \Delta t) - X(t)] \quad (3.1)$$

holds independent of time ( $\stackrel{d}{=}$  means equality in the sense of distributions), then  $X(t)$  is said to be a self-affine simple (or mono) fractal signal with scaling exponent  $H$ . This exponent must be positive and less than or equal to one. Intuitively a self-affine signal is such that if the time scale is multiplied by a factor  $\lambda$  and the signal amplitude by a factor  $\lambda^{-H}$  then the transformed time series has the same statistical properties as the original one. It is important to realize here that self-affinity refers to the properties of the differences in the signal amplitudes. Random, self-affine scalar functions with scaling exponent  $H$  and gaussian increments are the "fractional Brownian functions" discussed by Mandelbrot (1977, 1982). Ordinary Brownian motion is found when  $H = \frac{1}{2}$ . Formula (3.1) also indicates that for monofractal curves a single scaling exponent is sufficient to completely define the scaling properties of the system (e.g., the scaling properties of the mean, of the variance, and of higher moments).

Now consider another random process, say  $Y(t)$ . Being different processes  $X(t)$  and  $Y(t)$  may have different scaling exponents, say  $H_x$  and  $H_y$ . These two time series can be thought of as the parametric equations of a curve which can be viewed as a self-affine random trajectory on the  $X$ - $Y$  plane. This is a particular case of anisotropic monofractal curves, and may be found when different physical conditions are acting in different directions. A well-studied, special case of fractal curves are however self-similar (isotropic) fractal curves; this case occurs when  $X$  and  $Y$  have the same scaling exponent, i.e.,  $H_x = H_y$ . This occurs for example when  $X$  and  $Y$  are different realizations of the same underlying random process. For self-similar monofractals the fractal dimension of the trajectory is given by

$$D = \min[1/H, 2]. \quad (3.2)$$

Hence for  $0 < H < 1$ , the trajectory is a simple fractal curve such that  $1 < D \leq 2$ .

The calculation of the scaling exponent just discussed is a common method for determining the scaling properties and for obtaining the fractal dimension of a self-similar monofractal



curve. Another method for obtaining the fractal dimension is based on measuring the length of the curve by varying-length rulers (see Mandelbrot, 1967, 1977, 1982). If the length is approximated by a broken line whose segments have a "yardstick" length  $\Delta$  then, in the limit for small  $\Delta$ , the length goes as

$$L(\Delta) \approx \Delta^{1-D_L}, \quad (3.3)$$

where  $D_L$  is the "divider dimension" which approximates the Hausdorff dimension  $D$ . For an analytic function,  $D_L = 1$  and one obtains the ordinary length of a differentiable curve. For fractal curves the length diverges for smaller and smaller yardstick lengths. Computing the power law in (3.3) for the length divergence of a self-similar monofractal curve furnishes its fractal dimension.

A third method for determining the dimension of a fractal curve is based on the computation of the correlation dimension of the curve through a method proposed by Grassberger and Procaccia (1983). To compute the correlation dimension (which is an approximation to the Hausdorff dimension) from a digitized, vector time series  $x(t_i)$  one first calculates the Grassberger and Procaccia correlation function

$$C(\epsilon) = \frac{1}{M^2 - M} \sum_{i,j} \Theta(\epsilon - \|x(t_i) - x(t_j)\|), \quad (3.4)$$

where  $\Theta$  is the Heavyside step function,  $M$  is the number of points in the time series and the vertical bars indicate the norm of the vector. In the case of a self-similar fractal curve one has for small  $\epsilon$ ,

$$C(\epsilon) \approx \epsilon^v, \quad (3.5)$$

where  $v$  is the correlation dimension of the curve. Typically the correlation dimension is computed by calculating the slope of the correlation function (for small  $\epsilon$ ) in log-log coordinates.

An important observation is that the fractal dimension can be related to concepts from classical time series analysis. Specifically, there is a close relationship between self-affine, monofractal signals  $X(t)$  and their power spectra. Self-affinity implies that there is no preferred length scale in the signal. By a straightforward extension of the classic argument which relates the structure function of a signal to its power spectrum

(see Panchev, 1971), one finds that a self-affine signal with scaling exponent  $H$  has a power law spectrum  $P(\omega) \approx \omega^{-2}$  (where  $\omega$  is the angular frequency) such that

$$\alpha = 2H + 1, \quad 1 < \alpha \leq 3. \quad (3.6)$$

It is possible to extend this result to the case of a curve in an  $N$ -dimensional space, where one finds that, for self-similar monofractal curves, the spectral slopes of the signal components can be related to the fractal dimension of the curve through (3.2) and (3.6), such that

$$D = \min[2/(\alpha - 1), N]. \quad (3.7)$$

It is important to stress that the relation between the scaling nature of a signal and the power-law dependence of its power spectrum is unidirectional, i.e., the self-affine, fractal character of a signal determines the power law form of the spectrum, and not vice versa. Only in particular cases, in which both the power spectrum and the phase spectrum have particular characteristics, then relation (3.6) is valid in both "directions". An example of this is provided by random systems with power-law spectra and random Fourier phases uniformly distributed on  $(0, 2\pi)$  (see, e.g., Osborne and Provenzale, 1989). In this particular case, the slope of the power spectrum and the fact that the phases are random univoquely fixes the self-affine properties of the signal. In general, however, the sole knowledge of power-law dependence in a power spectrum does not infer that the corresponding signal is fractal. In fact (a) perfect power-law spectra are almost never observed in experimental results and one does not know a priori how sensitive the fractal properties are to deviations from power-law behavior, and (b) simple examples exist of signals which have power law spectra but which are non-fractal. The common triangular wave has a power law spectrum  $P(\omega) \approx \omega^{-2}$  but it is obviously non-fractal. Thus, when an  $\omega^{-2}$  spectrum is for example observed, it is not possible to know a priori whether the corresponding signal is self-affine (and fractal) or if it is dominated by few strong "jumps" (and is non-fractal). The fractal nature of a signal must thus be assessed independently from the power-law form of the spectrum. The latter may be taken at most as an indication of the possible presence of fractal behavior.

For simple, self-similar fractal curves the different methods for computing the fractal dimension provide (within the statistical uncertainties associated with the experimental errors and the finite amount of data) the same value for the fractal dimension. This relationship does not hold if the curve under study has a multifractal nature. In this case the parametric representation of the curve does not obey a simple relationship such as eq. (3.1), and the correspondence between the value of the dimension and the logarithmic slope of the power spectra is not necessarily given by eq. (3.7). The different methods for computing the fractal dimension, which rely upon different assumptions and measure different scaling properties of the curve, may thus provide different values for the fractal dimension. This results from the fact that for data with multifractal properties there are infinitely many different fractal dimensions. These are related to the different moments of the probability distributions of the process under study.

Multifractal properties are in fact related to multiplicative random processes and are associated with different scaling properties at different scales. In this case, a single scaling exponent (and a single fractal dimension) are not sufficient to describe the behavior of the statistical moments at different scales (see, e.g., Schertzer and Lovejoy, 1987 and Paladin and Vulpiani, 1987). Thus the extension from the simple scaling properties of monofractals to the more complex situation found for multifractals allows for a wider application of the "fractal approach" and also allows for a closer link to the dynamical processes active in fluid flows.

A simple way to study multifractal behavior is based on the use of a box-counting algorithm. Given a fractal curve on a two dimensional surface (for simplicity a plane) the box-counting procedure is based on filling the plane with a covering of adjacent square boxes of size  $\epsilon$ , and on computing the probability  $p_i(\epsilon)$  that the  $i$ th box contains a piece of the fractal curve. For fractal curves one has that for small  $\epsilon$

$$\sum_i [p_i(\epsilon)]^q \approx \epsilon^{(q-1)D_q}, \quad (3.8)$$

where the sum is extended over all non-empty boxes. The quantities  $D_q$  are the generalized fractal dimensions; a fundamental difference

between monofractals and multifractals is that for monofractal curves one has that  $D_q = D_q$  for  $q \neq q'$  while for multifractals the different generalized dimensions are not equal. In general in fact  $D_q < D_{q'}$  for  $q > q'$ . The usual correlation dimension is for example recovered for  $q = 2$ . Thus computing at least some of the generalized dimensions  $D_q$  provides a way to test the multifractal nature of a signal.

A word of caution about the application of multifractal methods is perhaps necessary however. The interest herein is focused on the application of these ideas to experimental data. A realistic application of multifractal methods to natural data provides information only on moments of lowest order. It is well-known that the errors of the higher moments may be large because of experimental noise and the finite length of a time series. Another question relates to the origin of (possibly observed) differences among the various generalized dimensions, since it may be unclear whether these deviations are produced by statistical fluctuations or by genuine multifractal behavior. These points will be discussed further below in the analysis of the Kuroshio data.

It is worth stressing that in all physical applications the focus is on "natural" fractals, as opposed to mathematical fractals. The latter "scale" over *all* length scales and their length truly diverges, while the former scale only in a well defined range of scales. For natural fractals small scale processes such as molecular diffusion and experimental noise limit the scaling range for small distances. In fluid dynamics an additional constraint to scaling is provided by the particle paths being solutions to a system of partial differential equations and hence continuously differentiable at very small scales. At large scale constraints such as the finite time of the experimental measurement, or natural boundaries such as the size of the ocean, provide an upper limit to scaling. For natural fractals the various fractal analysis methods therefore provide the value of the fractal dimension and also indicate the scale range over which fractal properties hold. In particular the scaling exponent calculations provide time scale information while the yardstick length and correlation function methods give space scales. Employing the various methods, one can thus gain independent space and time

scale information about the extent of the fractal scaling range. In the authors' opinion the information on the extent of the scaling range is probably almost as important as the discovery of the scaling behavior itself.

#### 4. Fractal analysis of the Kuroshio data

In this section, the ideas discussed above are applied to the analysis of the drifter trajectories from the Kuroshio extension. The first test is to compute the scaling exponents  $H_x$  and  $H_y$  of the longitude ( $x$ ) and latitude ( $y$ ) positions of the drifters. This test is important because it determines whether the signals display (statistical) scaling properties. As discussed above this method also provides time-scale information.

To compute the scaling exponents attention is focused on the average absolute value of displacements in longitude ( $\Delta x$ ) and latitude ( $\Delta y$ ), which for self-affine signals must obey

$$\begin{aligned} \overline{|x(t + \lambda \Delta t) - x(t)|} &= \overline{\Delta x(\lambda \Delta t)} = \lambda^{H_x} \overline{\Delta x(\Delta t)} \\ &= \lambda^{H_x} \overline{|x(t + \Delta t) - x(t)|}, \end{aligned} \quad (4.1)$$

$$\begin{aligned} \overline{|y(t + \lambda \Delta t) - y(t)|} &= \overline{\Delta y(\lambda \Delta t)} = \lambda^{H_y} \overline{\Delta y(\Delta t)} \\ &= \lambda^{H_y} \overline{|y(t + \Delta t) - y(t)|}. \end{aligned} \quad (4.2)$$

In (4.1) and (4.2), the vertical bars indicate absolute value and the overbar indicates a time

average. The delay time  $\lambda \Delta t$  is an integer multiple of the sampling time  $\Delta t = 12$  hours. If the signals are self-affine then graphs of  $\overline{\Delta x(\lambda \Delta t)}$  and  $\overline{\Delta y(\lambda \Delta t)}$  versus  $\lambda$  must fall on a straight line on a log-log plot, the slope of this line being the value of the scaling exponent.

Figs. 2 and 3 show  $\overline{\Delta x(\lambda \Delta t)}$  and  $\overline{\Delta y(\lambda \Delta t)}$  versus  $\lambda$  in log-log coordinates for each of the drifters. The mean (eastward and northward) drifter velocity has been removed from each time series used here. This step is standard in the study of turbulent flows and in our case it is useful in that it compacts the longitude signals that would otherwise be stretched in the east-west direction by the zonal flow. This implies that we are studying the properties of fluid particle motions around the rectilinear trajectory generated by a constant mean flow. This is also equivalent to a Galilean transformation to a coordinate system moving with the constant mean flow. These aspects are discussed further in Section 5.

From Figs. 2 and 3 scaling is evident both for longitude and latitude for all three drifters. A lower limit to the scaling range is fixed by the deviation of the curve from a straight line to be approximately 1.5 days. An upper limit to scaling is approximately 8 days for longitude and 6.5 days for the latitude time series. Table 1 lists the values of the scaling exponents obtained from a least-square-fit over the scaling range. The indicated uncertainties on the individual values of  $H_x$

Table 1. Values of the scaling exponent and of the fractal dimension obtained by the various methods from the three trajectories

Drifter	Component	$H$	$D = 1/H$	$D_L$	$v$
NO106	longitude	$0.85 \pm 0.02$	$1.27 \pm 0.09$	$1.20 \pm 0.03$	$1.35 \pm 0.05$
	latitude	$0.73 \pm 0.02$			
	average	$0.79 \pm 0.06$			
NO307	longitude	$0.85 \pm 0.02$	$1.19 \pm 0.02$	$1.14 \pm 0.02$	$1.28 \pm 0.08$
	latitude	$0.84 \pm 0.02$			
	average	$0.84 \pm 0.02$			
NO341	longitude	$0.75 \pm 0.02$	$1.34 \pm 0.04$	$1.35 \pm 0.05$	$1.33 \pm 0.04$
	latitude	$0.75 \pm 0.02$			
	average	$0.75 \pm 0.02$			
ensemble average	longitude	$0.81 \pm 0.03$	$1.26 \pm 0.05$	$1.23 \pm 0.06$	$1.32 \pm 0.06$
	latitude	$0.77 \pm 0.03$			
	average	$0.79 \pm 0.03$			

The uncertainties on the individual values are the least-square-fit statistical bounds, while the uncertainties on the average values are the maximum between the error due to propagation of individual errors and the standard deviation of the average.

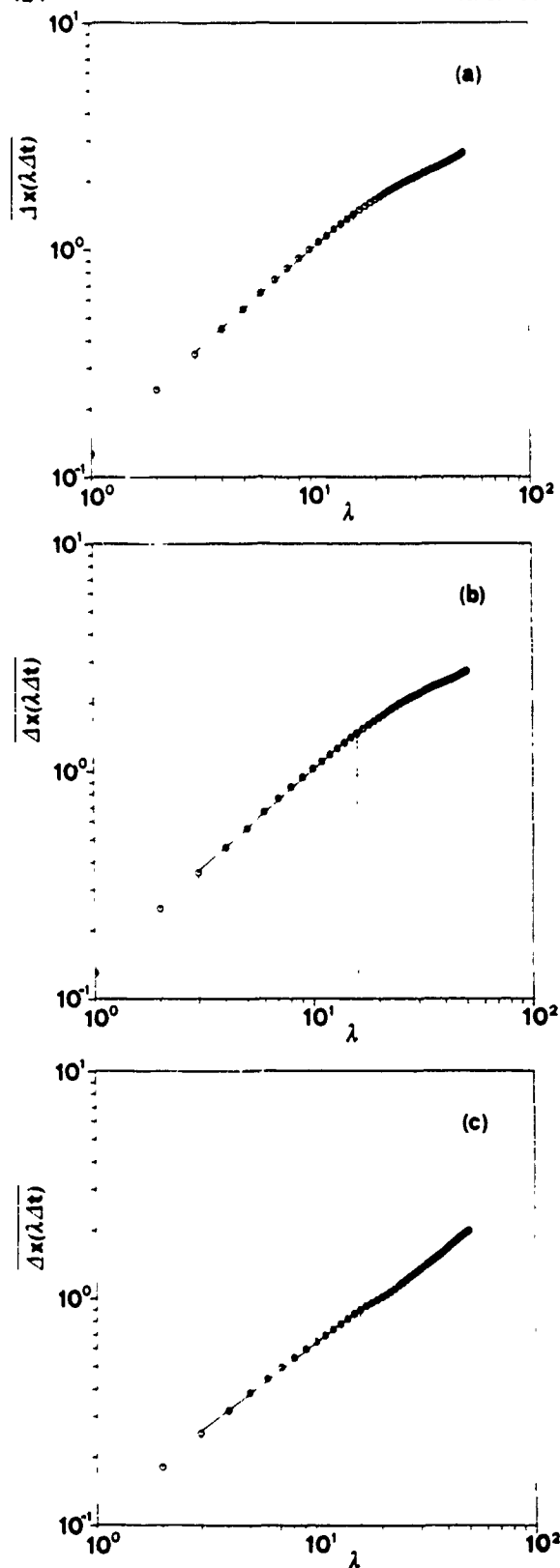


Fig. 2. Plot of  $\overline{\Delta x(\lambda \Delta t)}$  versus  $\lambda$  in log-log coordinates for the three drifter trajectories. Panel (a) is relative to drifter NO106, panel (b) refers to drifter NO307 and panel (c) to drifter NO341. The two vertical dashed lines indicate the limits of the scaling range. The solid

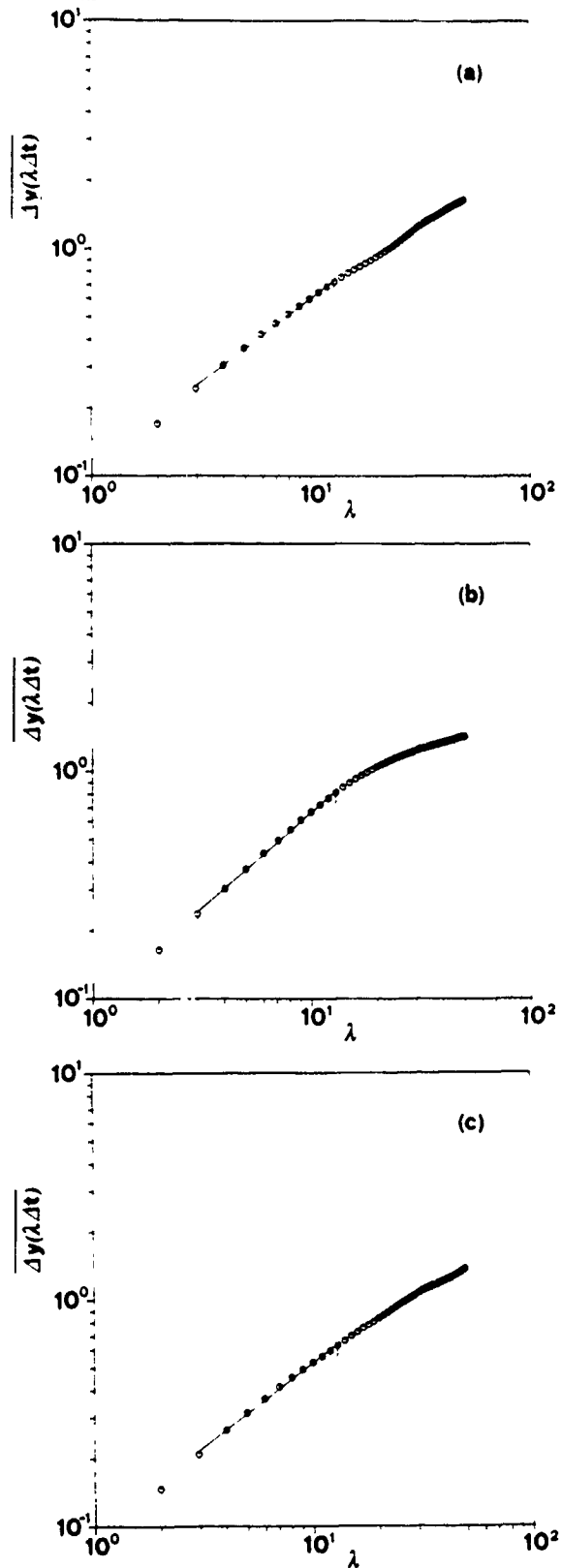


Fig. 3. Plot of  $\overline{\Delta y(\lambda \Delta t)}$  versus  $\lambda$  in log-log coordinates for the three drifter trajectories. Same details as in Fig. 2.

line in each panel is the least-square fit to the data. The slope of this line gives the scaling exponent.

and  $H_i$  are the statistical errors of the least square fits to the slopes of  $\overline{\Delta x(\lambda \Delta t)}$  and  $\overline{\Delta y(\lambda \Delta t)}$ . These have been obtained as the least-squares 95% confidence limits on the individual values of the slope. It should be recognized that these are just the statistical uncertainties on the power law dependence of  $\overline{\Delta x(\lambda \Delta t)}$  and  $\overline{\Delta y(\lambda \Delta t)}$ , they do not account for bias in the calculations arising from the fact that the time series have finite length, for propagation of experimental errors or, even more importantly, for the statistical fluctuations inherent in the value of the scaling exponent from one signal (and hence one realization) to another. This latter point is discussed further in Section 5. We remark here that when an average over several individual values of the scaling exponent (or of the dimension) is taken, the indicated uncertainty is the maximum between the standard deviation of the average and the uncertainty due to propagation of individual least-square errors. The latter is in general observed to be much smaller than the former.

Averaging the longitude and latitude scaling exponents for each drifter and using eq. (3.2) gives estimates of the fractal dimension of each of the three trajectories. These are also reported in Table 1. The average over all drifters then furnishes a value  $D = 1.26 \pm 0.05$  for the average fractal dimension. This result is evidently the first indication that fluid parcel trajectories in a large scale ocean flow may exhibit fractal and scaling behavior.

The average over  $H_i$  and  $H_j$  for each trajectory and the use of eq. (3.2) implies an isotropic character for the buoy trajectories. This seems justified since the difference between the average longitudinal and latitudinal values of the scaling exponent is quite small, indicating that any deviations from isotropic behavior are probably very mild. We thus consider the drifter trajectories, at least in a first approximation, to be isotropic fractal curves. We note however that the effects of rotation induce well-known differences between the meridional and the zonal directions, which could in turn induce different scaling properties in the two directions and consequently result in anisotropic behavior (which could for example be studied by methods such as "functional box counting", see, e.g., Lovejoy et al. (1987), and Schertzer and Lovejoy (1987)). A deeper understanding of the isotropic or anisotropic nature of drifter trajectories in large scale flows is thus an

important issue, but definite conclusions must be deferred to future studies with larger data bases than those considered here.

As a second step in the study of the fractal properties of these data we now compute the lengths of the three drifter trajectories in the  $x$ - $y$  plane by a variation of the yardstick method discussed earlier in Section 3. The strict version of this method cannot be applied here since the data are equally spaced in time but not in space. This means that one cannot choose a fixed yardstick length. The simplest solution to this problem is to compute the trajectory length  $L(\Delta_{iv})$  versus the average length  $\Delta_{iv}$  of the yardstick. A separate analysis shows that the errors introduced by a non-constant yardstick length are, in the present case, on the order of the statistical uncertainties of the least-square fit to the slope in the scaling region. Thus the slope of  $L(\Delta_{iv})$ , for small  $\Delta_{iv}$ , gives the fractal dimension of the curve with inconsequential error.

Fig. 4 shows the results for the three drifter trajectories. The path lengths clearly diverge for small  $\Delta_{iv}$ . In this region all curves exhibit power-law behavior with  $L(\Delta_{iv}) \sim \Delta_{iv}^{1-D_L}$ . The values of  $D_L$  are listed in Table 1. These results give as an average fractal dimension  $D_L = 1.23 \pm 0.06$  for the three trajectories. Of course with these data (as with all experimental time series) the length divergence does not continue up to infinitesimal yardstick lengths. The length divergence follows a well-defined power law down to scales of roughly 20 km, indicating fractal and scaling behavior down to these spatial scales. An upper limit to scaling may in turn be fixed at approximately 100 km.

The last test which we use for determining the value of the fractal dimension (and for estimating the extent of the scaling range) is obtained from the Grassberger and Procaccia correlation function. Fig. 5 shows the 3 correlation functions for the drifter paths. The mean drifter velocity was removed from the data before calculation of the correlation function. Scaling is evident from spatial scales of approximately 20 km up to scales of roughly 150 km. The slopes of the three correlation curves (in log-log coordinates) in the scaling range and the individual least-square-fit errors are given in Table 1. From these values the average correlation dimension of the three drifter trajectories is calculated to be  $\nu = 1.32 \pm 0.06$ .

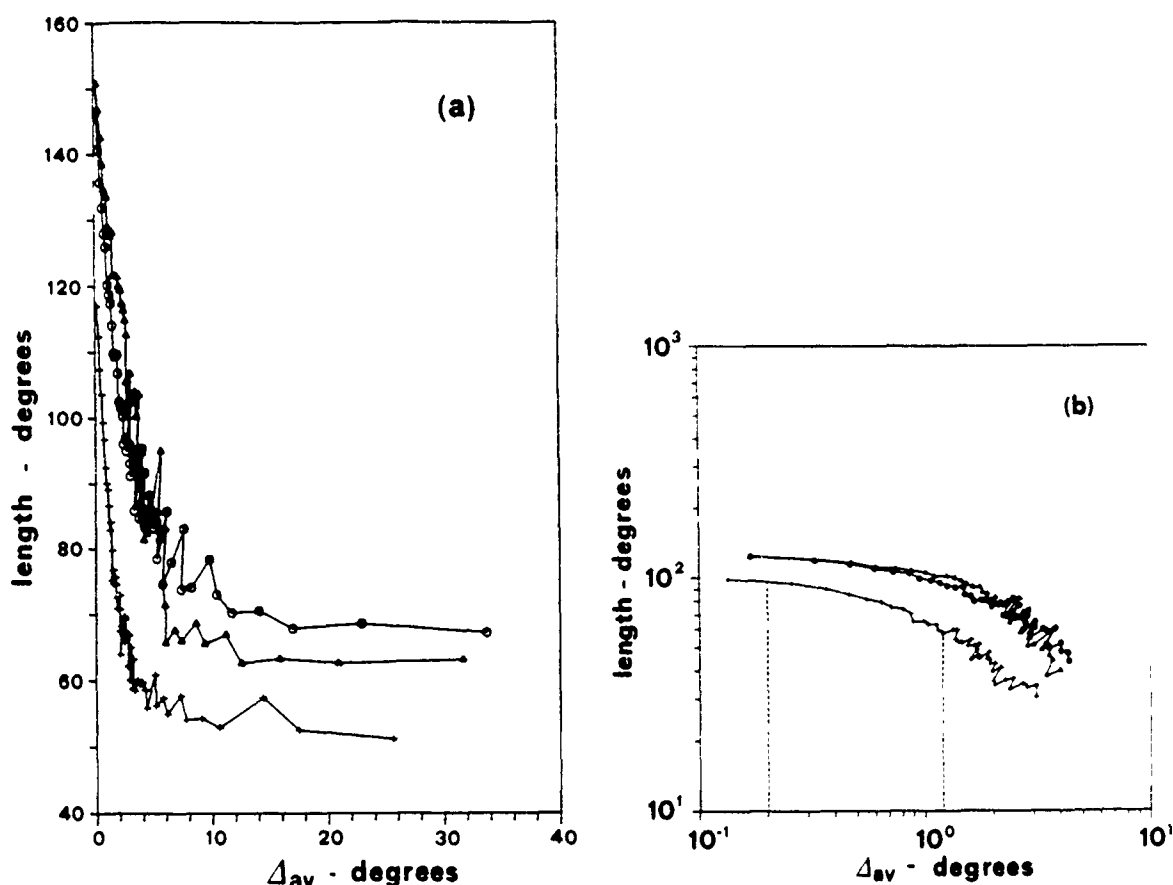


Fig. 4 Length  $L(\Delta_{av})$  of the three trajectories versus the average yardstick length in linear coordinates (panel (a)) and log-log coordinates (panel (b)). Circles are for buoy NO106, triangles for NO307 and crosses for NO341. Note the divergence of the lengths for small  $\Delta_{av}$ .

We have therefore used three independent methods for finding the value of the fractal dimension and the extent of the scaling range. Since the 3 methods rely upon different assumptions, and because they measure different properties of the trajectories, the likelihood is lessened that systematic factors associated with a particular technique have affected the results of the analysis. All 3 methods show that the drifter trajectories display fractal properties and scaling in a well-defined range of scales. Estimates of the average fractal dimension are between 1.23 and 1.32. The differences among the results of the various methods, as well as the differences among the estimates obtained from different drifter trajectories, are discussed in Section 5.

Previously it was noted that the fractal dimension of a self-affine monofractal signal is related to the logarithmic slope of its power-law spec-

trum. This is due to the fact that the scaling nature of a signal originates a power spectrum with power-law behavior. Power spectral analysis of the drifter positions is shown in Fig. 6 for the longitude and in Fig. 7 for the latitude time series. Even if not perfectly power-law as would be found for "mathematical" fractals, the spectra of the drifter positions clearly display an overall power-law dependence. The spectra displayed here have been passed through a Hanning filter. The spectra have been fitted to power laws by the least-squares method over the range 0.04–1.0 rad/day. We note that in analyses like those considered here, considerable care must be exercised in computing the slopes of the power spectra. Procedures such as the Hanning filter may in fact lead to biased estimates of the spectral slope. For this reason the slope estimates reported here were obtained from the unfiltered

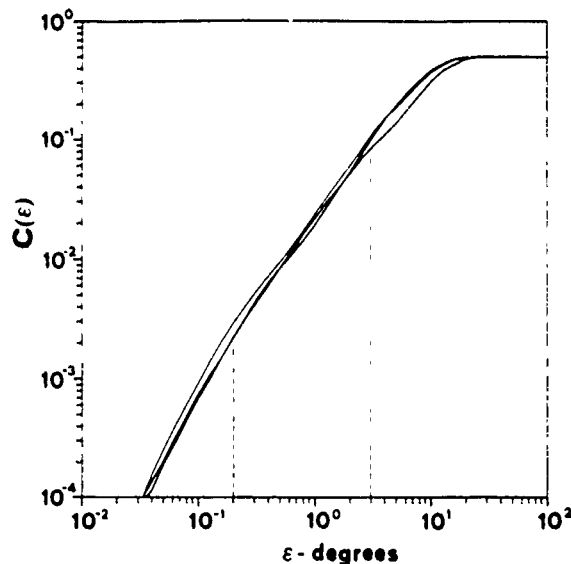


Fig 5. Correlation functions for the three drifter trajectories. The slope of the correlation function in log-log coordinates is a measure of the correlation dimension of the signal. The two vertical dashed lines indicate the approximate limits of the scaling range.

spectra. The resultant slopes are given in Table 2 where the uncertainties are the 95% confidence limits of the least-square slope estimates. We also provide estimates of spectral slopes derived from the values of the scaling exponents and the fractal dimension (through eqs. (3.6) and (3.7)); these are also given in Table 2. Note that these latter are

all within the 95% confidence limits of the observed slopes. This relation between the self-affine character of the signals and the power-law dependence of their spectra was in fact expected on the basis of the discussion given in Section 3, and may be considered as a further confirmation of the scaling nature of these data.

Given that the scaling and fractal nature of drifter trajectories in large-scale ocean flows has been determined, an interesting question is now whether they also display a monofractal or a multifractal behavior. To this end we have applied a box-counting algorithm to the detrended drifter data in order to determine the generalized dimensions  $D_q$  for several values of  $q$ . From an experimental point of view, the probability  $p_i(\epsilon)$  that the  $i$ th box with size  $\epsilon$  be occupied is now empirically computed from a measured series of points by

$$p_i(\epsilon) = n_i(\epsilon)/N, \quad (4.3)$$

where  $n_i(\epsilon)$  is the number of data points falling in the  $i$ th box and  $N$  is the total number of points in the time series.

For determining the possible multifractal behavior of the drifter data, we have computed the function  $\sum_i [p_i(\epsilon)]^q$  for several values of  $q$  between 1.5 and 6.5 for each of the trajectories. Power-law behavior for all three trajectories and for all the selected values of  $q$  is evident in the functions

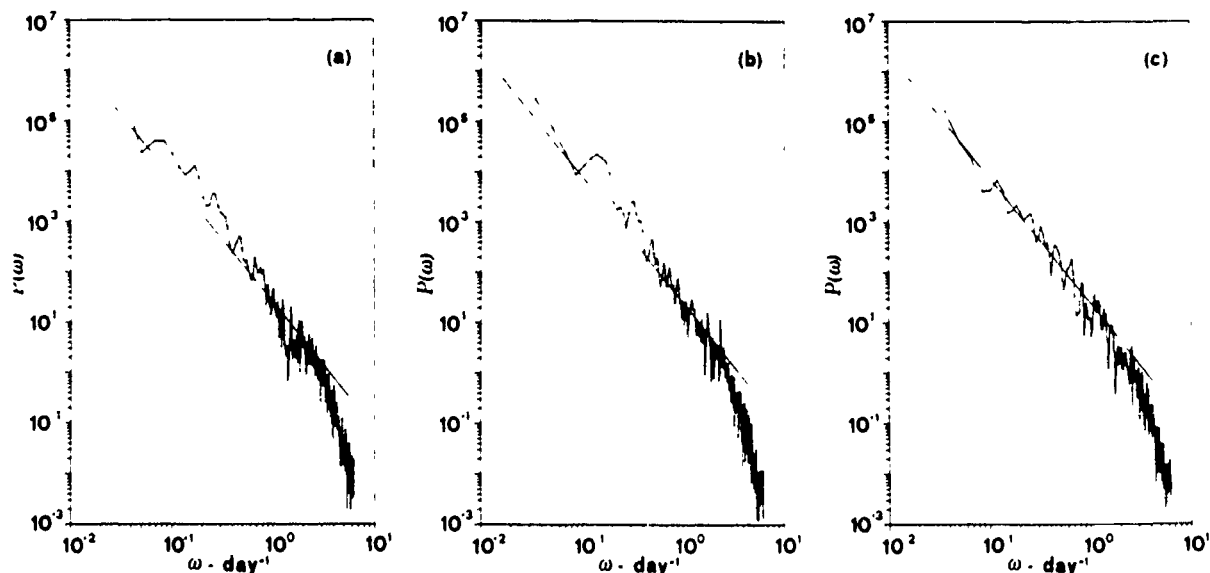


Fig 6. Power spectra of longitude signals for the three drifter trajectories. Panel (a) refers to drifter NO106, panel (b) to drifter NO307 and panel (c) to drifter NO341. The solid line represents an  $\omega^{-2.5}$  power spectrum.

Table 2. Values of the spectral slopes measured from the drifter spectra through least-square fits and of the spectral slopes derived from the self-affine character of the signal

Drifter	Component	$\alpha$	From $H$	From $D_L$	From $v$
NO106	longitude	$2.75 \pm 0.37$	$2.69 \pm 0.03$		
	latitude	$2.11 \pm 0.42$	$2.46 \pm 0.05$		
	average	$2.43 \pm 0.40$	$2.58 \pm 0.12$	$2.67 \pm 0.04$	$2.48 \pm 0.06$
NO307	longitude	$2.78 \pm 0.37$	$2.69 \pm 0.03$		
	latitude	$2.49 \pm 0.37$	$2.68 \pm 0.04$		
	average	$2.64 \pm 0.37$	$2.69 \pm 0.04$	$2.75 \pm 0.04$	$2.56 \pm 0.10$
NO341	longitude	$2.56 \pm 0.34$	$2.49 \pm 0.03$		
	latitude	$2.23 \pm 0.39$	$2.49 \pm 0.05$		
	average	$2.40 \pm 0.37$	$2.49 \pm 0.04$	$2.48 \pm 0.05$	$2.51 \pm 0.05$
ensemble average	longitude	$2.70 \pm 0.36$	$2.63 \pm 0.07$		
	latitude	$2.28 \pm 0.39$	$2.54 \pm 0.07$		
	average	$2.49 \pm 0.38$	$2.59 \pm 0.07$	$2.63 \pm 0.07$	$2.51 \pm 0.07$

The indicated uncertainties on the observed spectra are the least-square-fit statistical bounds while those on the computed slopes are due to propagation of the errors of the scaling exponent and of the fractal dimension.

$\sum_i [p_i(\varepsilon)]^q$  at least for  $\varepsilon$  in the interval from approximately 20 to more than 100 km (in agreement with the results of the methods discussed above) and the generalized dimensions are reported in Table 3. Fig. 8 reports the generalized dimension  $D_q$  versus  $q-1$  for the drifter NO106 (panel a), for NO307 (panel b) and for NO341 (panel c).

We recall that for monofractals, the generalized dimensions  $D_q$  are all equal. From Fig. 8 we see however that there is a well-defined decrease

of the  $D_q$  for increasing  $q$ , a common result in the case of multifractal curves. Note that the three different trajectories provide quite consistent estimates of the generalized dimensions. Note also however that the average  $D_q$  varies only from  $D_{1.5} \approx 1.4$  to  $D_{6.5} \approx 1.2$ , i.e., less than 20%. While obviously constrained to lie in the range  $1 \leq D_q \leq 2$ , one would have expected a larger variation for "strong" multifractal behavior. We thus conclude that the drifter trajectories probably possess a genuine multifractal

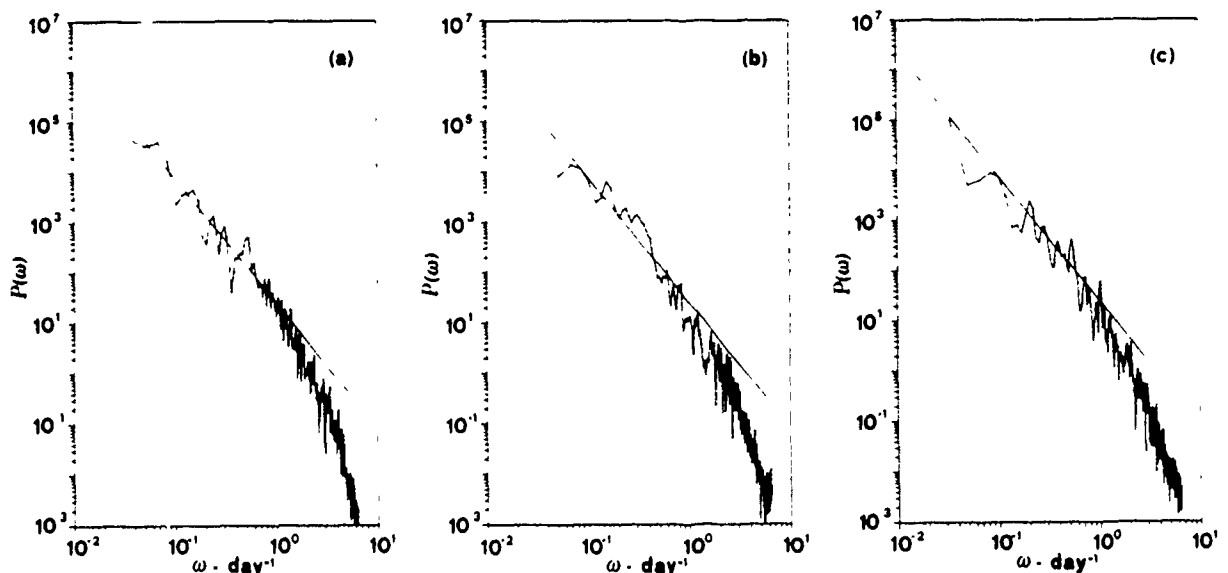


Fig. 7 Power spectra of latitude signals for the three drifter trajectories. Same details as Fig. 6.



Table 3. Values of the generalized fractal dimensions obtained by a box counting method from the three trajectories

$q-1$	Generalized dimension $D_q$		
	NO106	NO307	NO341
0.50	$1.38 \pm 0.02$	$1.44 \pm 0.03$	$1.37 \pm 0.03$
0.75	$1.36 \pm 0.02$	$1.42 \pm 0.03$	$1.35 \pm 0.03$
1.00	$1.34 \pm 0.02$	$1.40 \pm 0.03$	$1.33 \pm 0.03$
1.25	$1.32 \pm 0.02$	$1.38 \pm 0.04$	$1.32 \pm 0.03$
1.50	$1.30 \pm 0.02$	$1.36 \pm 0.04$	$1.30 \pm 0.03$
1.75	$1.28 \pm 0.02$	$1.34 \pm 0.04$	$1.28 \pm 0.03$
2.00	$1.27 \pm 0.02$	$1.32 \pm 0.05$	$1.27 \pm 0.03$
2.25	$1.26 \pm 0.02$	$1.31 \pm 0.05$	$1.26 \pm 0.03$
2.50	$1.24 \pm 0.02$	$1.29 \pm 0.05$	$1.25 \pm 0.04$
2.75	$1.23 \pm 0.02$	$1.28 \pm 0.06$	$1.23 \pm 0.04$
3.00	$1.22 \pm 0.02$	$1.26 \pm 0.06$	$1.22 \pm 0.04$
3.25	$1.21 \pm 0.02$	$1.25 \pm 0.06$	$1.21 \pm 0.04$
3.50	$1.20 \pm 0.03$	$1.24 \pm 0.06$	$1.20 \pm 0.04$
3.75	$1.20 \pm 0.03$	$1.23 \pm 0.07$	$1.20 \pm 0.04$
4.00	$1.19 \pm 0.03$	$1.22 \pm 0.07$	$1.19 \pm 0.04$
4.25	$1.18 \pm 0.03$	$1.21 \pm 0.07$	$1.18 \pm 0.04$
4.50	$1.18 \pm 0.03$	$1.20 \pm 0.07$	$1.18 \pm 0.05$
4.75	$1.17 \pm 0.03$	$1.19 \pm 0.07$	$1.17 \pm 0.05$
5.00	$1.16 \pm 0.03$	$1.19 \pm 0.07$	$1.16 \pm 0.05$
5.25	$1.16 \pm 0.03$	$1.18 \pm 0.08$	$1.16 \pm 0.05$
5.50	$1.15 \pm 0.03$	$1.17 \pm 0.08$	$1.15 \pm 0.05$

The uncertainties on the individual values are the least-square-fit statistical bounds.

behavior, which is however quite "mild". This also implies that, while multiplicative random processes are probably required for a deeper understanding of the dynamics, a simple first-order model based on additive processes (e.g., fractional Brownian motion) probably describes some of the principal features of the drifter motions.

### 5. Discussion of uncertainties in the analysis of the data

Table 1 summarizes our analysis on the monofractal properties of the three drifter trajectories. These results indicate that near-surface fluid particle paths from the Kuroshio extension region exhibit fractal behavior with an average fractal dimension of  $1.27 \pm 0.06$  for spatial scales from approximately 20 to 150 km and time scales from approximately 1.5 days to 1 week. This

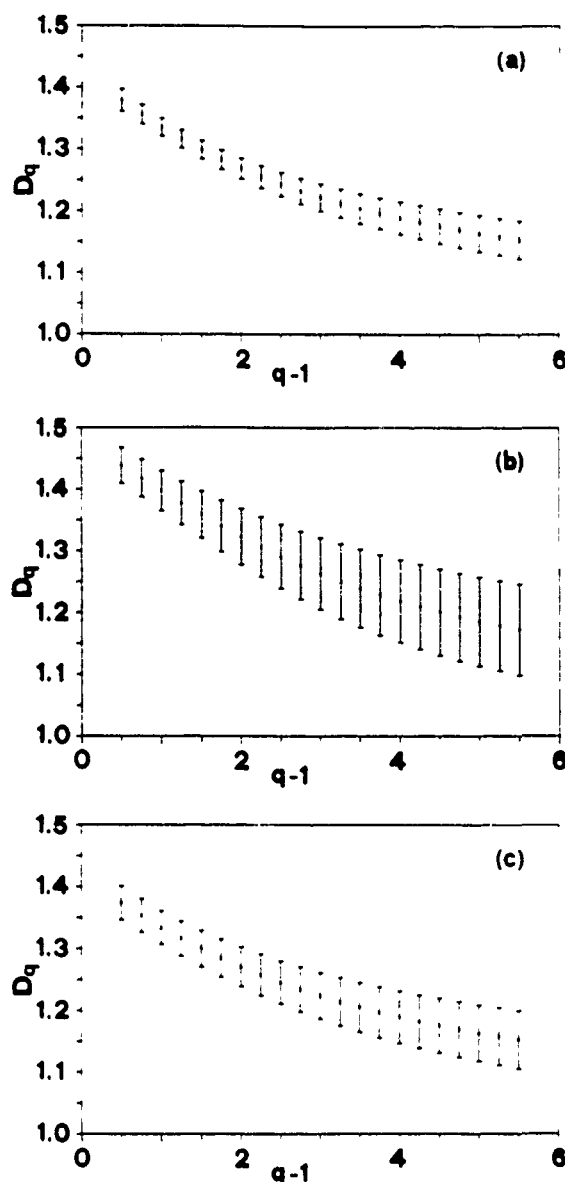


Fig. 8. Generalized dimensions  $D_q$  versus  $q-1$ . Panel (a) refers to drifter NO106, panel (b) to drifter NO307 and panel (c) to drifter NO341.

value of the fractal dimension has been obtained by averaging the dimension estimates from three independent methods and the indicated uncertainty is the standard deviation of the average. Statistical bounds on the value of the average fractal dimension of the drifter paths may be fixed by the use of a standard two-tailed student- $t$  distribution. Averaging the dimension estimates from the three different methods and the three trajectories one obtains  $D = 1.27 \pm 0.11$  with a 95% confidence limit. It is important to stress

that the 95% confidence limits outlined above indicate that the average fractal dimension is significantly larger than one. This is important since it provides strong evidence for the fractal character of the drifter trajectories.

The individual values of the fractal dimension and of the scaling exponent have been determined by fixing a scale range over which an appropriate quantity ( $\overline{\Delta x(\lambda \Delta r)}$ ,  $\overline{\Delta y(\lambda \Delta r)}$ ,  $L(\Delta_{\nu})$ ,  $C(\epsilon)$ ) shows a power-law dependence on its argument. The choice of the scaling range is, of course, somewhat subjective. We observe however that if we decrease the range of scales over which the least-square fit to the data has been obtained, no significant changes in the values of the scaling exponent are observed. If, on the contrary, we perform a least-square fit in a range larger than that selected in the analysis, then significant changes in the values of the scaling exponent and much larger errors on the least-square fits are soon observed. Thus in general the idea that guides the search for the extension of the scaling range is to define the maximum range inside which no significant deviations from power law dependence are detected. The smallness of the statistical errors on the least-square fits to the slopes (which in the present case never exceeds 4% of the value of the scaling exponent) in particular provides a strong indication that  $\overline{\Delta x(\lambda \Delta r)}$  and  $\overline{\Delta y(\lambda \Delta r)}$  obey a power law and thus that the scaling nature of these signals is well defined.

Another important issue in the analysis is whether the differences among the fractal dimension estimates provided by the various methods and by the different trajectories are significant. From Table 1, it is seen that of the three methods used to compute the fractal dimension, the "yardstick length" ( $D_L$ ) method gives results with the largest scatter. The most internally consistent technique for obtaining the fractal dimension for this data set has been found to be the correlation dimension ( $\nu$ ) method. The use of individual least-square errors is however inappropriate to decide whether the deviations among the various measured values of the fractal dimension may have some significance, as these errors only indicate the correctness of a power-law fit to each individual signal and do not take into account experimental errors, biases arising from the relatively limited number of data points and

Table 4. Values of the scaling exponent obtained from fifteen different realizations of a self-affine random signal with 733 points

Realization number	Scaling exponent
1	$0.777 \pm 0.005$
2	$0.816 \pm 0.003$
3	$0.682 \pm 0.010$
4	$0.779 \pm 0.002$
5	$0.851 \pm 0.004$
6	$0.797 \pm 0.005$
7	$0.756 \pm 0.003$
8	$0.704 \pm 0.006$
9	$0.764 \pm 0.004$
10	$0.796 \pm 0.003$
11	$0.787 \pm 0.006$
12	$0.789 \pm 0.004$
13	$0.787 \pm 0.002$
14	$0.772 \pm 0.008$
15	$0.659 \pm 0.016$

The uncertainties on each value of  $H$  are the least-square fit statistical bounds. It is clear how the value of  $H$  displays statistical fluctuations from one realization to another which are not accounted for by the least-square fit statistical bounds.

statistical fluctuations of the measured dimension from one signal to another. Hence the errors of the least-square fits to the slopes, while being important indicators of the well-defined scaling properties of the signals, are too small to be considered as representative of the real statistical fluctuations in the value of the scaling exponent from one signal (i.e., one statistical realization) to another. To emphasize this observation, we report in Table 4 the values of the scaling exponent computed from fifteen realizations of a synthetic, self-affine random process (with 733 data points) obtained by inverting a power-law power spectrum  $P(\omega) \approx \omega^{-2.7}$  with random Fourier phases uniformly distributed on  $(0, 2\pi)$ . As discussed above, for this particular class of random processes there is a one-to-one correspondence between the slope of the power spectrum and the value of the scaling exponent. Each realization of this process corresponds to the same power spectrum but to a different set of random phases. From Table 4, one sees that the values of the scaling exponent obtained from the various realizations are well outside the respective least-square confidence limits, thus indicating

that these must be considered at most as lower limits to the real statistical fluctuations of the system. A similar behavior is therefore to be expected in general when the scaling exponent (or the fractal dimension) is measured from experimental data, even if arising from a strict deterministic origin, as the measurement process itself would generate fluctuations in the values of these quantities.

To study the significance of the deviations observed among the various measured values of the fractal dimension one may thus more appropriately use a standard two-tailed, student-*t* distribution for determining the confidence limits of each group of measurements and for testing their consistency. Averaging the dimension estimates obtained by the three different methods for each of the trajectories, or alternatively averaging over the trajectories to keep distinct the outputs of the various methods, we find that the various estimates for the fractal dimension are inside the respective 95% confidence limits and differ from each other by at most 10%. It is thus encouraging that for these data from a natural, uncontrolled system the deviations among the fractal dimensions provided by different approaches and by different trajectories are quite small. This suggests that the value of the fractal dimension determined here may be a fundamental property of the flow investigated.

The fact that the dimension estimates provided by the different methods are statistically equivalent is in agreement with the "mild" multifractal behavior determined through a box-counting method, the results of which are reported in Table 3. Computing the generalized dimension  $D_q$  we have found that they differ from each other by at most 20% in the range  $1.5 \leq q \leq 6.5$ . It cannot be excluded however that the differences among the various  $D_q$ s could be explained by statistical fluctuations introduced by the finite length of the time series. However the fact that there is a well-defined trend in the dependence of the  $D_q$ s from  $q$ , seems to indicate a genuine, even if slight, multifractal nature for the drifter data.

Important technical questions concern the independence of the results of this analysis from both (a) the number of points in the time series and (b) the procedure of mean drift removal. If the drifter trajectories are cut into two or three parts and the various fractal analysis methods are

applied to each part, then the dimension estimates obtained in this way randomly differ by at most 15% from the original values. These fluctuations are consistent with the statistical uncertainties observed in our analysis, and are thus neglected in a first approximation. The smallness of the fluctuations in the value of the fractal dimension is important because it indicates that the fractal and scaling properties are nearly uniform over the entire trajectories. Another interesting question relates to whether one may be able to detect small but significant fluctuations of the fractal dimension in different oceanic regions. Although challenging, the answer to this question cannot come from the present analysis as it requires a much larger data base than available here.

Another important point concerns the removal of the mean drift current. Since we are primarily interested in scales between approximately 20 and 200 km, it seems natural to limit the effects of large scale advection, and consequently to consider some form of mean drift removal, especially for the longitude signals. In a first approximation these signals may be represented as a fluctuating part (which is the one of interest here) superimposed onto a monotonically increasing part which mimics the average advective effect of the mean flow. Removal of the mean flow is standard in the study of turbulence. We used several procedures for mean drift removal in our analysis (e.g., removing the mean velocity from the signals, or removing the linear least-square-fit trend, etc.) and in all cases we have found consistent results for the fractal dimension and the scaling exponents. The analysis of the raw data by contrast (i.e., with no mean drift removal) systematically furnished slightly lower values for the fractal dimension, a fact which is related to the systematically larger (of the order of 10%) value of the longitudinal scaling exponent  $H_x$ .

This behavior is entirely understood as spuriously generated by the "stretching" of the signal due to the mean drift and is observed in general when a fractal curve is subjected to some form of stretching along one of the dimensions. We have investigated this effect by generating a two dimensional self-similar fractal curve with a given and known dimension and then adding a linearly increasing function of time to one of its

components. This resulted in a (spurious) increase of the associated scaling exponent similar to that found in our data analysis. Thus a procedure of mean drift removal seems appropriate in our case. We notice also that the stretching of the trajectories in the mean flow is not directly related to the effects of rotation and to a possible anisotropic nature of fluid particle paths in mesoscale flows. The longitudinal elongation of the trajectories is in fact entirely produced by the advection due to the mean current. For drifter trajectories obtained in currents with a north-south orientation for example the stretching is in the latitudinal direction, with no relationship associated with the effects of rotation. It is conceivable however that an anisotropy might exist in the detrended data, since in general the variance in the east-west direction is larger (by a factor of two or three) than the variance in the meridional direction. Since however an anisotropy in the scaling behavior of the drifter data herein considered is indicated by only one of the three trajectories (NO106), we defer the important study of anisotropic scaling behavior to future analyses with larger amounts of data.

## 6. Discussion of physical implications

The fractals encountered in this study are natural fractals, as the scaling properties have been detected only in a limited (but well-defined) range of scales. An important point is now whether the limits to the scaling range are generated by statistical fluctuations and/or experimental considerations or if they reflect some fundamental dynamical limit. Basic dynamical processes active in the flow may in fact be responsible for a finite scaling range. A particular dynamical regime (active on a certain range of scales) may generate fractal behavior in its domain of validity, while other regimes (active at different scales) may be non fractal. In this case the fractal and scaling properties would be dynamically confined to a finite range of scales. The fact that certain experimental data have fractal and scaling properties over a finite range of scales may thus be an important dynamical result. Quantitatively relating the fractal properties to the actual dynamical processes active in a particular flow and carefully exploring the origin

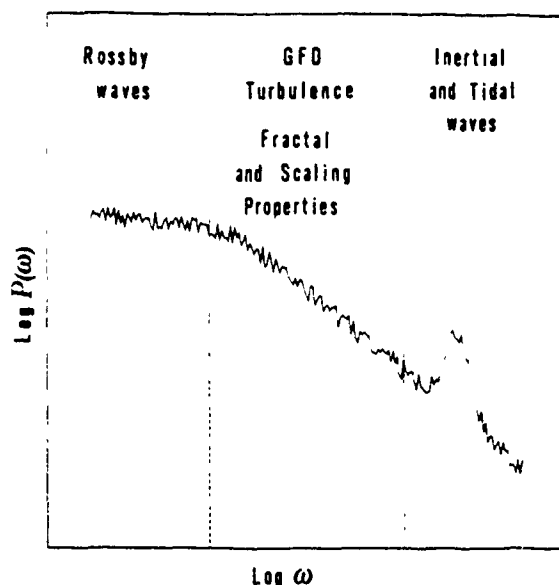


Fig. 9. Schematic power spectrum representing the different dynamical domains present in the time scales tested by the drifter trajectories.

of the finiteness of the scaling range are thus major challenges for future theoretical and experimental studies.

In the case of the data analyzed here the scale estimates determined above give a "turbulent intensity" of 15 to 20 cm/s and are in general consistent with usually accepted bounds on geostrophic or quasigeostrophic turbulence. Thus a plausible inference is that the near-surface mesoscale motions in the Kuroshio Extension exhibit fractal behavior in a range of scales usually attributed to geostrophic turbulence. Fig. 9 schematically shows a power spectrum typical of large-scale flows. For scales larger than 10 days and 100 to 200 km, the dynamics are essentially governed by Rossby waves and zonal flows. Our analysis gives no evidence of fractal and scaling properties in this regime. At the opposite side of the spectrum, i.e., for scales shorter than 2 days and 20 km, where inertial and/or tidal-wave dynamics dominate, a lack of fractal and scaling properties is observed. Between these two extreme wave regimes, the dynamics is governed by GFD turbulence and the power spectrum is thought to have a power law dependence (see, e.g., Rhines (1979) and Salmon (1982)). It is in this intermediate range of scales that we find evidence of fractality and scaling. Outside the

GFD turbulence scale range, i.e., in the Rossby or inertial/tidal wave regimes, wave dynamical processes may act to inhibit fractal behavior. In this regard it is interesting to recall a suggestion by Mandelbrot (1977, 1982) that in a Lagrangian framework one difference between laminar and turbulent flows may be in the contrast between the regular and fractal aspects of fluid parcel trajectories. Our findings apparently point in this direction also. We caution however that the limits to the scaling range determined here are essentially indicative; the drifter data are not inconsistent with the existence of a much larger scaling region. In this case, the limits of the scaling range would be of instrumental or statistical origin. In particular the lower limit to scaling could have been artificially generated by, e.g., the finite sampling time or by the positioning errors of the drifter-satellite system. Further work with other data sets is required to clarify this important issue.

A further interesting observation is that the fractal dimension of the trajectories is less than two. This implies that the drifter motions are definitely different from ordinary Brownian motion (for which  $D = 2$ ) and that, if a stochastic model is used to describe the drifter paths, it must possess some form of persistency or "memory" which is not found in Brownian random walks. The fact that  $D < 2$  also implies that the drifter motions do not explore and fill the entire plane of the ocean surface, as would be done by Brownian motion.

The principal results obtained here are summarized as follows. Each of the 6 signals has been analyzed by four different methods to determine fractal behavior. Remarkable consistency has been found in the results, which indicate a fractal nature for the drifter trajectories in the range of scales typical of GFD turbulence. It is encouraging that data from a large-scale natural flow, analyzed with four independent techniques, give the same fractal properties. Because these observations come from an uncontrolled experiment in a natural environment, this consistency could not be assumed a priori. We also note that this is evidently the first experimental indication that fluid parcel trajectories in large-scale flows can exhibit fractal behavior. The drifter trajectories have also been shown to possess a "mild" multifractal character. While in general the introduc-

tion of multifractality (associated with multiplicative random processes) is an important step toward the understanding of the links between fractal behavior and dynamical processes, for the particular data set studied here, we observe that a satisfactory first-order approximation is probably represented by simple additive processes such as fractional Brownian motions.

We hope that the results discussed here will provide a stimulus to search for fundamental reasons why fractal behavior might occur in flows of this type. A number of important questions are still to be answered. How fundamental dynamical motions generate fractal behavior remains in fact an open crucial question. The implications from a growing body of literature (see, e.g., Mandelbrot, 1974, 1975, 1977, 1982; Frisch et al., 1978; Frisch, 1985; Frisch and Parisi, 1985; Lovejoy and Mandelbrot, 1985; Sreenivasan and Meneveau, 1986; Meneveau and Sreenivasan, 1987; Schertzer and Lovejoy, 1987; Paladin and Vulpiani, 1987) are that there are several deep connections between the nonlinear dynamics generated by the partial differential equations of motion and fractal properties. While these connections are still to be understood it is to be expected that further theoretical clarification is forthcoming. For these reasons, it is important, in our opinion, to continue and to expand on experimental studies which can help shed light on the various aspects of fractal properties and to perhaps provide some insight about possible directions in which theoretical investigations might most fruitfully go. Several important physical questions are open in this context, such as for example: (1) Is the observed value of the fractal dimension common to all fluid parcel trajectories in GFD turbulent flows? How much different is the case of three dimensional turbulence? (2) Are the power spectra obtained for these data typical of Lagrangian GFD turbulence and may they be directly derived through some cascading argument? (3) Are the multifractal properties important and can they be stronger than those determined here? (4) Are the drifter motions (around the mean flow) isotropic or anisotropic? (5) Can one identify the scaling properties of the underlying (Lagrangian) equations of motion? Is it possible to derive the value of the fractal dimension from the equations of motion? (6) Can the drifter trajectories be modeled by (non-

gaussian) stochastic approaches or is there the need for a truly nonlinear deterministic model? (7) What is the relationship between the fractal behavior and the statistical properties of the system? Although these, and many other, fundamental issues are still to be addressed, we believe that the study of the fractal and scaling behavior of large-scale flows in a Lagrangian framework may provide added insight into the fundamental properties of large-scale motions.

## 7. Acknowledgements

We acknowledge Professor C. Castagnoli, Director of the Istituto di Cosmo geofisica del

Consiglio Nazionale delle Ricerche, for continuing support and valuable encouragement. This research has received funding from the Consiglio Nazionale delle Ricerche and from the Ministero della Pubblica Istruzione. A. D. Kirwan gratefully acknowledges the support of the Office of Naval Research (Contract N00014-89-J-1595) and of the National Science Foundation (Grant OCE8811453) and the Samuel L. and Fay M. Slover endowment to Old Dominion University. During part of this research A. Provenzale was supported by a fellowship from the "Dottorato di Ricerca in Fisica" at the University of Torino, Italy.

## REFERENCES

- Benzi, R., Paladin, G., Parisi, G. and Vulpiani, A. 1984. On the multifractal nature of fully developed turbulence and chaotic systems. *J. Physics A* **17**, 3521-3531.
- Bernstein, R. L. and White, W. B. 1979. Zonal variability in the distribution of eddy energy in the mid-latitude North Pacific Ocean. *J. Phys. Oceanogr.* **7**, 123-126.
- Bernstein, R. L. and White, W. B. 1981. Stationarity and traveling mesoscale perturbations in the Kuroshio extension current. *J. Phys. Oceanogr.* **11**, 692-704.
- Davis, R. E. 1982. On relating Eulerian and Lagrangian velocity statistics: single particles in homogeneous flows. *J. Fluid Mech.* **114**, 1-26.
- Davis, R. E. 1983. Oceanic property transport, Lagrangian particle statistics, and their prediction. *J. Mar. Res.* **41**, 163-194.
- Davis, R. E. 1985. Drifter observations of coastal surface currents during CODE: The statistical and dynamical views. *J. Geophys. Res.* **90**, 4756-4772.
- Eckmann, J. P. and Ruelle, D. 1985. Ergodic theory of strange attractors. *Rev. Mod. Phys.* **57**, 617-656.
- Fahrbach, E., Brockmann, C. and Meincke, J. 1986. Horizontal mixing in the Atlantic equatorial undercurrent estimated from drifting buoy clusters. *J. Geophys. Res.* **91**, 10557-10565.
- Frisch, U. 1981. Fully developed turbulence and singularities. In: *Chaotic behaviour of deterministic systems* (eds. G. Iooss, H. G. Helleman and R. Stora). Amsterdam: North Holland, 665-704.
- Frisch, U. 1985. Fully developed turbulence and intermittency. In: *Turbulence and predictability in geophysical fluid dynamics and climate dynamics*. Proc. Int. School of Physics "Enrico Fermi," Course LXXXVIII (eds. M. Ghil, R. Benzi and G. Parisi). Amsterdam: North Holland, 71-88.
- Frisch, U. and Morf, R. 1981. Intermittency in nonlinear dynamics and singularities at complex times. *Phys. Rev.* **A23**, 2673-2705.
- Frisch, U. and Parisi, G. 1985. On the singularity structure of fully developed turbulence. In: *Turbulence and predictability in geophysical fluid dynamics and climate dynamics*. Proc. Int. School of Physics "Enrico Fermi," Course LXXXVIII (eds. M. Ghil, R. Benzi and G. Parisi). Amsterdam: North Holland, 84-88.
- Frisch, U., Sulem, P. L. and Nelkin, M. 1978. A simple dynamical model of intermittent fully developed turbulence. *J. Fluid Mech.* **87**, 719-736.
- Grassberger, P. and Procaccia, I. 1983. Measuring the strangeness of strange attractors. *Physica* **9D**, 189-208.
- Halsey, T. C., Jensen, M. H., Kadanoff, L. P., Procaccia, I. and Shraiman, B. I. 1986. Fractal measures and their singularities: The characterization of strange sets. *Phys. Rev.* **A33**, 1141-1151.
- Hofmann, E. E. 1985. The large-scale horizontal structure of the Antarctic circumpolar current from FGGE drifters. *J. Geophys. Res.* **90**, 7087-7097.
- Kirwan, A. D., Jr., McNally, G. J., Reyna, E. and Merrell, W. J., Jr. 1978. The near-surface circulation of the eastern North Pacific. *J. Phys. Ocean.* **8**, 937-945.
- Kirwan, A. D., Jr., McNally, G. J. and Pazan, S. 1978. Wind drag and relative separations of undrogued drifters. *J. Phys. Ocean.* **8**, 1146-1150.
- Kirwan, A. D., Jr., McNally, G. J., Pazan, S. and Wert, R. 1979. Analysis of surface current response to wind. *J. Phys. Ocean.* **9**, 401-412.
- Kirwan, A. D., Jr. and Cresswell, G. R. 1982. Observations of large and mesoscale motions in the near surface layer. In: *Topics in ocean physics*. Proc. Int. School of Physics "Enrico Fermi," Course LXXX

- (eds. A. R. Osborne and P. Malanotte Rizzoli). Amsterdam: North Holland, 79-125.
- Krauss, W., Dengg, J. and Hinrichsen, H.-H. 1989. The response of drifting buoys to currents and winds. *J. Geophys. Res.* **94**, 3201-3210.
- Large, W. J. and Van Loon, H. 1989. Large scale, low frequency variability of the 1979 FGGE surface buoy drifts and winds over the southern hemisphere. *J. Phys. Ocean.* **19**, 216-232.
- Lovejoy, S. 1982. The area-perimeter relationship for rain and cloud areas. *Science* **216**, 185-187.
- Lovejoy, S. and Mandelbrot, B. B. 1985. Fractal properties of rain, and a fractal model. *Tellus* **37A**, 209-232.
- Lovejoy, S., Schertzer, D. and Tsonis, A. A. 1987. Functional boxcounting and multiple elliptical dimensions in rain. *Science* **235**, 1036-1038.
- Mandelbrot, B. B. 1967. How long is the coast of Britain? Statistical self-similarity and fractional dimension. *Science* **155**, 636-638.
- Mandelbrot, B. B. 1972. Possible refinement of the lognormal hypothesis concerning the distribution of energy dissipation in intermittent turbulence. In: *Statistical models and turbulence* (eds. M. Rosenblatt and C. Van Atta). Berlin: Springer Verlag, 333-351.
- Mandelbrot, B. B. 1974. Intermittent turbulence in self-similar cascades: divergence of high moments and dimension of the carrier. *J. Fluid Mech.* **62**, 331-358.
- Mandelbrot, B. B. 1975. On the geometry of homogeneous turbulence, with stress on the fractal dimension of the iso-surfaces of scalars. *J. Fluid Mech.* **72**, 401-416.
- Mandelbrot, B. B. 1977. *Fractals: form, chance and dimension*. San Francisco: Freeman.
- Mandelbrot, B. B. 1982. *The fractal geometry of nature*. San Francisco: Freeman.
- McNally, G. J. 1981. Satellite-tracked drift buoy observations of the near-surface flow in the eastern mid-latitude North Pacific. *J. Geophys. Res.* **86**, 8022-8030.
- McNally, G. J., Patzert, W. C., Kirwan, A. D., Jr. and Vastano, A. C. 1983. The near-surface circulation of the North Pacific using satellite tracked drifting buoys. *J. Geophys. Res.* **88**, 7507-7518.
- McNally, G. J. and White, W. B. 1985. Wind driven flow in the mixed layer observed by drifting buoys during autumn-winter in the midlatitude North Pacific. *J. Phys. Ocean.* **15**, 684-694.
- Meneveau, C. and Sreenivasan, K. R. 1987. The multifractal spectrum of the dissipation field in turbulent flows. In: *Chaos '87* (ed. M. Duong-Van). Nucl. Phys. B (Proc. Suppl.) **2**, 49-76.
- Molinari, R. L., Spillane, M., Brooks, I., Atwood, D. and Duckett, C. 1981. Surface currents in the Caribbean Sea as deduced from Lagrangian observations. *J. Geophys. Res.* **86**, 6537-6542.
- Osborne, A. R., Kirwan, A. D., Jr., Provenzale, A. and Bergamasco, L. 1986. A search for chaotic behaviour in large and mesoscale motions in the Pacific Ocean. *Physica* **23D**, 75-83.
- Osborne, A. R. and Provenzale, A. 1989. Finite correlation dimension for stochastic processes with power law spectra. *Physica D*, in press.
- Owens, W. B. 1984. A synoptic and statistical description of the Gulf Stream and subtropical gyre using SOFAR floats. *J. Phys. Ocean.* **14**, 104-113.
- Paladin, G. and Vulpiani, A. 1987. Anomalous scaling laws in multifractal objects. *Phys. Reports* **156**, 147-225.
- Panchev, S. 1971. *Random functions and turbulence*. Oxford: Pergamon.
- Peterson, R. G. 1985. Drifter trajectories through a current meter array at Drake Passage. *J. Geophys. Res.* **90**, 4883-4893.
- Pietronero, L. and Tosatti, E. 1986. *Fractals in physics*. Amsterdam: North Holland.
- Rhines, P. B. 1979. Geostrophic turbulence. *Ann. Rev. Fluid Mech.* **11**, 401-441.
- Richardson, P. L. 1983. Eddy kinetic energy in the North Atlantic from surface drifters. *J. Geophys. Res.* **88**, 4355-4367.
- Royer, T. C. and Emery, W. J. 1984. Circulation in the Bering Sea, 1982-82, based on satellite-tracked drifter observations. *J. Phys. Ocean.* **14**, 1914-1920.
- Salmon, R. 1982. Geostrophic turbulence. In: *Topics in ocean physics*. Proc. Int. School of Physics "Enrico Fermi," Course LXXX (eds. A. R. Osborne and P. Malanotte Rizzoli). Amsterdam: North Holland, 30-78.
- Schertzer, D. and Lovejoy, S. 1983. Elliptical turbulence in the atmosphere. *Proceedings of the 4th Symposium on Turbulent Shear Flows*, 1-11 Nov. Karlsruhe: University of Karlsruhe Press.
- Schertzer, D. and Lovejoy, S. 1987. Physical modeling and analysis of rain and clouds by anisotropic scaling multiplicative processes. *J. Geophys. Res.* **92**, 9693-9714.
- Schmitz, W. J., Jr., Price, J. F., Richardson, P. L., Owens, W. B. and Webb, D. C. 1981. A preliminary exploration of the Gulf Stream system with SOFAR floats. *J. Phys. Ocean.* **11**, 1194-1204.
- Schmitz, W. J., Jr. 1982. Abyssal eddy energy levels in the western North Pacific. *J. Phys. Ocean.* **14**, 198-201.
- Schmitz, W. J., Jr., Niiler, P. P., Bernstein, R. L. and Holland, W. R. 1982. Recent long-term mooring and instrument observation in the western North Pacific. *J. Geophys. Res.* **87**, 9425-9440.
- Shaw, P.-T. and Rossby, H. T. 1984. Towards a Lagrangian description of the Gulf Stream. *J. Phys. Ocean.* **14**, 528-540.
- Sreenivasan, K. R. and Meneveau, C. 1986. The fractal facets of turbulence. *J. Fluid Mech.* **173**, 357-386.
- Vastano, A. C., Hagan, D. E. and McNally, G. J. 1985. Lagrangian observation of surface circulation at the Emperor Seamount Chain. *J. Geophys. Res.* **90**, 3325-3331.

## Observed and Simulated Kinematic Properties of Loop Current Rings

A. D. KIRWAN, JR.,<sup>1,2</sup> J. K. LEWIS,<sup>3</sup> A. W. INDEST,<sup>4</sup> P. REINERSMAN,<sup>1</sup> AND I. QUINTERO<sup>1</sup>

Two rings, shed by the Loop Current in 1980 and 1982, were observed for several months by satellite-tracked drifters to migrate across the Gulf of Mexico. The drifter path data have been inverted to obtain estimates of the paths of the centers of the two rings, ring shape, and the swirl velocities. Three drifters were deployed in the 1980 ring, and the analysis of that data set establishes the variability of the above kinematic estimates for one ring. A comparison of the analysis of data from both rings provides some idea on inter-ring variability. Both rings impacted the Mexican continental slope at about 22.8°N, 95.5°W. After a brief adjustment period, both rings reestablished and maintained a vortex character for several months in the slope region while migrating slowly to the north. The paths of the centers of the two rings along the slope are virtually identical. The same analysis routine was applied to some simulated drifter data obtained from the Hurlburt and Thompson (1980) Gulf of Mexico primitive equation model. In the midgulf, the agreement between the observed rings and the simulated ring is good, although the former showed stronger interaction with the continental slope topography and/or circulation than was seen in the latter. Along the slope, the model ring kinematic characteristics were in extraordinary agreement with the observations.

## 1. INTRODUCTION

The circulation of the Gulf of Mexico has been the subject of a surprising amount of theoretical and observational studies. From the turn of the century [Sweitzer, 1898] until 1973 [Austin, 1955; Nowlin and McClellan, 1967; Nowlin, 1972], the emphasis was on analyses of hydrographic data. These studies established the presence of poorly defined, but quasi-permanent, anticyclonic signatures in the central part of the gulf.

Since 1973, the emphasis has shifted from qualitative descriptions of the hydrography to attempts at quantifying dynamical mechanisms associated with the anticyclonic structures. Sturges and Blaha [1976] and Blaha and Sturges [1978] proposed that the western gulf circulation was the result of the balance of wind stress curl and planetary vorticity, i.e., a mini-western boundary current effect in the Gulf of Mexico. Elliot [1979, 1982] disputed this, noting that this balance was not generally achieved if synoptic wind data on a fine scale were used. His work also gave more credence to the earlier idea of Ichiye [1962] that the anticyclonic features were in fact rings that had been shed by the Loop Current in the eastern gulf. Kirwan *et al.* [1984a] substantiated this hypothesis by tracking the migration of a ring shed by the Loop Current across the gulf to the continental shelf off of Mexico.

In a companion paper, Kirwan *et al.* [1984b] assessed the translation velocities, local vorticity, deformation rates, and shape of the ring as it propagated across the gulf. The analyses of the three drifters that were in the ring simultaneously showed generally good agreement of these properties. The results also are in general qualitative agreement with the nu-

merical simulations from the general circulation model (GCM) of Hurlburt and Thompson [1980], hereinafter referred to as HT.

Is the qualitative agreement between GCM calculations and one particular ring fortuitous or the result of deterministic dynamics? We examine this question with observations from two different rings along with simulated data from the HT model. Specifically, we compare in detail kinematic properties such as the movement of ring centers, ring translation and swirl velocities, and ring shapes from 1980-1981, 1982-1983, and simulations from the HT GCM.

The analysis routine used to determine these kinematic properties is an improved version of that reported by Kirwan *et al.* [1984b]. The routine inverts Lagrangian path data to obtain the desired kinematic properties. Unlike the earlier study, the present routine emphasizes ring shape and translation. Also, considerably better time resolution on parameter estimates can be made with the new routine. Some details are given below and in the appendix. The internal consistency of the analysis routine is being assessed separately with simulated data from the HT GCM.

The following observed data were utilized in this study. These come from two rings which occurred in 1980-1981 and 1982-1983. We have reported previously on the former [see Kirwan *et al.*, 1984a, b] using the more primitive analysis routine. That ring had three drifters in it simultaneously, and so our re-analysis provides some indication of intraring variability along with some indication of the consistency of the analysis routine. Only a descriptive analysis of the latter ring, which had only one drifter, has been reported before [Lewis and Kirwan, 1985]. Comparison of these two rings provides some measure of inter-ring variability.

These observed data are compared with simulated Lagrangian data from the HT GCM. This model was a two-layer (lower layer active) nonlinear primitive equation model of the Gulf of Mexico with realistic bottom topography. The grid spacing for the calculations used here was 10 km. The simulated path was obtained by advecting a parcel at each model time step (4 hours) to a new position given by the product of the velocity vector at the current position of the parcel and the time step. Since the position of the parcel was rarely at a grid point, it was usually necessary to interpolate the velocity vector from surrounding grid points. These calculations were kindly performed by A. Wallcraft.

<sup>1</sup>Department of Marine Sciences, University of South Florida, Saint Petersburg.

<sup>2</sup>Now at Department of Oceanography, Old Dominion University, Norfolk, Virginia.

<sup>3</sup>Science Applications International Corporation, College Station, Texas.

<sup>4</sup>Department of Oceanography, Old Dominion University, Norfolk, Virginia.



Both the observations and the simulations track appropriate rings for many months. During this time, the real and simulated rings move from the midgulf region with fairly flat topography in excess of 3000 m to the continental slope off of Mexico. This area of interest is depicted in Figure 1. In the midgulf region, ring translations are governed essentially by Rossby wave dynamics, and so one expects them to move west-southwest. But along the slope, interactions of the ring with bottom topography become important. Since the dynamics in these two geographic regions are so different, we have performed separate analyses for the rings in the two regions.

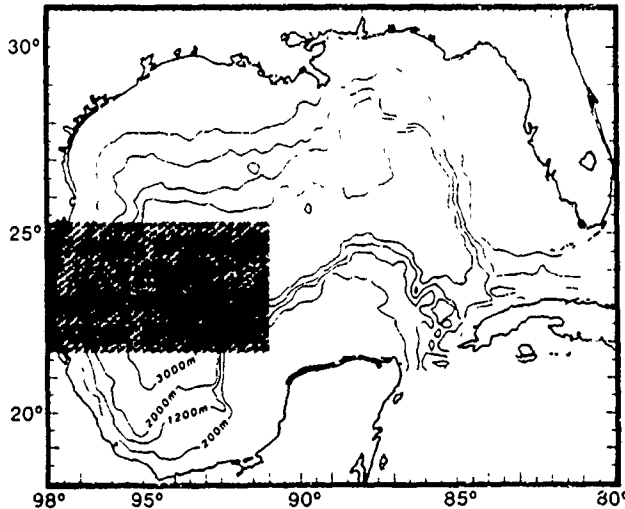


Fig. 1 Depiction of the area in which the observed and simulated Loop Current rings are studied.

## 2. ANALYSIS PROCEDURE

The observations used in this study are the positions of the Polar Research Laboratory drifters with Argos identifications 1598, 1599, 1600, and 3374. Kirwan *et al.* [1984a, b] reported on the analysis of 1598, 1599, and 1600, which were deployed simultaneously in November 1980. Position data from these three drifters are analyzed to establish the variability within a ring. Intraring variability is assessed by comparing the analysis performed on the three drifters in the 1980–1981 ring with that of drifter 3374, which was deployed in the 1982–1983 ring. Each drifter was the standard Polar Research Laboratory buoy drogued by a 200-m thermistor line. No thermistor data are available from any of these units.

The analysis procedure utilizes a parametric kinematic model discussed by Kirwan *et al.* [1984b] for inferring the translation and swirl velocities as well as the vorticity, horizontal divergence, and deformation rates. This model was first proposed by Okubo [1970] to describe small-scale motion about flow singularities. Kirwan [1984] showed that same model can be applied to larger scales if the model parameters are constant along a parcel path.

The model assumes that the swirl velocity is given as a linear function of the distance from a local flow center. Here the local parcel flow center will be referred to as the "ring center" or some times "orbit-determined center". This terminology is dictated only by the nature of the available data.

Flierl [1981] has pointed out that this center may not coincide with an "Eulerian" center. (We interpret this as a center of mass.) Smith and Reid [1982] have developed a general formalism for studying the centers of the distribution on any property, for example, mass, potential energy, kinetic energy or enstrophy. In general, these centers do not coincide, nor do their propagation velocities. Establishing the relations between these various centers for Gulf of Mexico rings requires much more data than is now available.

For the present model the total velocity ( $u, v$ ) of a drifter is composed of the translation velocity ( $U_T, V_T$ ) of the ring center and the swirl velocity ( $u_s, v_s$ ):

$$u = U_T + u_s \quad (1)$$

$$v = V_T + v_s$$

$$u_s = (d + a)x/2 + (h - c)y/2 \quad (2)$$

$$v_s = (b + c)x/2 + (d - a)y/2$$

Here  $x$  and  $y$  are the instantaneous coordinates, relative to the ring center of a particular parcel (drifter). If (2) is regarded as a Taylor expansion for the velocity field, then the parameters  $a$  and  $b$  can be interpreted as deformation rates and  $c$  and  $d$  as the vertical vorticity and horizontal divergence. It is stressed that these parameters are evaluated along individual paths. Eulerian estimates of deformation rates, vorticity, and divergence likely would differ from these estimates. Consequently, it is better to interpret  $a, b$ , and  $c$  as shape functions which determine the orientation and ellipticity of a particular orbit in a ring. See Kirwan *et al.* [1984b] for details.

The general solution to (1) and (2) is easily obtained [Okubo, 1970]. The procedure here is to apply this solution to every time interval between fixes (in practice, interpolated positions). Thus for the interval  $t_k \leq t \leq t_{k+1}$ , one obtains

$$u_k = U_{Tk} + (d_k + a_k)x_k/2 + (b_k - c_k)y_k/2 \quad (3)$$

$$v_k = V_{Tk} + (b_k + c_k)x_k/2 + (d_k - a_k)y_k/2 \quad (4)$$

where

$$x_k = \{ \exp [r_{1k}(t - t_k)] [X_k(\sqrt{a_k^2 + b_k^2 - c_k^2} + a_k) + Y_k(b_k - c_k)] - \exp [r_{2k}(t - t_k)] [X_k(a_k - \sqrt{a_k^2 + b_k^2 - c_k^2}) + Y_k(b_k - c_k)] - 2\sqrt{a_k^2 + b_k^2 - c_k^2} \} \quad (5)$$

$$y_k = \{ \exp [r_{1k}(t - t_k)] [X_k(b_k + c_k) + Y_k(\sqrt{a_k^2 + b_k^2 - c_k^2} - a_k)] + \exp [r_{2k}(t - t_k)] [-X_k(b_k + c_k) + Y_k(\sqrt{a_k^2 + b_k^2 - c_k^2} + a_k)] - 2\sqrt{a_k^2 + b_k^2 - c_k^2} \} \quad (6)$$

In (5) and (6), ( $X_k, Y_k$ ) are the coordinates of the parcel in question at time  $t = t_k$  relative to the ring center. Also,

$$r_{1k} = (d_k + \sqrt{a_k^2 + b_k^2 - c_k^2})/2 \quad (7)$$

$$r_{2k} = (d_k - \sqrt{a_k^2 + b_k^2 - c_k^2})/2 \quad (8)$$

are the eigenvalues of the matrix

$$2M_k = \begin{bmatrix} (d_k + a_k) & (b_k - c_k) \\ (b_k + c_k) & (d_k - a_k) \end{bmatrix}$$

Note that these eigenvalues are complex conjugates when  $c_k^2 > a_k^2 + b_k^2$ . This, naturally, produces real periodic solu-

tions which are a characteristic of swirl velocities of drifters trapped in a ring.

To apply this model to drifter data, differentiate (3) and (4) three times with respect to time. One side of these equations contains the unknown variable set  $Z_k = (a_k, b_k, c_k, d_k, X_k, Y_k)$ . The other side of these equations can be estimated from path data. These six equations do not contain the translation velocity, since it is assumed a priori to be constant for a time interval. (But, of course, its value may change from one time interval to the next.) These six equations are inverted analytically for the six elements of  $Z_k$ . The translation velocities can be recovered from (3) and (4), since all other quantities are now known. Alternatively, the translation velocities can be obtained by differentiating the path of the ring center. Both procedures provide comparable estimates. Here we use the latter procedure. With all elements of  $Z_k$  now determined, one then moves to the next time interval and repeats the calculations, thus obtaining a time series of  $Z_k$ . Details are given in the appendix.

We have expended a great deal of effort in learning how to make reliable time derivative estimates of the path data. For the data analyzed here, the raw position files have been edited, interpolated to equally spaced time intervals, and low-pass filtered (half power point of 100 hours). All derivative estimates were obtained by fourth-order accurate, centered difference schemes. Each derivative file was edited and low-pass filtered. The calculations, as described in the appendix for  $Z_k$ , were performed with the latter derivative files. The calculated  $Z_k$ , in turn, were edited and low-pass filtered.

The analysis procedure just outlined is an improvement over that used by Kirwan *et al.* [1984b]. Their method required an a priori assignment of a solution form to (4) and (5); i.e., (7) and (8) were assumed to be complex conjugates, and values of  $Z_k$  were assumed to be constant over one ring revolution (approximately 15 days). The procedure used here does not require an a priori assignment of the solution form; it lets the data determine this. Thus it should have wider utility. In addition, the  $Z_k$  are now required to be constant over seven time intervals (42 hours in the present case) rather than 2 weeks.

As was indicated above,  $a$ ,  $b$ , and  $c$  are not especially useful for comparison with Eulerian data. For rings a more appropriate description would be the elliptical structure of the orbit traversed by a particular drifter. As was shown by Kirwan *et al.* [1984b], the characteristic equation is

$$(c_k + b_k)x_k^2 + (c_k - b_k)y_k^2 - 2a_kx_ky_k = L_k \exp[-d_k(t - t_k)] \quad (9)$$

Here  $L_k$  is the angular momentum per unit mass relative to the ring center. This can be calculated directly (see equation (A18)). In (9) the argument in the exponential term can be made zero by making the evaluation at the beginning of the time interval  $t = t_k$ . Note that a requirement for (9) to describe an ellipse is that  $c_k^2 > a_k^2 + b_k^2$ .

From analytic geometry it is known that for anticyclonic motion,  $c_k < 0$ , the major axis of the ellipse makes an angle with east of

$$\alpha_k = \frac{1}{2} \tan^{-1}(-a_k/b_k) \quad (10)$$

In evaluating (10), care must be exercised in the quadrant assignment. Also, the semilength of the major axis is

$$R_k = \sqrt{L_k/(c_k - h_k)} \quad (11)$$

where

$$h_k^2 = a_k^2 + b_k^2$$

The paradigm just outlined for analysis of Lagrangian data puts critical emphasis on time derivatives of path data. Inconsequential errors in the path data can become consequential in the derivative estimates. Moreover, the nonlinear algebraic combinations of these derivatives in the paradigm may magnify further the impact of these errors on the inversion. The concern is that two paths which contain the same kinematic information but differ by small random and/or round off errors, will produce vastly different kinematic estimates when run through the paradigm. The internal consistency of estimates of ring kinematics is presently being examined with simulated data from the HT GCM.

### 3. MIDGULF

#### 3.1. Observations

Here the results of the intraring and inter-ring comparisons are presented for the midgulf region. This includes ring kinematics as inferred from the three drifters in the 1980–1981 ring and the single drifter in the 1982–1983 ring. While in the midgulf region, both rings began to interact with the continental slope topography and/or circulation. This period is isolated in the analysis. The same analysis routine is then applied to simulated midgulf ring data from the HT GCM.

*The 1980–1981 ring.* The data for this portion of the study come from three drifters (1598, 1599, and 1600) which were seeded in the 1980–1981 ring. Kirwan *et al.* [1984a, b] have already reported on this. The data have been reanalyzed using the general algorithm discussed in the preceding section and in the appendix.

Figure 2 shows the paths of these three drifters in the midgulf region along with the positions of the centers and the orbit ellipses. Arrows on the drifter and center paths mark 10-day intervals, while the ellipses are presented at 15-day intervals. The paths for each drifter are for a common time interval (day 340, 1980, to day 118, 1981). This figure establishes three points. First, all three make the same swath through this portion of the gulf, suggesting that they generally followed the ring. The overall path characteristics of drifters 1598 and 1600 (Figures 2a and 2c) are remarkably similar, suggesting that they were in very similar orbits. Second, the paths for the center of the ring, as determined independently from the three drifters, is in good agreement as far as about 94°W (the first 2 months of the record). Discounting the very beginning where there are numerical problems, the typical difference in the location of the center at any one time is 30 km, about 20% of the diameter of the ring as determined from satellite imagery [Kirwan *et al.*, 1984b]. This is about 10 km larger than the rms displacement between the maximum surface and interface displacement anomalies of the HT GCM. The 30-km variability is considerably larger than that reported by Hooker and Olson [1984] using a variant of the technique employed here under ideal conditions. In view of our results along the continental slope, described below, it is not clear whether the large variability is due to data, technique, or rapid evolution of the ring.

Finally, the ellipses also show generally good agreement east of 94°W. Note the tendency to develop a northwest elon-

gation as the ring approaches 94°W. West of 94°W, all three orbits suggest that the ring begins to interact with the continental slope circulation and/or topography. This is discussed later.

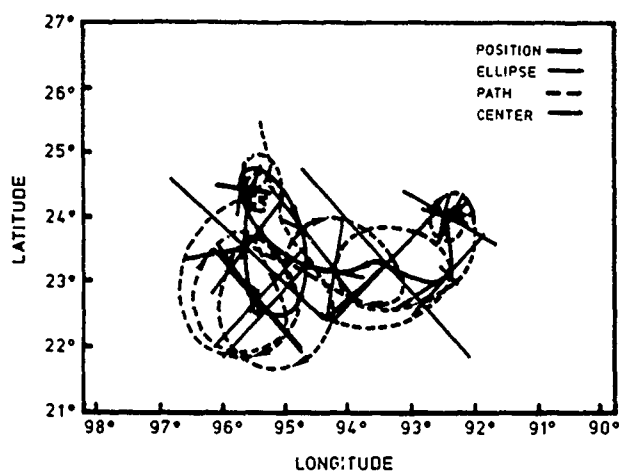


Fig. 2a

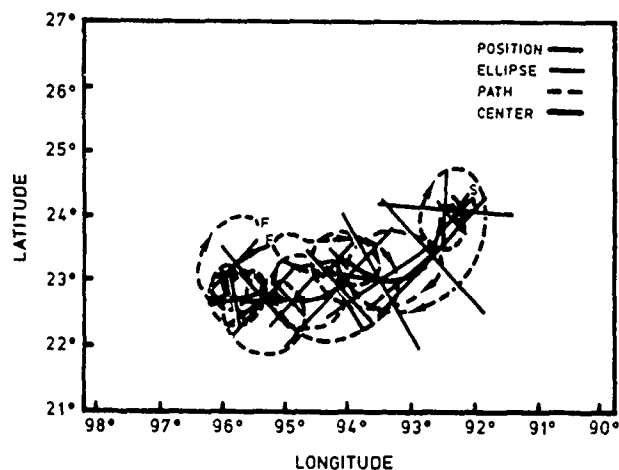


Fig. 2b

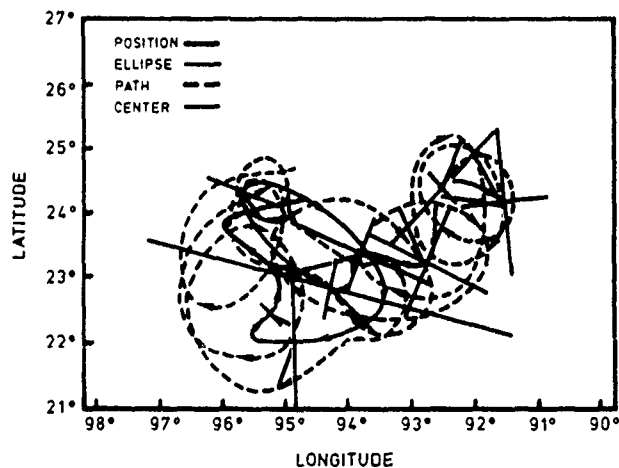


Fig. 2c

Fig. 2. Drifter paths, inferred center path (red) and orbit ellipse (blue) for the three drifters in the 1980–1981 ring: (a) 1598, (b) 1599, and (c) 1600. Arrows on the paths are at 10-day intervals, while the ellipses are shown at 15-day intervals. Here S and F refer to start and finish.

Figure 3 shows the time series for the swirl and translation velocities. All three records indicate swirl velocities in excess of 50 cm/s throughout most of the record. The dominant period is about 14 days with a variation of about 2 days between the records. This is recognized as the ring's rotation period. However, from about day 30 to 60, 1981, all three drifters show a smaller-period component (about 5 days) in the time series and a decrease in swirl amplitude. As will be discussed below,

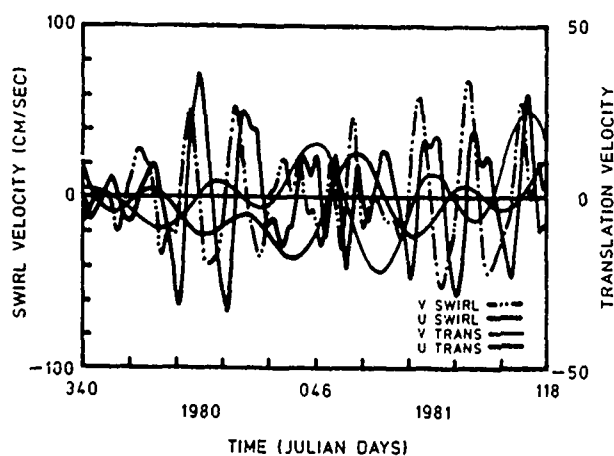


Fig. 3a

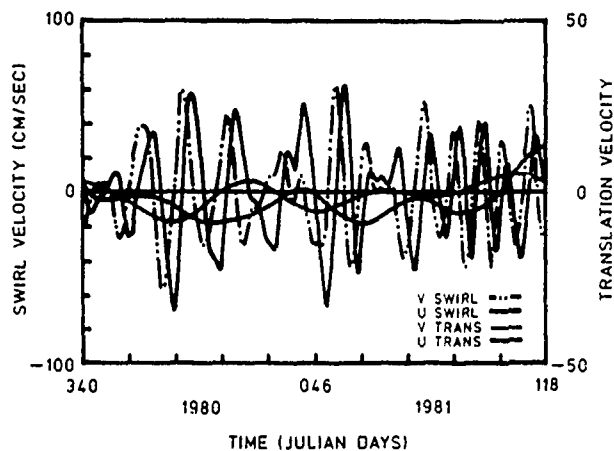


Fig. 3b

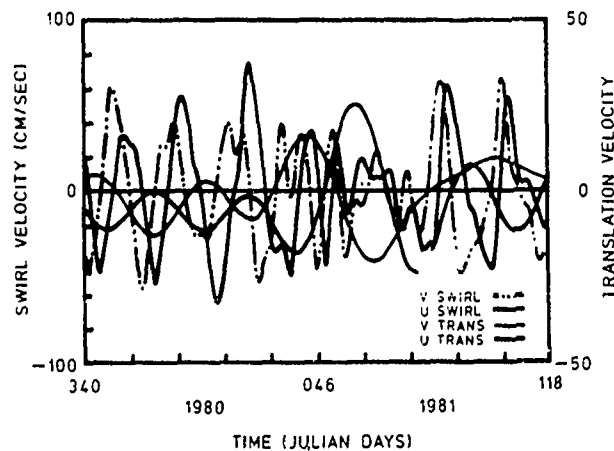


Fig. 3c

Fig. 3. Swirl (left scale) and translation velocities (right scale) inferred from the three drifters in the 1980–1981 ring. (a) 1598, (b) 1599, and (c) 1600. The east and north components of the translation velocity are depicted in red and blue, respectively.

it is speculated that during this period the drifters were responding to effects produced by the continental slope and/or circulation further to the west. All the translation velocities show a consistent westward component of about 4 cm/s up until about day 30, 1981. For the reason just given, it is not clear that the analysis applies to this ring for the period from day 30, 1981, to day 60, 1981. After day 60, 1981, the ring centers appear to be stationary.

*The 1982–1983 ring and comparison with the 1980–1981 ring.* The same characteristics are seen in the analysis for the 1982–1983 ring. Figure 4 shows the drifter path, inferred center path, and the orbit ellipses for drifter 3374. As in Figure 2, there is significant distortion of the orbits west of 94°W. Unlike the earlier ring, no significant northwest ellipticity is developed as the ring approaches 94°W. Comparison with Figure 2 indicates that the 1982–1983 ring center followed nearly the same path as that of the 1980–1981 ring.

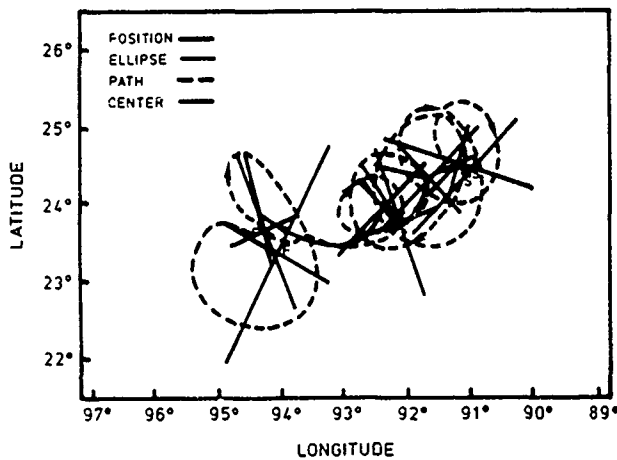


Fig. 4 Drifter path, inferred center path (red), and orbit ellipse (blue) for the drifter in the 1982–1983 ring. Arrows on the paths are at 10-day intervals, while the ellipses are shown at 15-day intervals.

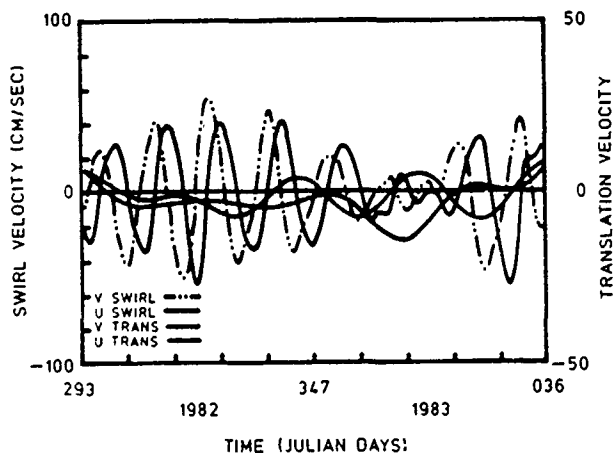


Fig. 5 Swirl (left scale) and translation velocities (right scale) inferred from the three drifters in the 1982–1983 ring. The east and north components of the translation velocity are depicted in red and blue, respectively.

Figure 5 shows the translation and swirl velocities for the 1982–1983 ring. The swirls are slightly less than 50 cm/s, which could reflect a smaller orbit of the drifter. The dominant period is still about 14 days. Note that around day 1, 1983 the

swirl velocities decrease significantly and show some evidence of higher-frequency components. This is the period when the drifter moves west of 94°W and executes the deformed, northwest-oriented loop. As with the earlier ring, this is interpreted as evidence for topographic and/or slope circulation interactions.

Figure 2 indicates that west of 94°W, the three drifters in the 1980–1981 ring show significant divergence in the calculation of the inferred center. Furthermore, drifters from both rings showed anomalous path characteristics in this region. In particular, 1598 and 1600 appeared to become entrained in smaller, anticyclonic eddies, while 1599 and 3374 exhibited warped and elongated ellipses. This has been attributed to interaction between the ring and the continental slope and/or slope circulation further to the west.

Figure 6 focuses on this time interval. Figure 6a shows the paths of all four drifters during the period in question. It is clear from this that all four drifters were under the influence of different dynamical processes here than those they experienced to the east.

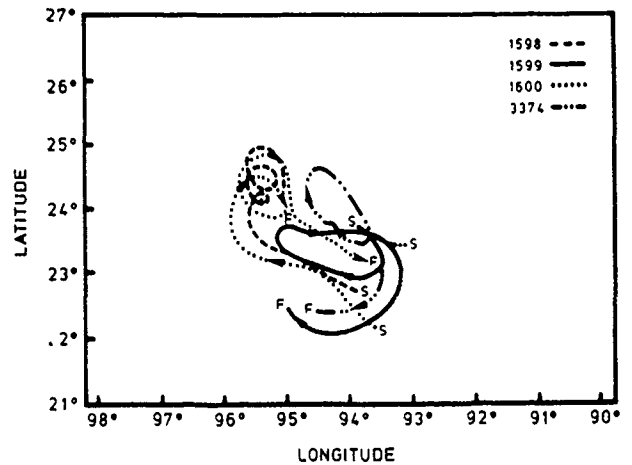


Fig. 6a

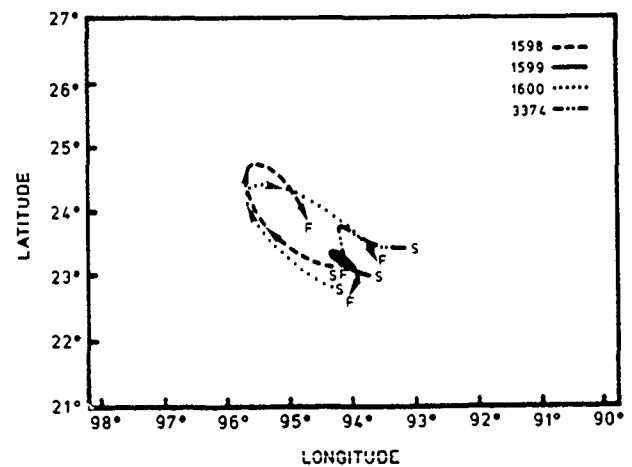


Fig. 6b

Fig. 6. Paths of drifters 1598, 1599 and 1600 in the 1980–1981 ring and 3374 in the 1982–1983 ring for the period when they were interacting with the slope topography and/or circulation. The arrows are at 10-day intervals. (a) Drifter paths. (b) Inferred centers of flow.

Figure 6b compares the movement of the inferred centers. In interpreting this figure, it should be emphasized that the center calculation is greatly complicated by the changes in curvature of the paths. The paradigm interprets this as a

change from an anticyclonic to cyclonic structure with a consequent change in the location of the center. No doubt the real dynamics during this period are much more complicated than the rather simple scenario available from the kinematic model. The geographic variation in the paths clearly is much larger than that seen east of  $94^{\circ}\text{W}$  or, as will be seen shortly, than that found along the slope. This suggests that each of these drifters was either briefly pulled out of the parent ring or its orbits deformed through interaction with the continental slope topography or circulation. This hypothesis accounts for the deformed orbits and the brief occurrence of high frequencies in the swirl velocities.

### 3.2. Simulations

Attention is now turned to the simulated data. There are two issues involved in the utilization and interpretation of this data. First, how consistent is the paradigm in recovering ring kinematics which should be independent of the orbit? This issue is presently being addressed. Addressed here is the issue of establishing how well the GCM agrees with the observations. Specifically, the center path, orbit ellipses, and translation velocity as inferred from the simulated data are compared with the same properties as determined from the observations.

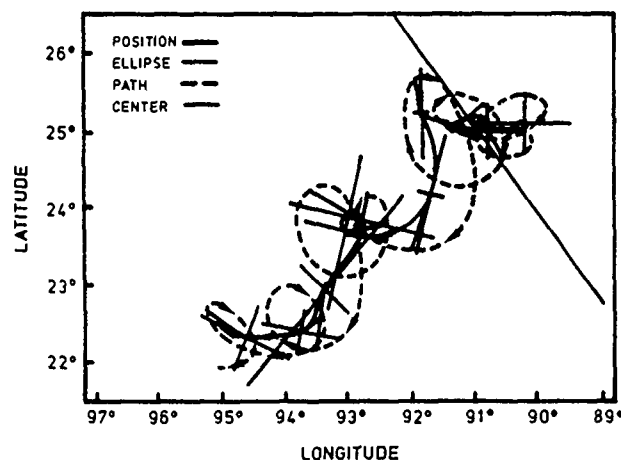


Fig. 7a

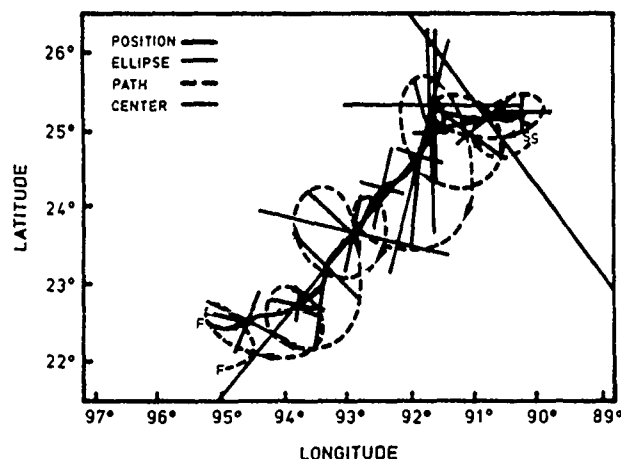


Fig. 7b

Fig. 7 Path and orbit ellipses (blue) of a simulated drifter from the HT GCM. Arrows on the path are at 10-day intervals, while ellipses are shown at 15-day intervals. Figure 7a shows the ellipses using the orbit-inferred center as the flow center, and Figure 7b uses the maximum interface displacement anomaly. Both centers are shown in red.

Figure 7 shows the path of one of several simulated drifters from the HT GCM along with the orbit ellipses. Figure 7a depicts the results using the ring center as inferred from the drifter orbit, while Figure 7b repeats the ellipse calculation using the position of the maximum displacement anomaly of the interface. The choice of the interface displacement as representative of the ring center is arbitrary. Presently, we are comparing the maximum interface displacement, the maximum surface elevation displacement and orbit-determined centers. In general, all are within 30 km of each other.

The most significant difference between the orbit-determined centers and interface displacement anomaly occurs in the interval between  $91^{\circ}\text{W}$  and  $93^{\circ}\text{W}$  where the orbit-inferred ring center shows a significant southern loop. This is not seen in the path of the maximum interface displacement anomaly. At  $93^{\circ}\text{W}$  the orbit-inferred center executes an anticyclonic loop that, again, is not seen in the displacement anomaly path. Elsewhere, the orbit-determined path is consistently 5 to 25 km south of the displacement anomaly path.

A comparison of Figures 2, 4, and 7 shows that the simulated and observed centers follow the same general path through this part of the midgulf. In general, the simulated center path is 10 to 35 km south of the observed path, depending upon which of the two simulated center paths is used. There is virtually no evidence of the interaction with the continental slope topography and circulation in the model results as was seen in the observations. None of the simulated orbits were deformed or appeared to be pulled out temporarily from the ring. Somewhat surprisingly, we have found less consistency in the ellipse calculations for the simulations than in the observations. A number of the ellipses from the simulated data are quite deformed. They also show frequent reversals of the major and minor axes. Overall, however, as the ring nears the slope region, a northeast orientation appears to develop in the orbit ellipses.

Figure 8 shows the translation and swirl velocities for the simulation. Figure 8a gives the results using the orbit center, and Figure 8b uses the maximum displacement anomaly as the ring center. The dominant period in the swirl velocities is about 24 days, or 10 days more than was found in the observations. Note that the swirl velocities, as calculated from either center, are of comparable magnitude, about 30 cm/s.

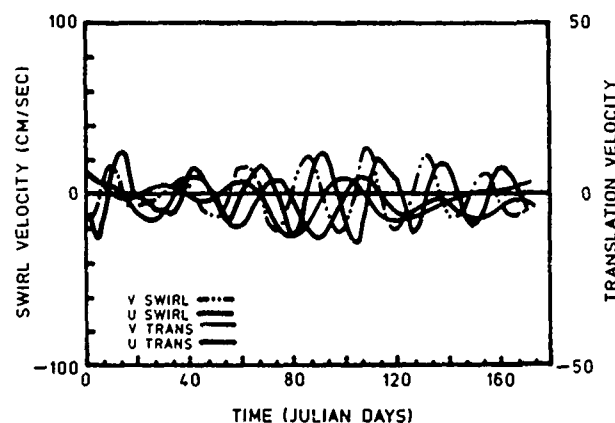


Fig. 8a

Fig. 8 Translation and swirl velocities as inferred from the HT GCM. The east and north components of the translation velocity are depicted in red and blue, respectively. The scale for the translation velocity is on the right. Figure 8a shows results using the orbit-inferred center, while Figure 8b (next page) shows results using the maximum displacement anomaly as the flow center.

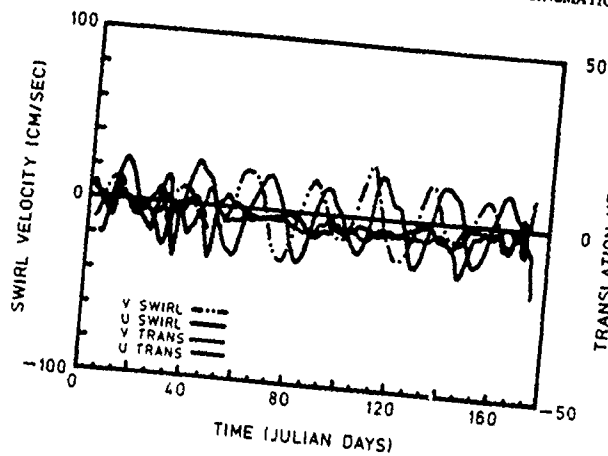


Fig 8b

This is somewhat less than the observed swirls, but this could be rectified by picking a simulated drifter in a greater orbit. There seems to be more difference in the translation velocities. Because its path is straighter, the displacement anomaly path has less variance. The mean westward component in both cases of about 5 cm/s is consistent with the observations.

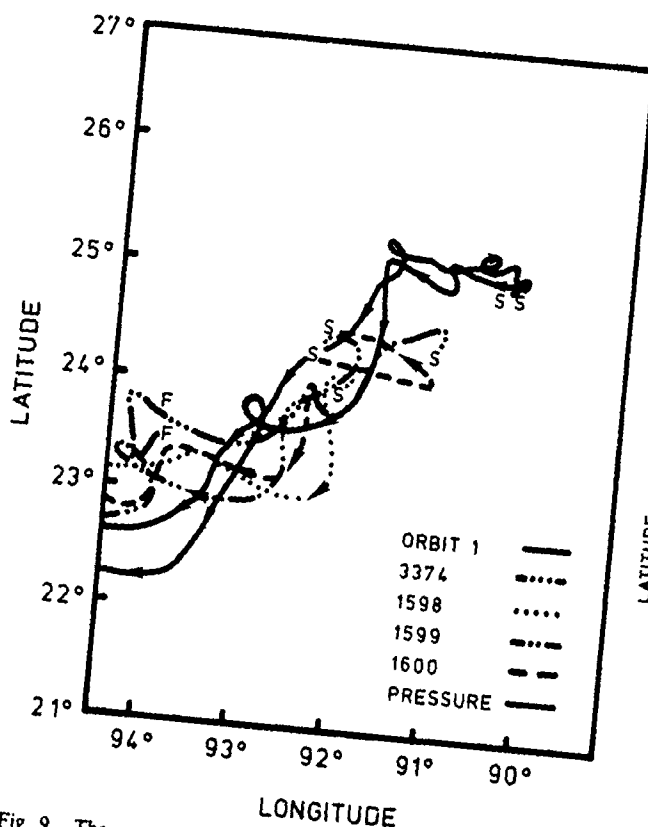


Fig 9 The centers for the 1980–1981 ring, the 1982–1983 ring, and the HT GCM simulation. Orbit 1 (red) refers to the orbit-determined center, and pressure (blue) refers to the maximum displacement anomaly path. Arrows depict 10-day intervals.

Figure 9 compares the inferred center movement for all four drifters along with the inferred center of the simulated drifter and the displacement anomaly path east of 94°W. This is the region where there is no apparent effect of slope topography or circulation in the observations. Of course, details in the paths vary, but overall the agreement is quite good. The maximum deviation at any one time between any of the paths is

100 km, which is only two-thirds the diameter of a typical ring. For most of the paths, the orbit-determined centers are somewhat south of the displacement anomaly path. However, as the paths near 94°W, the observed centers move north of the displacement anomaly. All the orbit-determined center paths show considerably more structure than does that of the displacement anomaly.

#### 4. CONTINENTAL SLOPE

It is remarkable that both observed rings and the simulated ring impacted the continental slope in the same area. This is seen in Figure 10, which shows the drifter paths, inferred center paths, and orbit ellipses for all three cases. In the case

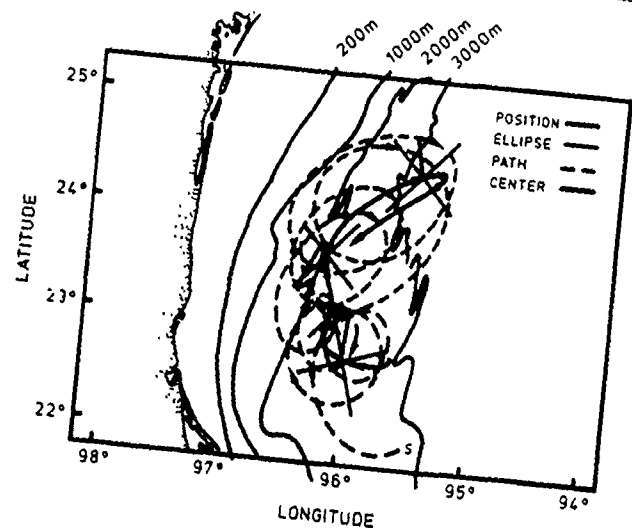


Fig. 10a

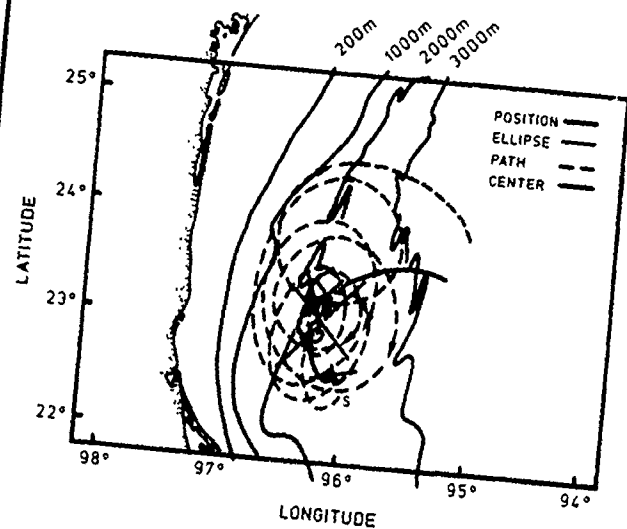


Fig. 10b

Fig 10 Drifter paths, inferred centers and orbit ellipses for (a) the 1981–1982 ring, (b) the 1982–1983 ring (above), (c) the simulated ring, and (d) center paths along the continental slope (next page). Arrows on the paths depict 10-day intervals, while the ellipses are at 15-day intervals.

of the simulated data (Figure 10c), the orbit-inferred center path and the displacement anomaly path are virtually identical. Consequently, it is only necessary to display one set of calculations. The orbit-determined centers were used here.

Figure 10d illustrates how close the movements of the two observed and simulated rings are. There the paths of the inferred centers along with the displacement anomaly path have

been superimposed. Except for the beginning and end of the paths, the maximum deviation is 70 km with a rms deviation of 12 km. Moreover, all paths show the same general characteristics. Both the observations and simulation show a northward migration along the isobaths but with some eastward or looping component.

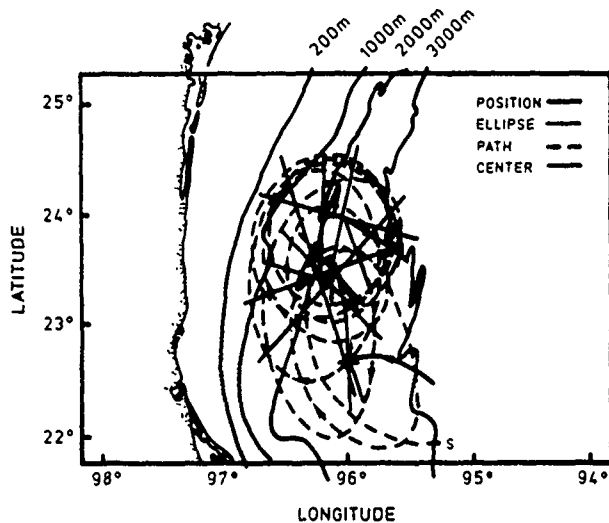


Fig. 10c

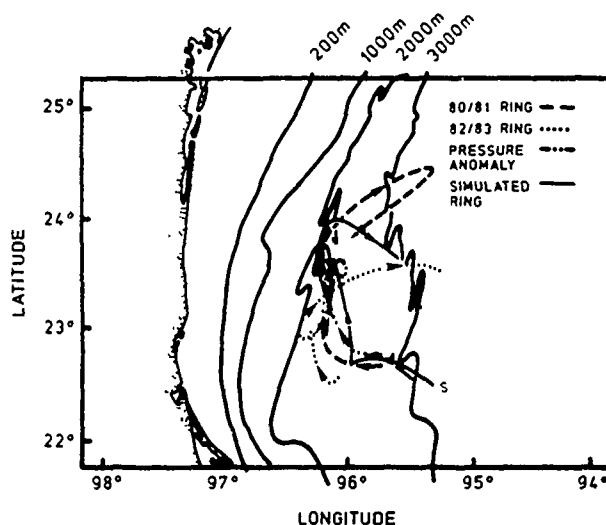


Fig. 10d

Fig. 10. (cont.) Drifter paths, inferred centers and orbit ellipses for (c) the simulated ring, and (d) center paths along the continental slope. Arrows on the paths depict 10-day intervals, while the ellipses are shown at 15-day intervals

The northward migration along the slope is puzzling, as conventional theory [Smith and O'Brien, 1983] would have topographic beta drive the rings to the south. Recently, Smith [1986] has suggested that the northward migration may be due to boundary effects. An alternate explanation was offered by Nakamoto [1986], who found northward propagating soliton solutions in a two-layer, nonlinear, quasi-geostrophic model.

The swirl and translation velocity time series are shown in Figure 11. In the 1980–1981 ring the dominant period is 15 days, almost exactly that found in the midgulf. For the 1982–1983 ring the dominant period is about 11 days, slightly less than that found in the midgulf. The simulated ring also shows

a decrease in the dominant period to about 15 days. The magnitudes of the observed ring's swirl velocities are about 40 to 50 cm/s, which is close to that found in the midgulf. The swirl velocity for the simulated ring is about 80 cm/s, substantially more than what was obtained for the midgulf. All translation velocities indicate a fairly steady northward movement of about 4 cm/s.

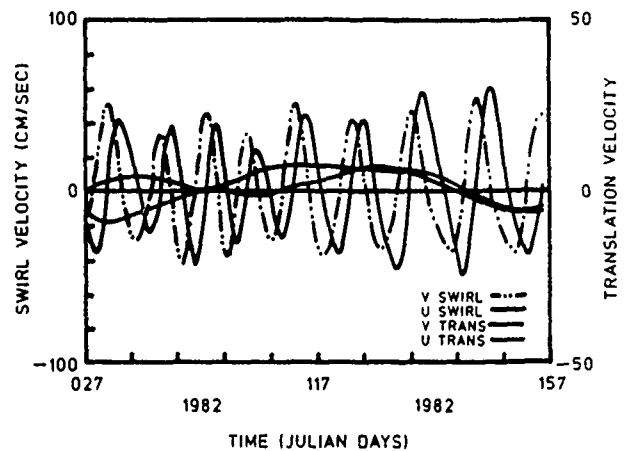


Fig. 11a

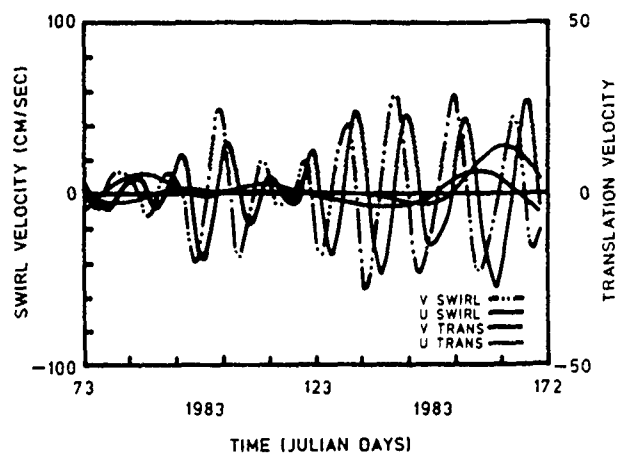


Fig. 11b

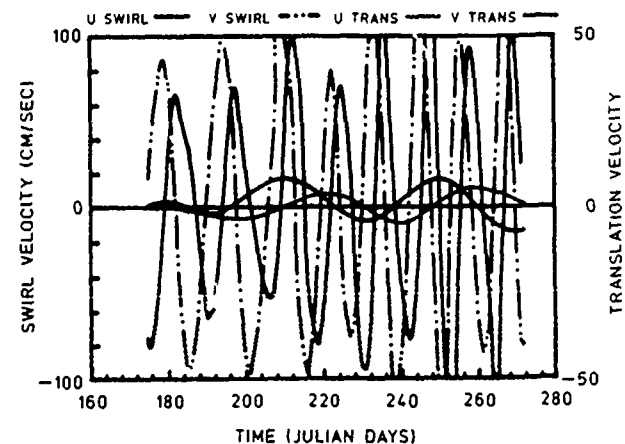


Fig. 11c

Fig. 11 Swirl (left scale) and translation velocities (right scale) for the (a) 1980–1981, (b) 1982–1983, and (c) simulated rings along the continental slope.

## 5. CONCLUSIONS

The paths, translation and swirl velocities, and orbit ellipses have been calculated from Lagrangian observations for two large anticyclonic, Gulf of Mexico rings and one simulated ring. Within the capabilities of the data base and the analysis routine, the following are now established.

1. The paths of the three rings across the central Gulf of Mexico to the continental slope off of Mexico are virtually identical. However, not all Loop Current rings will follow this path. See *Lewis and Kirwan [1987]*.

2. The intraring variability of translation and swirl velocities and the inferred center paths for the 1980–1981 ring are essentially the same as the inter-ring variability between the 1980–1981 and 1982–1983 rings.

3. For the observed rings, there was evidence of strong ellipticity developing as these rings approached the continental slope. The axis of orientation was approximately NE-SW. No independent data on ellipticity were available for the 1982–1983 ring, so it cannot be ruled out that this ring was so orientated. Similar but less pronounced ellipticity was seen in the simulated ring.

4. Both observed rings showed significant distortion of the drifter orbits west of 94°W. This is attributed to interaction of these rings with the continental slope topography and/or slope circulation features. Such interaction was not observed in the simulated ring.

5. After encountering the continental slope off of Mexico, both observed and simulated rings retained their integrity for at least several months while they migrated to the north. The track of the center of both was very close to the 1200-m isobath. The observed swirl speeds were slightly changed from the values obtained from the midgulf. The simulated ring exhibited a substantial increase in swirl velocity. For both the observed and simulated data, the translation speeds were comparable to those obtained for the midgulf.

There are a couple of broader implications of this study pertinent to eddy-resolving GCM's. Both the volume of data as well as the time and space scale resolution of simulated data available from these models far surpasses the typical observational data bases used for verification. Because of the different time and space scales of resolution in the simulated and observed data bases, it is not clear how to establish reliable criteria for statistical comparisons. This study suggests that a potent alternative is to compare model and observed Lagrangian kinematics. Both simulated and observed Lagrangian data sets provide comparable space-time resolution on the evolution of specific circulation features. Moreover, the assessment of the prediction of such features is a more stringent test of a model's predictive capability than are general statistics. The Lagrangian data also provide a means of fine-tuning model parameters such as layer depth, density differences, etc., so that observed and simulated swirl velocities can be matched. As to the HT model, this study has documented the interesting situation that the prediction improves in time, at least as far as the movement of the ring is concerned.

The second and related issue is the use of Lagrangian observations for updating prognostic models. In character, such data are similar to sea surface topographic data derived from satellites [see *Hurlburt, 1986; Thompson, 1986; Kindle, 1986*]. The Lagrangian data contain information on the motion of representative parcels but no information on what is happening nearby. Satellite topographic data return information just

along the satellite path but give no information on the actual motion. Supplementing the latter data with the former data in eddy-resolving general circulation models could significantly upgrade their predictive capabilities.

## APPENDIX

The purpose here is to provide some details on the inversion of (3) and (4) to obtain the time series for the elements of  $Z_k$ . The basis for this inversion is a Taylor expansion in time about the instant  $t_k$  of the velocity vector. From the left-hand side of (3) and (4) one obtains

$$u(t) = u(t_k) + u'(t_k)(t - t_k) + u''(t_k)(t - t_k)^2/2 + u'''(t_k)(t - t_k)^3/6 \quad (A1)$$

$$v(t) = v(t_k) - v'(t_k)(t - t_k) + v''(t_k)(t - t_k)^2/2 + v'''(t_k)(t - t_k)^3/6 \quad (A2)$$

for the interval  $t_k \leq t \leq t_{k+1}$ . The primes represent time derivatives. Now each of the terms on the right-hand side of (A1) and (A2) can be estimated from the velocity record. For example  $u(t_k)$  and  $v(t_k)$  are merely the velocities at time  $t_k$ . The derivatives can be estimated by a variety of techniques; here we have employed centered finite differences.

Now the analytic solution, (5) and (6), can be expanded in a Taylor series as well. When this is done and coefficients of the appropriate powers in this expansion and (A1) and (A2) are equated, a system of simultaneous nonlinear equations is obtained for each time interval. With the subscript  $k$  suppressed, these are

$$X(a + d) + Y(b - c) + 2U_T = 2u \quad (A3)$$

$$X(b + c) + Y(d - a) + 2V_T = 2v \quad (A4)$$

$$X[(d + a)^2 + b^2 - c^2] + 2Yd(b - c) = 4u' \quad (A5)$$

$$2Xd(b + c) + Y[(d - a)^2 + b^2 - c^2] = 4v' \quad (A6)$$

$$X[(d + a)^3 + (b^2 - c^2)(3d + a)] + Y(b - c)(3d^2 + a^2 + b^2 - c^2) = 8u'' \quad (A7)$$

$$X(b + c)(3d^2 + a^2 + b^2 - c^2) + Y[(d - a)^3 + (b^2 - c^2)(3d - a)] = 8v'' \quad (A8)$$

$$X[(a^2 + b^2 - c^2 + d^2)^2 + 4d^2(a^2 + b^2 - c^2) + 4ad(a^2 + b^2 - c^2 + d^2)] + 4Yd(b - c)(a^2 + b^2 - c^2 + d^2) = 16u''' \quad (A9)$$

$$4Xd(b + c)(a^2 + b^2 - c^2 + d^2) + Y[(a^2 + b^2 - c^2 + d^2)^2 + 4d^2(a^2 + b^2 - c^2) - 4ad(a^2 + b^2 - c^2 + d^2)] = 16v''' \quad (A10)$$

These eight equations are inverted at each time step for  $X$ ,  $Y$ ,  $U_T$ ,  $V_T$ ,  $a$ ,  $b$ ,  $c$ , and  $d$ . To our surprise it seems that this can be done analytically. The key to this is the observation that the geometric invariants of the matrix  $M_k$ , i.e.,  $\text{Tr}(M)$  and  $\det(M)$ , can be calculated from observations without knowing  $a$ ,  $b$ , or  $c$ , a priori. After 3 years of inspection it was seen that

$$\det(M) = 2(u''v''' - u'''v'')/(u'v'' - v'u') = M^2 \quad (A11)$$

$$\text{Tr}(M) = (u'v''' - v'u''')/(u'v'' - v'u') = d \quad (A12)$$

Insertion of  $M^2$  and  $d$ , calculated from (A11) and (A12), respectively, into (A5)–(A10) significantly simplifies the latter



expressions. Considerable routine algebra then yields

$$X = 8[u'(M^2 + 2d^2) - 2u''']/M^4 \quad (\text{A13})$$

$$Y = 8[v'(M^2 + 2d^2) - 2v''']/M^4 \quad (\text{A14})$$

$$a = -\{K_1 M^2 + K_2 + K_3(d/2)\}/N \quad (\text{A15})$$

$$b = \{H_1 M^2 + H_2 + H_3(d/2)\}/N \quad (\text{A16})$$

$$c = -\{G_1 M^2 - G_2 + G_3(d/2)\}/N \quad (\text{A17})$$

where

$$N = 8(u'v'' - u''v');$$

$$G_1 = 2(u'^2 + v'^2);$$

$$G_2 = 8(u'^2 + v'^2);$$

$$G_3 = 16(u'u'' + v'v'');$$

$$H_1 = 2(u'^2 - v'^2);$$

$$H_2 = 8(u'^2 - v'^2);$$

$$H_3 = 16(u'u'' - v'v'');$$

$$K_1 = 2u'v';$$

$$K_2 = 8u''v'';$$

$$K_3 = 8(u'v'' + u''v').$$

Incidentally, the parameter  $N$  is directly related to the angular momentum per unit mass of the orbit  $L$ :

$$L = -4N/M^4 \quad (\text{A18})$$

The final step in the calculations is to determine the translation velocities from (A3) and (A4). This is trivial, since all other terms are now known.

**Acknowledgments** We acknowledge support for this research from the Office of Naval Research under contract N-00014-83-K-0256 to the University of South Florida. Support for J.K.L. was supplied by the Minerals Management Service, Gulf of Mexico Physical Oceanography Study, through contract with Science Applications International Corporation. A.D.K. acknowledges the support of the Slover Oceanography Endowment to Old Dominion University. A. Wallcraft very kindly supplied the simulated data from the HT GCM.

#### REFERENCES

- Austin, G. B., Some recent oceanographic surveys of the Gulf of Mexico, *EOS Trans. AGU*, 36(5), 885-892, 1955.
- Blaha, J. P., and W. Sturges, Evidence for wind forced circulation in the Gulf of Mexico, technical report, Dep. of Oceanogr., Fla. State Univ., Tallahassee, 1978.
- Elliot, B. A., Anticyclonic rings and the energetics of the circulation of the Gulf of Mexico, Ph.D. dissertation, Tex. A&M Univ., College Station, 1979.
- Elliot, B. A., Anticyclonic rings in the Gulf of Mexico, *J. Phys. Oceanogr.*, 12, 1293-1309, 1982.
- Flierl, G. R., Particle motions in large amplitude wave fields, *Geophys. Astrophys. Fluid Dyn.*, 18, 39-74, 1981.
- Hooker, S. B., and D. B. Olson, Center of mass estimation in closed vortices: A verification in principle and practice, *J. Atmos. Oceanic Technol.*, 1(3), 247-255, 1984.
- Hurlburt, H. E., Dynamic transfer of simulated altimeter data into subsurface information by a numerical ocean model, *J. Geophys. Res.*, 91(C2), 2372-2400, 1986.
- Hurlburt, H. E., and J. D. Thompson, A numerical study of Loop Current intrusions and eddy shedding, *J. Phys. Oceanogr.*, 10, 1611-1651, 1980.
- Ichye, T., Circulation and water mass distribution in the Gulf of Mexico, *Geophys. Int.*, 2, 47-76, 1962.
- Kindle, J. C., Sampling strategies and model assimilation of altimetric data for ocean modeling and prediction, *J. Geophys. Res.*, 91(C2), 2418-2432, 1986.
- Kirwan, A. D., Jr., A note on a geophysical fluid dynamics variational principle, *Tellus, Ser. A*, 36, 211-215, 1984.
- Kirwan, A. D., Jr., W. J. Merrell, Jr., J. K. Lewis, and R. E. Whitaker, Lagrangian observations of an anticyclonic ring in the Western Gulf of Mexico, *J. Geophys. Res.*, 89, 3417-3424, 1984a.
- Kirwan, A. D., Jr., W. J. Merrell, Jr., J. K. Lewis, R. E. Whitaker, and R. Legeckis, A model for the analysis of drifter data with an application to a warm core ring in the Gulf of Mexico, *J. Geophys. Res.*, 89, 3425-3428, 1984b.
- Lewis, J. K., and A. D. Kirwan, Jr., Some observations of ring-topography and ring-ring interactions in the Gulf of Mexico, *J. Geophys. Res.*, 90(C5), 9017-9028, 1985.
- Lewis, J. K., and A. D. Kirwan, Jr., Genesis of a Gulf of Mexico ring as determined from kinematic analyses, *J. Geophys. Res.*, 92(C11), 11,727-11,740, 1987.
- Nakamoto, S., Application of solitary wave theory to mesoscale eddies in the Gulf of Mexico, Ph.D. dissertation, 50 pp., Dep. of Oceanogr., Tex. A&M Univ., College Station, 1986.
- Nowlin, W. D., *Winter Circulation Patterns and Property Distributions*, Tex. A&M Univ. Oceanogr. Stud., vol. 2, edited by L. R. A. Capurro and J. L. Reid, pp. 3-53, Gulf, Houston, Tex., 1972.
- Nowlin, W. D., and H. J. McClellan, A characterization of the Gulf of Mexico waters in winter, *J. Mar. Res.*, 25, 29-59, 1967.
- Okubo, A., Horizontal dispersion of floatable particles in the vicinity of velocity singularities such as convergences, *Deep Sea Res.*, 17, 445-454, 1970.
- Smith, D. C., IV, A numerical study of Loop Current eddy interaction with bottom topography in the western Gulf of Mexico, *J. Phys. Oceanogr.*, 16(7), 1260-1272, 1986.
- Smith, D. C., IV, and J. J. O'Brien, The interaction of a two layer isolated mesoscale eddy with topography, *J. Phys. Oceanogr.*, 13, 1681-1697, 1983.
- Smith, D. C., IV, and R. O. Reid, A numerical study of non-friction decay of mesoscale eddies, *J. Phys. Oceanogr.*, 12(3), 244-255, 1982.
- Sturges, W., and J. P. Blaha, A western boundary current in the Gulf of Mexico, *Science*, 192, 367-369, 1976.
- Sweitzer, N. B., Jr., Origin of the Gulf Stream and circulation of waters in the Gulf of Mexico with special reference to the effect on jetty construction, *Trans. Am. Soc. Civ. Eng.*, 40, 86-98, 1898.
- Thompson, J. D., Altimeter data and geoid error in mesoscale ocean prediction: Some results from a primitive equation model, *J. Geophys. Res.*, 91(C2), 2401-2417, 1986.
- A. W. Indest and A. D. Kirwan, Department of Oceanography, Old Dominion University, Norfolk, VA 23508.
- J. K. Lewis, Science Applications International Corporation, 1304 Deacon, College Station, TX 77480.
- I. Quintero and P. Reinersman, Department of Marine Science, University of South Florida, 140 Seventh Avenue South, Saint Petersburg, FL 33701.

(Received March 20, 1987;  
accepted May 18, 1987.)

## DYNAMICS OF WARM-CORE MESOSCALE EDDIES\*

LIU Juping (刘举平)

(Institute of Oceanology, Academia Sinica, Qingdao)

A. D. Kirwan, Jr.

(Department of Oceanography, Old Dominion University, Norfolk, VA 23508, U. S. A.)

Received March 20, 1989

## Abstract

A nonlinear model of a warm-core ring is presented here. The model treats the warm-core ring as a confined lens of fluid rotating on an  $f$  plane. A simple polynomial expansion of the hydrodynamic field variables about the center of mass of the lens provides the basis for an exact reduction of the hydrodynamic equations. Observations from two warm-core rings are compared with simulations from the nonlinear model. Fair agreement is found between model calculations and observations from the Gulf Stream and the Kuroshio.

## I. INTRODUCTION

There has been vigorous development in both theory and observation of warm-core rings in recent years. An indication of this activity is the warm-core rings workshop held at the University of Rhode Island, USA in August of 1984. The papers resulting from the workshop included models and observations of rings north of the Gulf Stream (see *J. Geophys. Res.*, Vol. 90, No. 5, 1985).

Warm-core rings are clockwise rotating, high-pressure centers bounded underneath by a strong thermocline that rises around the warm-water pool and reaches the surface, forming a front around the ring's periphery. Typical characteristics of a young warm eddy are an ellipsoidal shape, a horizontal scale of about 200 to 300 km, a center depth of more than 500 m, and surface velocities sometimes in excess of 1 m/s (Kirwan et al., 1988). The popular explanation for the formation of the warm eddy of western boundary currents is separation of the meanders of the currents (Saunders, 1971; Gotthart and Porocshy, 1974). The life of the warm eddies is measured in months. Their usual fate is to reattach to the main currents.

Fig. 1 from Joyce, 1984, shows a warm ring observed north of the Gulf Stream. From the star-shaped observations of the surface currents the diameter of the ring is about 300 km. The 10 °C water reaches the depth of more than 700 m near the ring center. At the depth of 500 m water warmer than 10 °C covers an elliptical area with horizontal scale of 200 km. The high velocity zone is located at the distance of about 100 km from the ring center with maximum current speed of 2 m/s. Fig. 2 from Kawai, 1972, shows a warm ring north of the Kuroshio. The anticyclonic surface currents cover an elliptical area with horizontal dimension of about 300 km. The water warmer than 16 °C drops at the depth of 200 m and occupies an area with horizontal scale of 150 km. The surface current velocity measured by a geoelectromagnetic kinetograph also reached about 2 m/s.

Because of the large swirl velocities and resultant large Rossby numbers it is uncertain whether or not linear quasi-geostrophic dynamics apply. Recently, several non-linear models for warm eddies have been proposed. Cushman-Roisin et al.

\* Contribution No. 1747 from the Institute of Oceanology, Academia Sinica

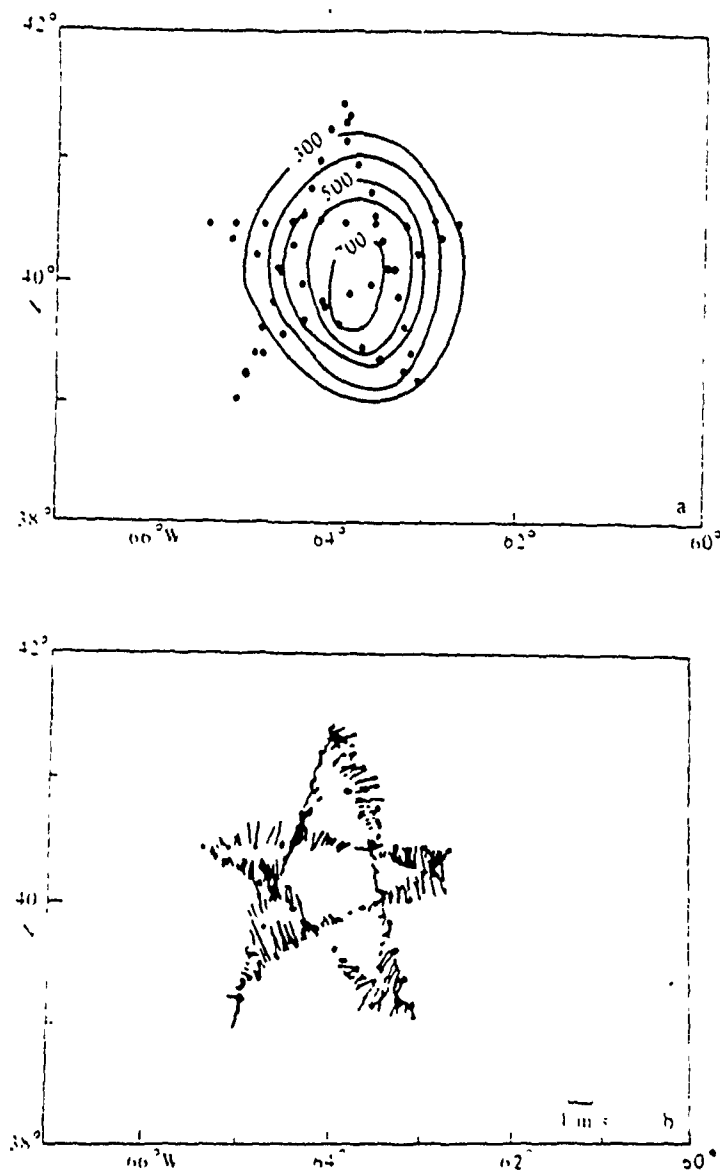


Fig. 1. Star-shaped survey of the ring track carried out from 14 to 16 September 1981 from the R.V. Endeavor. (a) Depth (m) of the 10 °C isotherm from XBTs (dots); (b) Acoustic-Doppler velocity at 28 m depth (from Joyce, 1984)

(1985, 1987) developed a time-dependent, non-linear model for the warm-core rings and obtained analytical solutions to special linear and non-linear cases. Kirwan and Liu (1989) presented a systematic numerical investigation of the general system of the equations developed by Cushman-Roisin et al. (1985) as an initial value problem. In the Kirwan/Liu formulation the time dependent amplitude equations for the vorticity, divergence, deformation, and the ellipse shape were developed and solved numerically. This decomposition provides a simple description of the geometry and kinematics of warm eddies.

The present paper applies the model of Kirwan and Liu (1989) to warm eddies

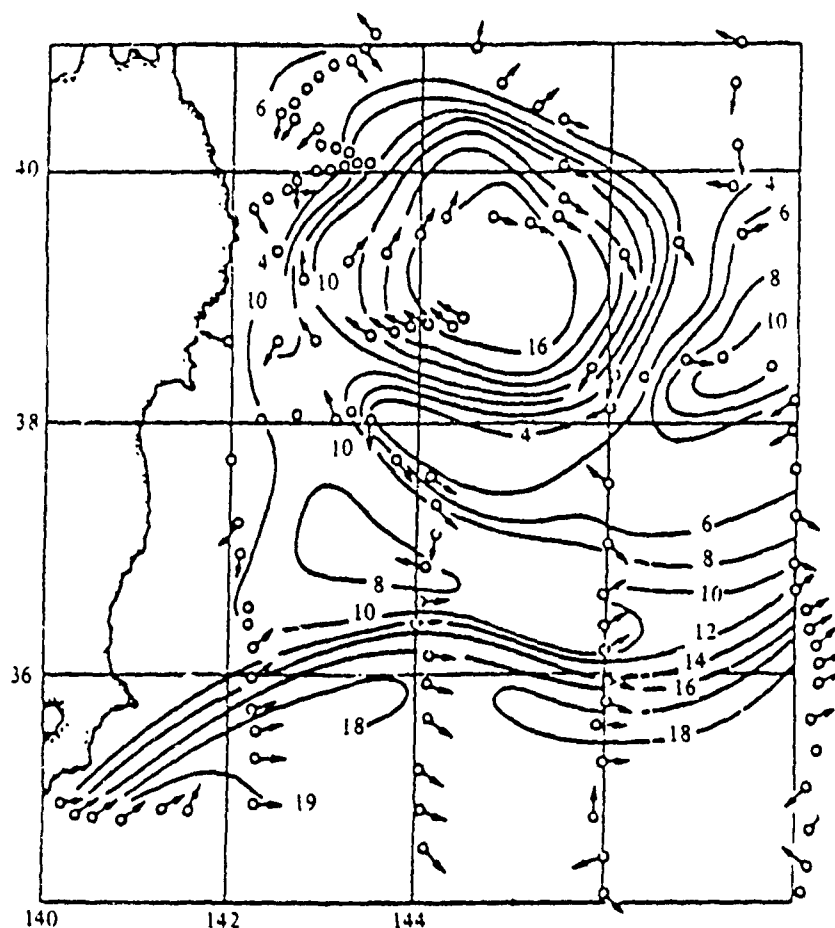


Fig. 2. Temperature distribution ( $^{\circ}\text{C}$ ) at a depth of 200 m in a region east of Japan on August 12–21, 1960.

The circles show the positions of the hydrographic stations. The arrows indicate the direction of surface currents measured by a geoelectromagnetic kinetograph (after Kawai, 1972)

spawned by western boundary currents. A brief review of the model is given in the next section. A comparison of model calculations with the observations is presented in sections 3 and 4. The last section gives a brief discussion of the results.

## II. MODEL REVIEW

The following is a brief review of the model given by Kirwan and Liu (1989). We start with the well known reduced-gravity equations for an inviscid two layer fluid.

$$u_t + uu_x + vu_y - fv = -gh_x \quad (1.a)$$

$$v_t + uv_x + vv_y + fu = -gh_y \quad (1.b)$$

$$h_t + (hu)_x + (hv)_y = 0 \quad (1.c)$$

where  $f$  is the Coriolis parameter,  $g$  reduced gravity, and  $h$  the upper layer thickness. The lower layer is assumed to be infinitely deep and at rest.

If the boundary of the upper layer is an ellipsoid, an exact solution to (1) is

$$u = (G/2 + G_n)x + (G_t - G_r)y \quad (2.a)$$

$$v = (G_r + G_t)x + (G/2 - G_n)y \quad (2.b)$$

$$h = h_0 + (B/2 + B_n)x^2 + 2B_txy + (B/2 - B_n)y^2 \quad (2.c)$$

where  $h_0$ ,  $B$ ,  $B_t$ ,  $B_n$ ,  $G$ ,  $G_r$ ,  $G_n$ , and  $G_t$  are functions of time only, and  $x$  and  $y$  are coordinates relative to the center of mass. The eight amplitudes in (2) can be determined by substituting (2) into (1). This results in the following system of differential equations:

$$\dot{h}_0 + Gh_0 = 0 \quad (3.a)$$

$$\dot{B} + 2\{BG + 2(B_nG_n + B_tG_t)\} = 0 \quad (3.b)$$

$$\dot{B}_t + 2B_tG + BG_t - 2B_nG_r = 0 \quad (3.c)$$

$$\dot{B}_n + 2B_nG + BG_n + 2B_tG_r = 0 \quad (3.d)$$

$$\dot{G} + G^2/2 + 2(G_n^2 + G_t^2 + G_r^2) - 2fG_r + 2gB = 0 \quad (3.e)$$

$$\dot{G}_r + GG_r + fG/2 = 0 \quad (3.f)$$

$$\dot{G}_n + GG_n - fG_t + 2gB_n = 0 \quad (3.g)$$

$$\dot{G}_t + GG_t + fG_n + 2gB_t = 0 \quad (3.h)$$

where  $(\dot{\phantom{x}}) = \frac{d}{dt}(\phantom{x})$ . The first four parameters  $h_0$ ,  $B$ ,  $B_t$ , and  $B_n$  describe the distribution of mass within the ring. The remaining four parameters  $G$ ,  $G_r$ ,  $G_n$ , and  $G_t$  are recognized as the divergence, vorticity, shear and normal deformation rate of the ring. See Kirwan, 1975, for a discussion of the physical interpretation of these quantities. The equations in (3) describe the evolution of warm-core rings under appropriate initial conditions. The center mass of the ring undergoes steady inertial motion (Ball, 1963), therefore, the system of the equations (3) governs the motion of the ring in a coordinate system moving with the center of the ring mass.

There are two special analytical solutions of the model. One is an elliptical shaped ring which was named *rodon* by Cushman-Roisin et al. (1985). The other is a circular ring first discovered by Cushman-Roisin (1987) and named *pulson* by Kirwan and Liu (1989).

We consider first the rodon solution. Assuming  $G=0$  and  $B$  is constant, the  $h_0$  and  $G_r$  become constant and the equations (3.c), (3.d), (3.g) and (3.h) reduce to four linear differential equations. The analytical solution of the rodon from the four linear equations is

$$B_t = -B_D \cos \theta \quad (4.a)$$

$$B_n = -B_D \sin \theta \quad (4.b)$$

$$G_n = G_D \cos \theta \quad (4.c)$$

$$G_t = -G_D \sin \theta \quad (4.d)$$

where  $\theta = \omega t + \varphi$ . The phase  $\varphi$  can be chosen according to the initial orientation of the ellipse. The  $B_D$ ,  $G_D$ ,  $B$ ,  $G_r$ , and  $\omega$  are constrained by equations

$$B_D(\omega + 2G_r) - BG_D = 0 \quad (4.e)$$

$$G_D(f - \omega) - 2gB_D = 0 \quad (4.f)$$

$$G_D^2 - G_r^2 - fG_r + gB = 0 \quad (4.g)$$

There are different ways to specify these parameters. Here we chose  $B$  and  $B_D$ , according to the initial condition, to express the others. From the four linear equations and (4.e), (4.f), and (4.g), the constraints can be obtained as

$$G_D = (2B_D / \delta) M^{+-} \quad (4.h)$$

$$G_r = -f/2 + (B / \delta) M^{+-} + M^{+-} / 4 \quad (4.i)$$

$$\omega = f - M^{+-} / 2 \quad (4.j)$$

where

$$M^{+-} = (f^2 + \delta g)^{1/2} \pm (f^2 - \delta g)^{1/2} \quad (4.k)$$

and

$$\delta = 4[B^2 - 4B_D^2]^{1/2} \quad (4.l)$$

Kirwan and Liu (1989) showed that (4) can be obtained from the general system of equations (3) if special initial values are specified.

On the other hand, by assuming  $B_r = B_n = G_n = G_r = 0$ , the equations (3.a), (3.b), (3.e), and (3.f) reduce to four non-linear equations. A particular analytical solution of these equations is the pulson solution. This is

$$h_0 = H / [1 + \gamma \sin(f't + \varphi)] \quad (5.a)$$

$$B = -(\Lambda_B / 4g) / [1 + \gamma \sin(f't + \varphi)]^2 \quad (5.b)$$

$$G = f\gamma \cos(f't + \varphi) / [1 + \gamma \sin(f't + \varphi)] \quad (5.c)$$

$$G_r = -(f/2) \{1 + \Lambda_Q / [1 + \gamma \sin(f't + \varphi)]\} \quad (5.d)$$

There are also constraints for the solution from the  $\dot{G}$  equation

$$\Lambda_B = f^2(1 - \gamma^2 - \Lambda_Q) > 0 \quad (5.e)$$

$$-1 < \gamma < 1 \quad (5.f)$$

Subject to special constraints the numerical solution of the general system of equations (3) is identical to (5).

### III. ELLIPTICAL EDDIES

A great number of observations show that the warm eddies are elliptical. The major axis of the ellipse is meridional in Fig. 1, but zonal in Fig. 2. Supposing the elliptical eddies only rotate and do not change their size then the rodon special case applies.

In the general system of equations (3), choosing  $f = 10^{-4} s^{-1}$ ,  $\Delta\rho/\rho = 1.5 \times 10^{-3}$ , we obtained one example of the rodon with the following initial values:

$$B_r(0) = G(0) = G_n(0) = 0$$

$$h_0(0) = 0.5 \text{ km}$$

$$B(0) = -8.5 \times 10^{-5} \text{ km}^{-1}$$

$$B_n(0) = -2.0 \times 10^{-5} \text{ km}^{-1}$$

$$G_r(0) = -1.220488 \text{ day}^{-1}$$

$$G_s(0) = -0.52157 \text{ day}^{-1}.$$

The initial ellipse is located with a meridional major axis of 298 km and a zonal minor axis of 178 km. The ellipse rotates clockwise and completes 1 rotation in 56 days. The particles also move clockwise around the center of the ring at maximum speed of 1.8 m/s. Fig. 3 shows the boundary of the ring at its 2nd and 13th day respectively. The end to head arrow lengths indicate the distances the particles within the ring move in two hours on that day. The length of the arrows has the same scale as the coordinates.

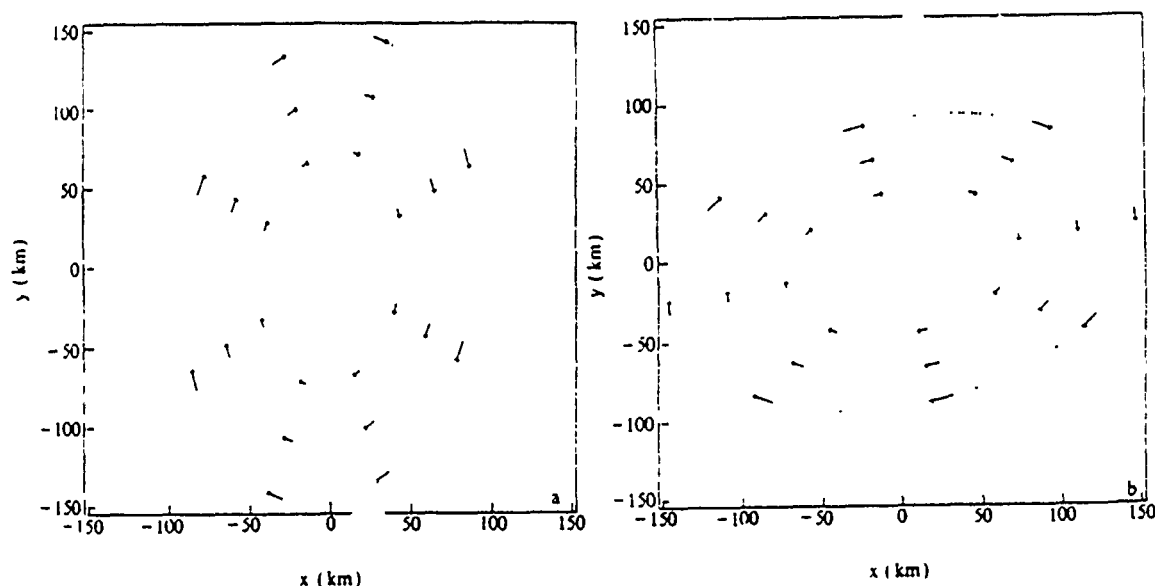


Fig. 3. The moving state of the various particles within the ring eddy during the first two hours on its 2nd day (a) and 13th day (b). The dashed ellipse is the position of the boundary at the same time.

Kirwan and Liu (1989) showed that the roton solutions apply if  $0 < \delta < (f^2/g)$ . Setting the major axis in the meridional direction, the initial values for the general roton case are

$$h_0(0) = H \quad (6.a)$$

$$B_r(0) = G(0) = G_n(0) = 0 \quad (6.b)$$

$$B(0) = -[(\delta/4)^2 + 4B_D^2]^{1/2} \quad (6.c)$$

$$B_n(0) = -B_D \quad (6.d)$$

$$G_r(0) = -f/2 + (B(0)/\delta) M^{+-} + M^{-+}/4 \quad (6.e)$$

$$G_s(0) = -(2B_D/\delta) M^{+-} \quad (6.f)$$

where  $B_D > 0$ . The size of the ring and the velocity field depends upon  $H$ ,  $\delta$  and  $B_D$ .

Large  $H$  provides large horizontal scale of the rings, while large  $B_0$  causes the particles to move faster. The rotation of the ellipse and particles is determined by  $\delta$ . There are two groups of possible values in (6) which depend upon the selection of + and - in  $M$ . A choice of  $M^+$  gives a slower spin and an ellipse rotation rate proportional to  $\delta$ ; the  $M^-$  selection results in faster spin and a rotation rate inversely proportional to  $\delta$ . In the example the solution is for the  $M^+$  root. Fig. 4 shows the relationship between  $\omega$  and  $\delta$ . This plot shows that for a given value of  $\delta$  there are two possible ellipse rotation rates. The  $M^-$  root refers to the lower branch of  $\omega$ .

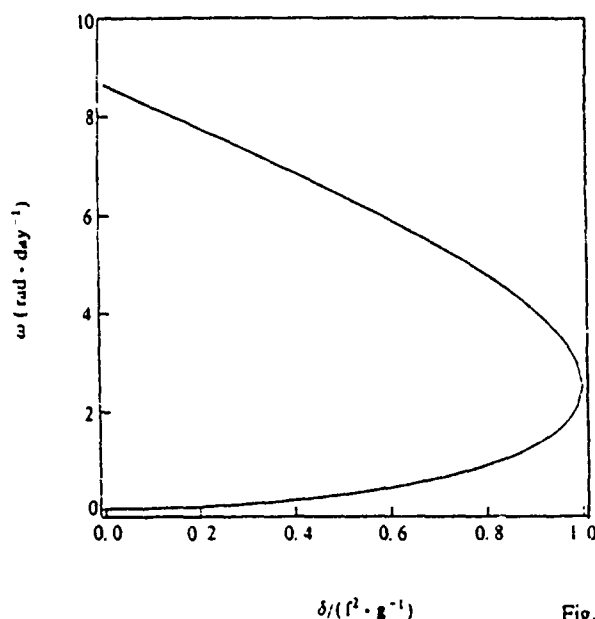


Fig. 4. Relationship between rotating rate of the ellipse  $\omega$  and  $\delta$

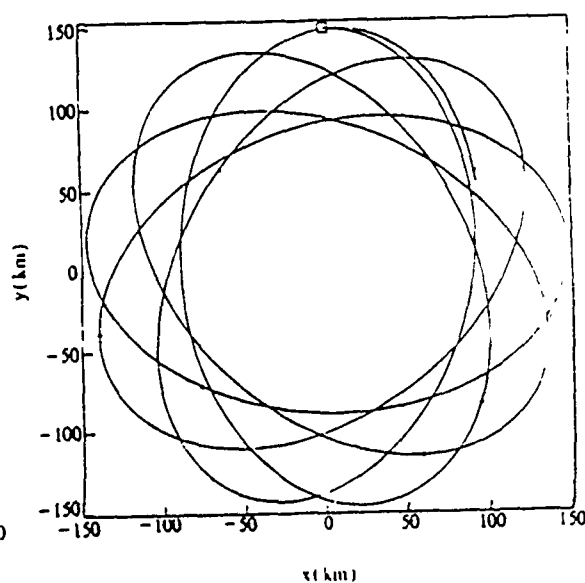


Fig. 5. The path of the particle at the boundary (the square) of the rodon during its first 30 days. The arrows indicate the moving direction

Subject to the general initial condition (6), the numerical solutions show that the dynamic fields,  $h_0(t)$ ,  $B(t)$ ,  $G(t)$ , and  $G_r(\cdot)$  retain their initial values, which means that the center depth, the divergence, and the vorticity of the rodon are constant during the evolution of the eddies. The particles within the eddies rotate at the frequency of  $[\omega/2(f - \omega/2)]^{1/2}$  around the center (Ripa, 1987). In the example  $\omega$  is 0.036 cycle per day, therefore, the particles rotate at the rate of 0.156 cycle per day, which is much larger than that of the frame of the eddy. Fig. 5 shows the path of a particle at the boundary of the eddy. The square in this figure indicates the initial position of the particle. The particle completes 4.7 cycles along the boundary of the eddy in a month. The structure of the particle velocity field is not isotropic. Particles near the minor axis move faster than those near the major axis. This is the result of conservation of total angular momentum for the eddy (Ball, 1963 and Kirwan and Liu, 1989). The maximum velocities, therefore, are located at the cross points of the minor axis and the boundary of the ring (Fig. 3).

#### IV. CIRCULAR EDDIES

Observations also show that the shape and the size of the warm eddies change



with time. The shape of eddies in the ocean surface sometimes is circular. The circular eddies can be approximated with the pulson special case of the general system of equations (3).

Choosing phase  $\varphi = 0$  could not lose the generality. The initial conditions of the pulson case can be specified as

$$h_0(0) = H \quad (7.a)$$

$$B_r(0) = B_n(0) = G_n(0) = G_r(0) = 0 \quad (7.b)$$

$$B(0) = -\Lambda_B / (4g) \quad (7.c)$$

$$G(0) = f\gamma \quad (7.d)$$

$$G_r(0) = - (f/2)(1 + \Lambda_Q) \quad (7.e)$$

where  $H$  is the average depth of the ring center. The  $H$ ,  $\gamma$ , and  $\Lambda_Q$  can be chosen from the initial condition.

Kirwan and Liu (1989) showed that the pulson size and the associated velocity field depend upon  $H$ ,  $G(0)$ , and  $G_r(0)$ . Large ring and high velocity are produced by large  $H$ ,  $G(0)$ , and  $G_r(0)$ . i.e. the evolution of the ring the  $B_r(t)$ ,  $B_n(t)$ ,  $G_r(t)$ , and  $G_r(t)$  retain their initial values of zero, which means that the eddies in the pulson mode always keep their circular shape and have no shear and normal deformation. The motion of the pulson eddies is a periodic but nonlinear expansion and contraction of their circular outcrop at the inertial frequency. The particle motions within the lens are anticyclonic. The average circle in the sea surface is coupled with the mean depth  $H$ . The maximum (minimum) circles are related to minimum (maximum) depth of the ring center. If the initial value  $G_r(0) < -f/2$  (positive  $\Lambda_Q$ ), the local spin  $G_r(t)$  is always negative and the particles move clockwise around the ring center. However, if the  $G_r(0) > -f/2$  (negative  $\Lambda_Q$ ), the local spin can change its sign as the ring goes to its minimum radius. In this case the local spin may briefly achieve positive (cyclonic) values.

For simulating eddies spawned by western boundary currents, initial values are chosen subject to (7) as

$$h_0(0) = 0.3 \text{ km}$$

$$B_r(0) = B_n(0) = G_n(0) = G_r(0) = 0$$

$$B(0) = -4.71939 \times 10^{-5} \text{ km}^{-1}$$

$$G(0) = 3.456 \text{ day}^{-1}$$

$$G_r(0) = -1.08 \text{ day}^{-1}$$

Fig. 6(a) and (b) show the position of the surface circle of the eddy at its 0.15 and 0.5 days of evolution where the dashed circles indicate the initial position of the boundary. The diameter of the eddy can change from 265 km to 143 km. The period of the oscillation of the boundary is 0.73 day, which corresponds to an inertial oscillation with  $f = 10^{-4} \text{ s}^{-1}$ . Fig. 6(c) and (d) show the vertical sections in (a) and (b). The shallow mode has a larger surface area while the deep mode has a smaller area. The depth of the eddy can change from 210 m to 500 m. The frequency

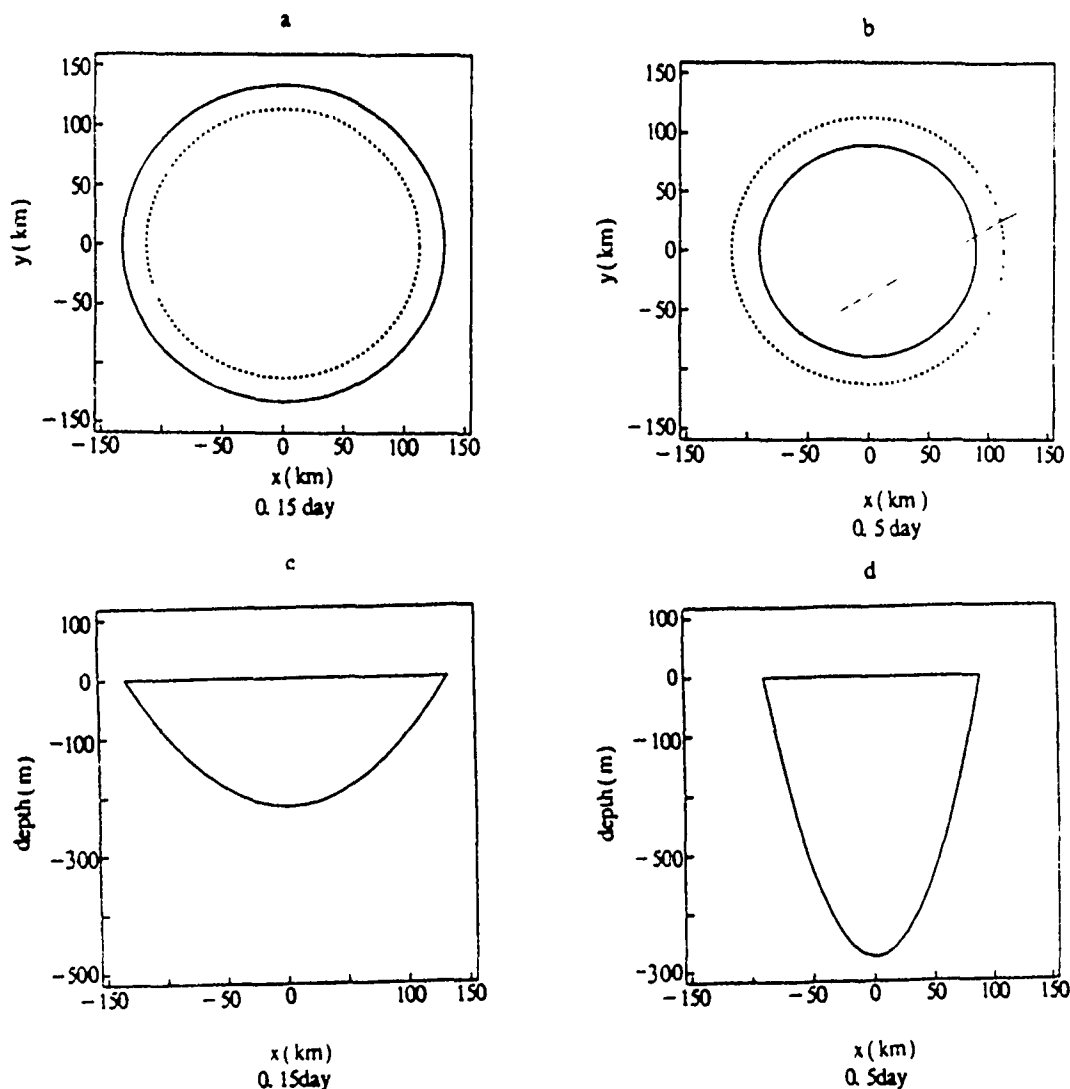


Fig. 6. (a, b) The positions of the surface circles at 0.15 and 0.5 days. The dashed circles are the initial boundaries; (c, d) the relative vertical sections of the pulson.

of the depth variation is the same as that of the surface circle, i. e. the Coriolis frequency. The amplitude of the fluctuation at the surface and the depth depends upon the horizontal divergence in the eddy. A large  $G(0)$  produces a large variation of the  $G(t)$  and, therefore, produces a large amplitude of the variation in the surface circle and the depth of the ring. The velocities of the particles increase gradually from the center to the boundary of the ring, with a maximum value of 2 m/s. The larger the  $G(0)$ ,  $G_t(0)$ , and  $H$ , the higher the velocity of the ring. The velocity field of the pulson, unlike the rodon, is isotropic at all times. The variation of the velocities in this case is remarkable as the particles move from the largest circle to the smallest. Fig. 7 shows the different modes of the velocity field where the solid circles are the initial positions of the boundaries and the dashed circles indicate the evolved boundaries of the ring. The scale of the arrows is the same as that of the coordinates. We can see from Fig. 7 that the ring expands first from the initial position to its maximum then shrinks to the

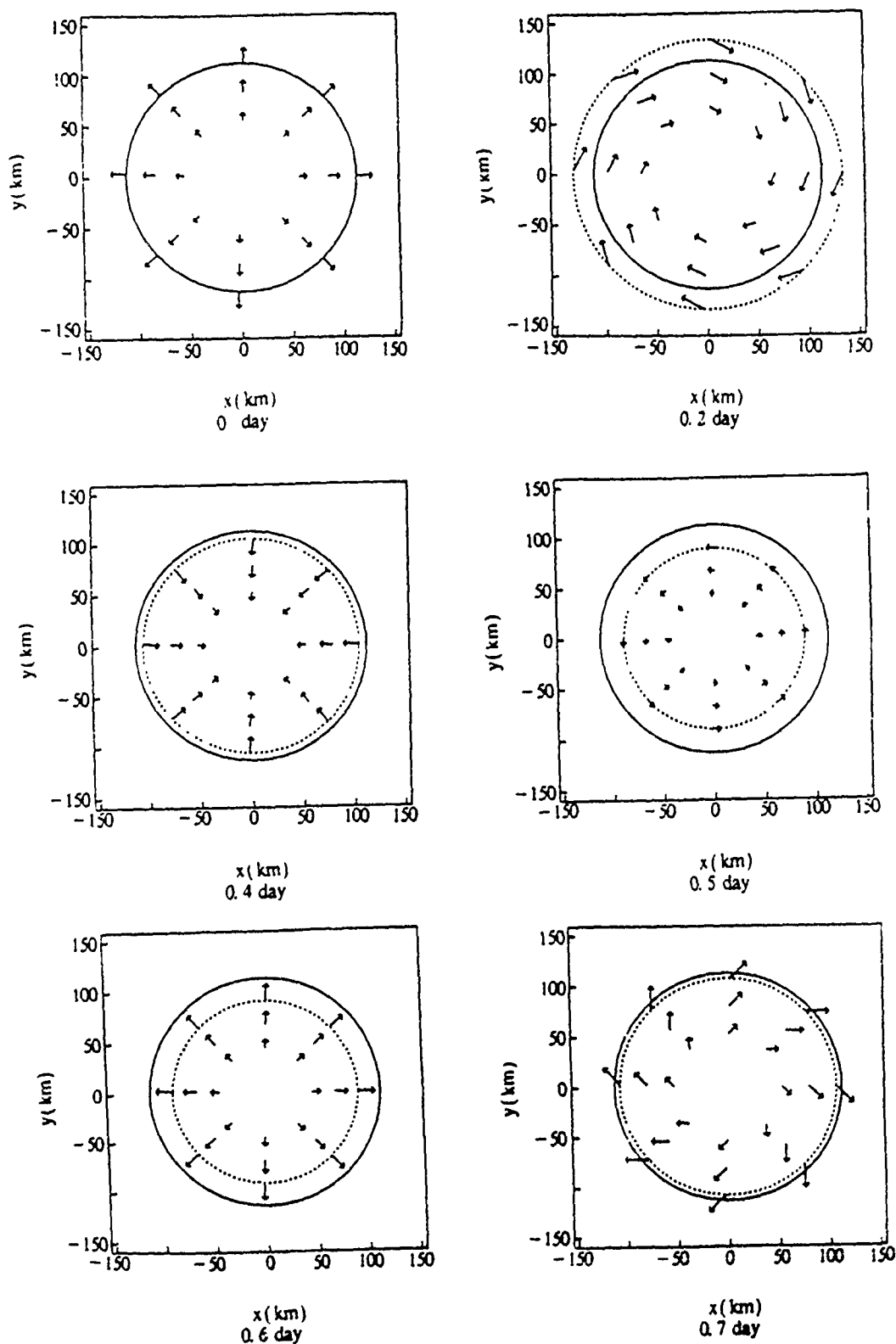


Fig. 7. The moving states of the various particles within the pulson during 0.1 day at different ages of the ring. The dashed circles are the boundaries at the same age and the solid circles are the initial positions of the boundaries.

minimum. Although the particles move back and forth with the motion of the circles, they tend to spend more time in the shallow, large radius mode than in the deep, small radius mode. This is attributed to the basic nonlinearity of the model. One notes that the particles move slower as the ring is in the deep, small radius mode. This is the result of the principle of angular momentum conservation. Because of the sign change of the local spin at the deep, small radius mode, particle paths show some brief cyclonic structures (Fig. 7d). Fig. 8 shows the path of the particle (the square) at the boundary of the ring. In this example it takes 7.5 days for a particle to complete one cycle around the center of the eddy.

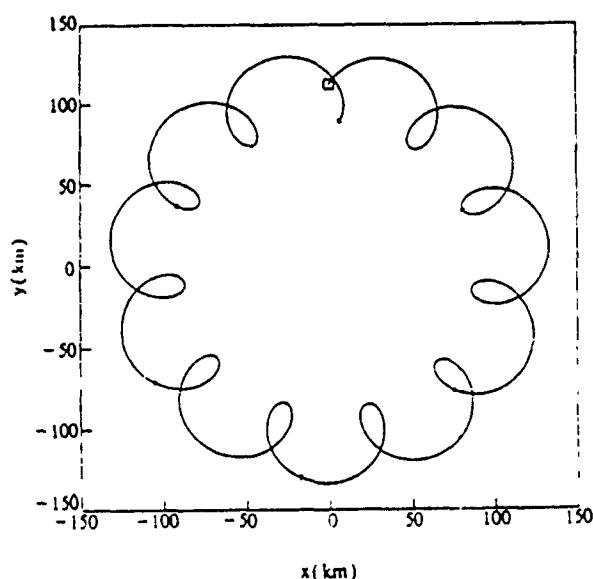


Fig. 8. The path of the particle at the boundary (the square) of the pulson during its first 7.8 days. The arrows indicate the moving direction.

## V. DISCUSSION

Both examples of the numerical results are in fair agreement with the warm eddies in Fig. 1 and Fig. 2 in the horizontal scale and the velocity fields. It is worth noting that the rotation of the ellipse as a whole ring is different from the rotation of the particles in the model. In the example of the rodon, the ellipse rotates once in 56 days while the particles complete one revolution around the ring center in only 6.4 days. In the example of the pulson, the particles move once around the ring center in 7.5 days. It is hard to measure the rotating rate of the ellipse from the hydrographic data. Therefore, the rotating rate of about one cycle per 3.6 days in the Gulf Stream eddy (Fig. 1) observed by Joyce (1984) probably corresponds to the rotating rate of the particles in the examples, not of the ellipse.

For simulation of large warm eddies of western boundary currents, the initial values must be chosen to correspond with the lower value of  $\omega$  in the model. This implies  $M^*$  option for the rodon case. In the pulson case, the rate of vorticity should be chosen in the range of  $-f/2 < G_r(0) < 0$ .

The numerical scheme used in the calculations is a standard explicit linear

multistep method. The time step in the integration is 0.01 day. The numerical tests showed that all of the modes both in the rodon and the pulson are stable if  $B(0) < 0$  and  $B(0)^2 - 4B_0^2 > 0$  in the initial values.

### ACKNOWLEDGMENT

This research was sponsored by the Office of Naval Research through the grant N00014-89-J-1595, and the National Science Foundation through a grant subcontracted from the University of Miami to Old Dominion University. A. D. Kirwan gratefully acknowledges the support of the Samuel L. and Fay M. Slover Endowment to Old Dominion University.

### References

- Bail, F. K., 1963. Some general theorems concerning the finite motion of a shallow rotating liquid lying on a paraboloid. *J. Fluid Mech.* 17: 204-256.
- Cushman-Roisin, B., W. H. Heil, and D. Nof, 1985. Oscillations and rotations of elliptical warm-core ring. *J. Geophys. Res.* 90: 11756-11764.
- Cushman-Roisin, B., 1987. Exact analytical solutions for elliptical vortices of the shallow-water equations. *Tellus*, 39A: 235-244.
- Guthardt, G. A., and G. J. Potocsky, 1974. Life of a Gulf Stream anticyclonic eddy observed from several oceanographic platforms. *J. Phys. Oceanogr.* 4: 131-134.
- Joyce, T. M., 1984. Velocity and hydrographic structure of a Gulf Stream warm-core ring. *J. Phys. Oceanogr.* 14: 936-947.
- Kawai, H., 1972. Physical Aspects of the Japan Current. In Kuroshio, Univ. of Washington Press, Seattle, pp. 235-352.
- Kirwan, A. D., Jr., 1975. Oceanic velocity gradients. *J. Phys. Oceanogr.* 5: 729-735.
- Kirwan, A. D., Jr., J. K. Lewis, A. W. Indest, P. Reinertman, and I. Quintero, 1988. Observed and simulated kinematic properties of loop current ring. *J. Geophys. Res.* 93: 1189-1198.
- Kirwan, A. D., Jr. and Juping Liu, 1989. The shallow water equations on an F plane. To appear in Nonlinear Topics in Ocean Physics, Course CIX, Int'l. School of Physics "Enrico Fermi", A. R. Osborne ed., North Holland.
- Ripa, P., 1987. On the stability of elliptical vortex solutions of the shallow-water equations. *J. Fluid Mech.* 183: 343-363.
- Saunders, P. M., 1971. Anticyclonic eddies formed from Shoreward meanders of the Gulf Stream. *Deep Sea Res.* 19B: 1207-1219.